The Arab American University

Faculty of Graduate Studies

Formation and characterization of the In_2Se_3/CuO heterojunctions

By

Reham Reda Kmail

Supervisor

Prof. Dr. Atef Fayez Qasrawi

This thesis was submitted in partial fulfillment of the requirements for

The Master's degree in Physics

June/2018

Formation and characterization of the In_2Se_3/CuO Heterojunctions

By

Reham Reda Kmail

This thesis was defended successfully on 7/7/2018 and approved by:

Committee members	Signature
1. Prof. Dr. Atef Fayez Qasrawi (Supervisor)	………………….
2. Assoc. Prof. Dr. Rushdi Kettaneh (External Examiner)	………………….
3. Assoc. Prof. Dr. Adli Saleh(Internal Examiner)	…………………..

Declaration

The work provided in this thesis, unless otherwise referenced, is the researcher's own work and has not been submitted elsewhere for any other degree or qualification.

Student's Name:

Signature:

Date:

Dedication

To My Parents

Acknowledgments

And said, "My Lord, enable me to be grateful for your favor which you have bestowed upon my parents and to do righteousness of which you approve, and admit me by your mercy in to the rank of your good righteous servant".

All thanks go to my god who give me the ability to finish this thesis and Peace and blessings be upon our Prophet Muhammad

I send all thanks for the righteous and mercy heart, to the candle that shine my heart, to the sun that he was like a light for my life and to the mountains of my ideas, to my lovely father.

To the tree in my heart that I bend over in it, to the chrysanthemum flower and the green wheat field, to my spring and my flowers my lovely mother.

To my language, to my words that sailings by his support, to my brother Jehad, who gave me power, success and inspiration of my heart.

To whom that build my glory, to the basis of my glory and spikes of happiness of my life, to those who were my sun thatshines my darkness, my brothers and sisters.

Words like in racing for forming a necklace that no one deserve it except you, to you who worked hard without waiting praise, to you, I send the best and specially thanks. Fly in our sky, always like stars, never disappear, we waiting its lightness and we feel happy when it shines in our sky every hour, his name deserve to be at the top, to our professor doctor Atef Qasrawi.

To the messengers of education, to the lamps of the way of life, to the instructors teachers and doctors.

Specially thanks to my university Arab American University, and all supervisors and administration in AAUJ.

To all people who help me for completing this thesis.

Finally, on behalf of me, thanks for any person believe in rightness and try for the sake of education and life, and for any one call the brotherhood, to Palestine (the name, the identity), to all people I love and I feel that I am one of them and they feel the same.

Abstract

Formation and characterization of the In_2Se_3/CuO Heterojunctions

In this thesis, we have discussed the formation and performance of $\gamma-$ In_2Se_3/CuO heterojunctions from structural, optical, dielectric and electrical point of view. The heterojunction device is prepared onto glass and aluminum substrates by the physical vapor deposition technique under vacuum pressure of 10^{-5} mbar. To guarantee the polycrystalline nature and the correct optimization of the $\gamma-$ In_2Se_3, the substrates are kept at 250 ^{o}C during the evaporation of indium selenide. The X-ray diffraction analysis on the films and its composers has shown that while the $\gamma-$ In_2Se_3 is of polycrystalline nature, the CuO is amorphous in its as grown form. The evaporation of CuO onto indium selenide resulted in strained nature of growth. On the other hand, the optical analysis which is carried out in the incident light wavelength range of 300-1100 nm have shown that the energy band gaps of the $\gamma-$ In_2Se_3 and CuO are of direct allowed electronic transitions type and the formation of the heterojunction is associated with band tails that extend in the band gap of both materials. The calculated valence and conduction band offsets are observed to be sufficient to actualize the needed quantum confinement for thin film transistor fabrication. As a result of the optical analysis, the dielectric spectra for the $\gamma-$ In_2Se_3/CuO heterojunctions are calculated and discussed. From the dielectric spectra, the optical conductivity parameters are estimated via Drude-Lorentz approach for conductivity spectra. The obtained optical conductivity parameters presented by drift mobility, free carrier density, plasmon frequency and electron-plasmon reduced frequency all exhibit values that are very attractive for thin film transistor technology. In addition, the heterojunction device which is prepared onto Al metal substrate displayed novel parameters presented by resonance-antiresonance phenomena and negative capacitance effect. These two features are also theoretically studied by the existing correlated barrier hopping and quantum mechanical tunneling theories. The resonance – antiresonance effects are analyzed in accordance with the Ershov model for electrical conduction. Furthermore, the current transport mechanism which is investigated by means of Schottky-Richardson mechanisms reveal a barrier height that is suitable for optoelectronic switching characteristics.

Keywords: Terahertz; InSe; CuO; Heterojunction; Plasmon; band offset.

List of contents

List of tables

List of figures

Chapter One

Introduction and Literature Survey

1.1Introduction and Literature Review

When talking about Semiconductor heterojunctions, we go back almost 50 years ago, which led to the emergency of many great achievements and many applications. It is the main title of many of the most advanced electronic and optoelectronic devices, like large-speed transistors and semiconductor lasers, which are used in information and communication technologies [1-5]. The heterojunction formed by semiconductors is important in modern semiconductor industry. A heterojunction can be formed between two dissimilar semiconductors, these semiconducting materials have different properties and most importantly different band gaps as opposed to a homo junction, where the high band gap selected for its transparency of light for the top layer and the low band gap that readily absorb light for the bottom layer. It is an important and useful base and advantageous to engineer the electronic energy bands in many solid-state device applications, like semiconductor lasers and other semiconductor devices, such as solar cells and transistors[6,7].

Heterojunctions can be organized into two types: the first one is isotype variety (n-n or p-p) and the second one is the anisotype variety (p-n). Anisotype heterojunction can be formed between two semiconductors having different types of conductivity and transparent (higher band gap), conducting substrate. On the other hand, isotype heterojunctions can be formed between two semiconductors that have the same type of conductivity [8].

The behavior of a semiconductor junction depends on the energy bands at the interface. We have three types of heterojunctions that can be organized into semiconductor interfaces, it appears in figure 1.1: (Type I) straddling gap formed by one material having lower E_c and higher E_v with small $E_{g.}$ (Type II) staggered gap location of lower and higher E_v are displaced so electron collected at larger E_v and detained different space. (Type III) broken gap where E_c on one side is lower than the E_v of the other side so E_{c1} overlap with E_{v2}at interface.

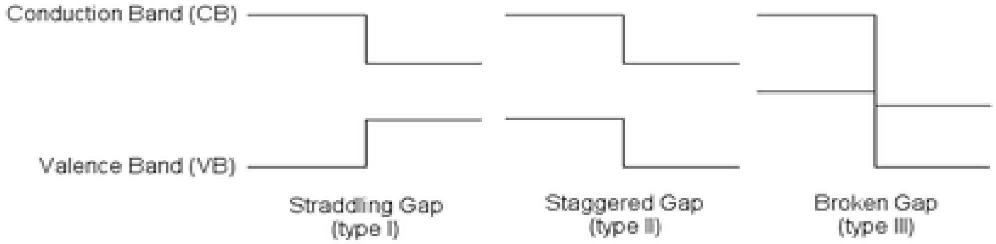

Figure 1.1: Types of heterojunctions depending on the energy bands

1.2 Applications of Heterojunctions

Many semiconductor materials which are used in the scientific regard are in heterojunction form, regardless whether it is single-crystal or polycrystalline [8]. Semiconductor heterojunctions have been used as an important application in many solid state devices, like solar cells, photo detectors, semiconductor laser and light-emitting diodes (LED) [6].

When talking about carbon-neutral energy source we keep in mind the sun, which is the largest source of this energy that has not been completely used, and unless solar energy is harvested with high efficiency are widely used solar cell devices based on inorganic semiconductors. These devices are of high cost to be economically employable. This is the main reason for the non-expansion of organic photovoltaic materials and devices, which leads us to many benefits such as low cost, flexibility and abundant availability.

In last year's, the organic solar cells based on heterojunction (HJ) active layers have attracted much importance because of the potential low cost, light weight, flexibility and their applications in large area devices. . Organic HJ solar cells contains conjugated polymers as electron donor materials and fullerene derivatives as electron acceptor materials, where it achieve great success in high power conversion efficiency (PCE) by optimizing the structure of conjugated polymers and device architecture [9].

To get well-controlled fabrication we use semiconductor heterojunctions with ideal lattice matching. These devices contains modulated-doped high-speed field-effect transistors, ultra-high-gain and high-speed bipolar transistors, efficient injection lasers and light-emitting diodes and sensitive photo-detecting structures [10].

In 1963 Herbert Kroemer a prominent scientist suggested the use of heterojunctions in lasers field, where population inversion could be greatly enhanced by heterostructures. Carriers can be confined and the laser can occur at room temperature with low threshold, by incorporating a smaller direct band gap material between two larger band gap layers. Semiconductor diode lasers used in CD and DVD players and fiber optic transceivers are manufactured using alternating layers of semiconductors to form lasing heterostructures[7].

In bipolar transistors to have a high forward gain and low reverse gain result, a heterojunction is used. This is important in high frequency operations (10 to 100 of GHz) and low leakage currents. This device is called a heterojunction bipolar transistor (HBT)[7]. On the other hand, in field effect transistors, heterojunctions are used to have high electron mobility transistors (HEMT) which can operate at large frequencies (over 500 GHz). Where the rise of electron mobilities depends on proper doping profile and band alignment where very small scattering can occur[7].

1.3 Crystal Structure

Staking by two different semiconductors we can form a heterojunction, but the characteristics of each semiconductor must be considered, some of these characteristics are electron affinity ($q\chi$), energy band gap (E_g) and lattice parameters (a, b and c). Table 1.1 illustrate these parameters for some materials. In table 1.2 we designed some possible heterojunctions and calculated the necessary parameters to form a heterojunction device.

Table 1.1: List of semiconductors with suitable properties for heterojunctions design.

Crystal	**a (A^o)**	**b(A^o)**	**c (A^o)**	**Eg(eV)**	**$q\chi$(eV)**
GaN	3.19[11]	3.19[11]	5.18[11]	3.17[11]	3.40[22]
Ga_2S_3	11.0[11]	9.57[11]	6.39[11]	3.40[11]	3.30[23]
InS	3.94[12]	---	---	3.30[17]	4.50[17]
MoO_3	3.96[13]	13.8[13]	3.69[13]	2.98[18]	6.70[18]
Fe_2O_3	8.34[14]	---	---	2.46[19]	5.50[24]
CuO	4.68[15]	3.42[15]	5.132[15]	1.35[20]	4.07[20]
ZnSe	5.66[11]	---	---	2.80[11]	0.19[25]
ZnS	5.40[11]	---	---	3.72[11]	3.90[26]
InSe	4.00[16]	4.00[16]	16.6[16]	1.45[21]	4.60[27]

Table 1. 2: Possible heterojunctions designs.

Crystal	**Mismatch (%)**	**C. thickness (A^O)**	**ΔE_c(eV)**	**ΔE_g (eV)**	**Δ E_v (eV)**
GaN/ Ga_2S_3	71.2	7.80	0.10	0.26	0.16
GaN/ InS	18.8	10.4	1.10	0.13	0.97
GaN/ MoO_3	19.4	10.2	3.30	0.19	3.11
GaN/ Fe_2O_3	61.7	6.70	2.10	0.71	1.39
GaN/ CuO	6.72	25.4	0.67	1.82	1.15
GaN/ ZnSe	43.6	6.49	3.21	0.37	2.84
GaN/ ZnS	40.9	6.60	0.50	0.55	0.05
GaN/ InSe	58.0	6.50	1.15	1.47	0.32
Ga_2S_3/InS	181	1.08	1.20	0.13	1.07
Ga_2S_3/ MoO_3	180	11.0	3.40	0.45	2.95
Ga_2S_3/ Fe_2O_3	32.4	12.6	2.20	0.97	1.23
Ga_2S_3/ CuO	224	0.76	0.77	2.08	1.31
Ga_2S_3/ ZnSe	95.9	2.95	3.11	0.63	2.48
Ga_2S_3/ ZnS	105	2.50	0.60	0.29	0.31
InS/ MoO_3	0.50	396	2.20	0.32	1.88
InS/ Fe_2O_3	52.7	7.90	1.00	0.84	0.16
InS/ CuO	15.2	11.2	0.43	1.95	1.52
InS/ ZnSe	30.3	9.30	4.31	0.50	3.81
InS/ ZnS	72.9	3.70	0.60	0.42	0.18
InS/ InSe	48.1	7.80	0.05	1.60	1.55
MoO_3/ Fe_2O_3	52.5	7.90	1.20	0.52	0.68
MoO_3/ CuO	15.7	10.8	2.63	1.63	1.00
MoO_3/ ZnSe	30.0	9.40	6.51	0.18	6.33
MoO_3/ ZnS	26.6	10.1	2.80	0.74	2.08

MoO_3/ InSe	47.8	7.90	2.15	1.28	0.87
Fe_2O_3/ CuO	143	1.10	1.43	1.11	0.32
Fe_2O_3/ ZnSe	47.3	5.90	5.31	0.34	4.97
Fe_2O_3/ ZnS	54.4	4.90	1.60	1.26	0.34
Fe_2O_3/ InSe	9.73	93.0	0.95	0.76	0.19
CuO/ ZnSe	39.5	7.10	3.88	1.45	2.43
CuO/ ZnS	36.6	7.37	0.17	2.37	2.20
CuO/ InSe	55.0	6.90	0.48	0.35	0.13
ZnSe/ ZnS	4.80	56.2	3.71	0.92	2.79
ZnSe/ InSe	25.5	14.9	4.36	1.10	3.26
InSe/CuO	6.10	34.9	0.53	0.10	0.43

Table1.2 demonstrates the properties of the crystal after the installation of the two semiconductors on each other. When choosing the suitable crystal you should see the properties of two semiconductors to be installed together like: lattice mismatch (Δ), critical thickness (t_c), conduction band offset (ΔE_c), energy valance band offset (ΔE_v) and energy band gap (ΔE_g), where [28]:

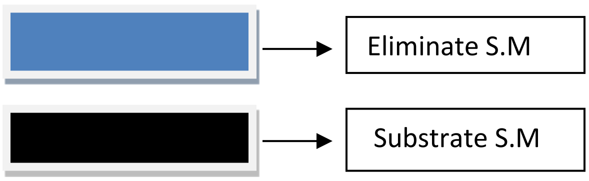

Figure 1.2: The shape of the device

$$\Delta = \left|\frac{a_e - a_s}{a_e}\right| \times 100\% \tag{1.1}$$

$$t_c = \frac{a_e}{2\Delta} \tag{1.2}$$

$$\Delta E_c = q\chi_s - q\chi_e \tag{1.3}$$

$$\Delta E_g = E_{gs} - E_{ge} \tag{1.4}$$

$$\Delta E_v = \Delta E_c - \Delta E_g \tag{1.5}$$

For thin film transistor technology, ΔE_v must be greater than 0.5 eV. In addition, the large lattice mismatch is necessary toactualize quantum confinement.

1.4 Problem Statement

The continuously accelerating communication technology is associated with many complicated problems that are related to electrical response and data transfer. Some designers went to the developments that improve the performance of data transfer via RF and microwave signals. Others carried out this issue with the help of combination of complicated and large size waveguide circuits. However, the recently developed mobile technology force new findings of low dimensional size very light in weight and reserve approximately no place on the mobile cards. Such requirements can be satisfied by the invention of new heterojunction devices being able to carry more than one duty at the same time. However, such type of heterojunction structures which are known as thin film transistors have series troubles during the performance because of its low dimensionality. For these reasons, here in this thesis we aim to fabricate a new type of heterojunction devices in which quantum confinement is actualized between the interfaced materials and relatively large energy band offsets to allow electronic transform via interbands between layers. The heterojunction device is expected to behave as a microwave and light signal resonators at the same time. It is also expected to behave as a rectifier that carry the duties of rectifications. The device is also expected to behave as a typical transistor that carry the traditional duties of the transistors.

In this study will design a heterojunction device through use of the InSe material and evaporate CuO to form InSe/CuO interface. Alternatively γ-In_2Se_3/CuO interface is produced through raising the substrate temperature to 250^oC before the heterojunction created. For this device we will study the optical properties to find the energy band gap in finally. After that we will handle the structural for this crystal to know the crystalline family to which they belong. Also study the impedance spectroscopy in two parts: conductance and capacitance. At the end of this study we will present the electrical characteristics of this device through studying the current-voltage mechanism.

The thesis will follow the sequence which starts with chapter one which displays the introduction and literature review taking into account the general features and characteristics of the heterojunctions. In chapter two, we will explain the basic principle and theoretical background that will guide this study. In chapter three, the steps of forming this device will be presented in details and equipment used to obtain the result of this study will be also reported. In chapter four, The results of the experiments are reported and discussed. Chapter five is the final chapter, where it deals with the summary of this study.

Chapter Two
Theoretical Background

2.1 Crystal Structure and Bravais Lattices

Crystal structure describes the ordered arrangement of atoms, ions or molecules in a crystalline material. The smallest group of particles in the material that constitutes the repeating pattern is called the unit cell of the structure. The repeating patterns are located at the points of the Bravais lattice. The crystal structure and symmetry play an essential role in determining many physical properties, like electronic band structure and optical transparency [29].

Bravais lattices or space lattices, describe the geometric arrangement of the lattice points, and the translational symmetry of the crystal. Also is an infinite array of discrete points in three dimensional space generated by a set of discrete translation operations described by [30]:

$$R = a_1 n_1 + a_2 n_2 + a_3 n_3 \tag{2.1}$$

Where n_i are any integers and a_i are known as the primitive vectors which lie in different directions.

Linear arrays of points can be combined in five distinguishable ways in order to create a two-dimensional Bravais lattices. These five types of arrangements are: square, rectangular, hexagonal, centered-rectangular and oblique unit cells.

2.2 Hexagonal Unit Cell

Hexagonal system**,** one of the principal systems of structures to which a given crystalline solid can be set. Components of crystals in this system are located by reference to four axis, three of equal length set at 120° to one another and a fourth axis perpendicular to the plane of the other three.

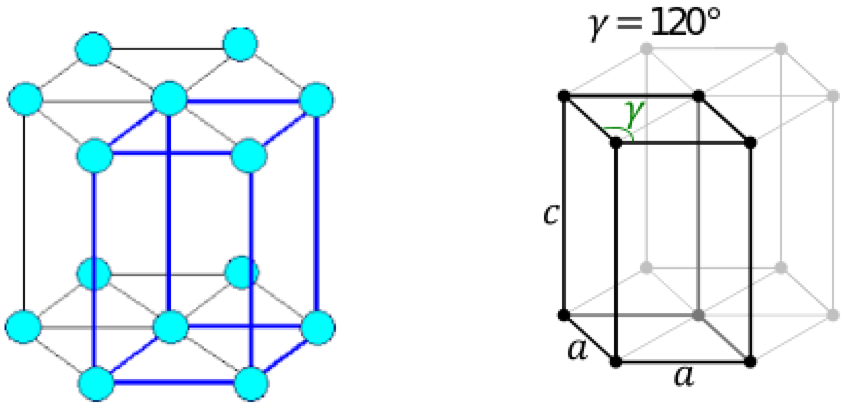

Figure 2.1: Hexagonal structure unit cell.

To calculate the lattice parameters for hexagonal structure we use [31]:

$$\frac{1}{d^2{}_{hkl}} = \frac{h^2 + hk + k^2}{a^2} \tag{2.2(a)}$$

$$\frac{1}{d^2{}_{\mathrm{hkl}}} = \frac{3}{4}\frac{(h^2 + hk + k^2)}{a^2} + \frac{l^2}{c^2} \tag{2.2(b)}$$

Where, d is interplanar distance, (hkl) are Miller indices of the reflection, a and c are the lattice parameters.

The lattice mismatches causes dislocation at is the surface and it is related to the maximum allowed epitaxial layer, it can be calculated using lattice parameters and epitaxial relationship [28]:

$$\Delta\,\% = \frac{\mathrm{a_e} - a_s}{\mathrm{a_e}} X\, 100\% \qquad (2.3)$$

Where$\mathrm{a_e}$ is the lattice constant of the epitaxial layer and a_s is the lattice constant of the substrate layer.

2.3 The X-Ray Diffraction

In this section, the method of the crystal structure analysis will be described. It is not the aim and the purpose of this section to give the details of the method but to describe the basic idea of X-ray diffraction. X-ray scattering technique gives information about the crystal structure and physical properties of materials and thin films. The properties and functions of materials depends on the crystal structures, so that the x-ray diffraction techniques widely used as an indispensable means in materials research and development. The maximum condition to clarify beam diffracted by atomic planes as shown in figure 2.2 are given by the Bragg equation [32]:

$$n\lambda = 2dsin\theta \qquad (2.4)$$

In this equation, *n* is an integer, λ is the wavelength of the incoming x-rays, *d* is the interplanar spacing between successive atomic planes and θ is the angle of the x-ray beam, that equals the angle of reflection.

The angle between X-ray beam and detector is set to the reflection condition for a certain lattice plane that is given by the Bragg equation. The crystal structure is determined by the Bragg-Brentano geometry in which the crystal is rotated with an angle θ and the detector is rotated with 2θ.

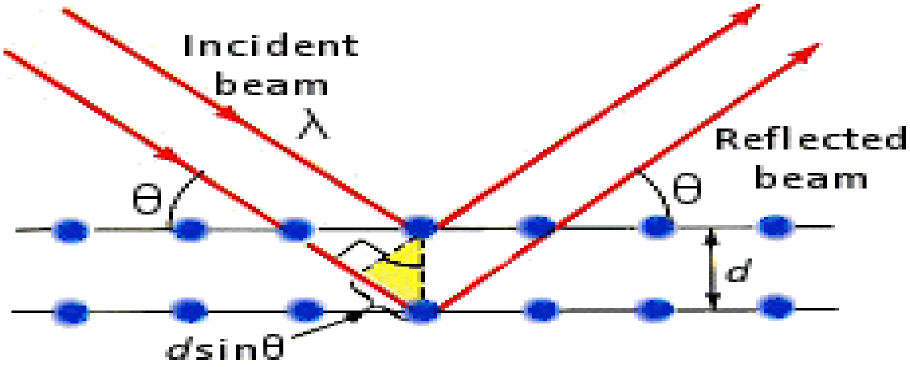

Figure 2.2: Bragg scattering on the lattice surface.

2.3.1 X-Ray Peak Broadening (β)

The other structural parameters can be found using Scherrer equation which is a formula relates the grain size of crystallites, in a solid to the broadening of a peak.The Scherrer's equation can be written as: [33]:

$$\beta cos\theta = \frac{k\lambda}{D} + 4\varepsilon sin\theta \tag{2.5}$$

B is the full width of the maximum intensity of peak in radians, θ is the Bragg angle in degrees, k is the constant related to crystallite shape and is mostly for grain size less than

200 nm equal to 0.94 [33], λ is the x-ray wavelength and equal 0.154 nm [34], *D* is the grain size and ε is the strain.

2.3.2 Grain Size (*D*)

Grain size refers to the size of a single crystal inside a material. A single grain can be composed of several crystallites. We can refer to equation (2.4) to explain the values of grain size and equal to [33]:

$$D = \frac{0.94\,\lambda}{\beta cos\theta} \qquad (2.6)$$

β is the full width of the maximum intensity of peak in radians, θ is the Bragg angle in degrees, λ is the x-ray wavelength and equal 0.154 nm [34].

2.3.3 Strain (*ε*)

Strain is defined as "deformation of a solid due to stress". It is also a measure of deformation representing the displacement between particles in the body relative to a reference length [35]. The strain can be written as [36]:

$$\varepsilon = \frac{\beta}{4tan\theta} \qquad (2.7)$$

β is the full width of the maximum intensity of peak in radians, θ is the Bragg angle in degrees.

Strain is of three types depending on the change produced in a body and the stress applied. The three types of strain are Longitudinal, Volume and Shearing Strains.

Longitudinal strain is the ratio of the change in length of a body to the original length of the body. Volume strain: It is the ratio of the change in volume of a body to its original volume. Shearing strain is the ratio of the displacement of a layer to its distance from the fixed layer. Strains are caused when too much force is placed on a material, this changes the properties of the material.

2.3.4 Stacking Faults (SF)

A stacking fault is a type of defect which characterizes the disordering of crystallographic planes. It is, thus, considered a planar defect. It represents any defect that alters the periodic sequence of layers, these defects may be a wrong layer inserted into the sequence, a change of the layer sequence or a different translation between two subsequent layers, the stacking faults can be determined from the formula [37]:

$$sf = \frac{2\pi^2\beta}{45\sqrt{3tan\theta}} \tag{2.8}$$

β is the full width of the maximum intensity of peak in radians, θ is the Bragg angle in degrees.

2.3.5 Dislocation Density (δ)

Dislocations (δ) are types of defects in crystals, it arises when atoms are out of position in the crystal structure, dislocations usually appears when a stress is applied, and it causes plastic deformation[38]: It can be calculated from the equation,

$$\delta = \frac{15\varepsilon}{aD}\left(\frac{\text{lines}}{\text{cm}^2}\right) \tag{2.9}$$

Where ε is the strain, a is the lattice constant and D is the grain size of crystallite. In accordance with this formula, the larger the strain the larger the defect density and the larger the grain size, the smaller the defect density.

2.4 Optical Properties in Semiconductor

The optical properties of semiconductors play a key role in the development of thin films. It forms the basis of the technology revolution. It is connected with transitions between the valance and conduction bands with consideration of interbands transitions. When a beam of light with intensity I_o inter a sample of thickness d, part of the light is absorbed with absorbance intensity I_A multiplied by a factor ($e^{-\alpha d}$), where α is the absorption coefficient. Other parts will be transmitted with intensity $I_{T,}$ reflected with intensity I_R and scattered with I_S. The mechanism is illustrated in figure 2.3. These intensities can be written as the following relation [39]:

$$I_0 = I_A + I_R + I_T + I_S \qquad (2.10)$$

The coefficients for absorbance$(A = I_A/I_0)$, reflectance $(R = I_R/I_0)$, transmittance $(T = I_T/I_0)$, and scattaring $(S = I_S/I_0$)are all add to give the total intensity of incident light as below:

$$A + R + T + S = 1 \qquad (2.11)$$

Because the scattering part is very small, so equation (2.11) can be rewritten as:

$$A + R + T = 1 \qquad (2.12)$$

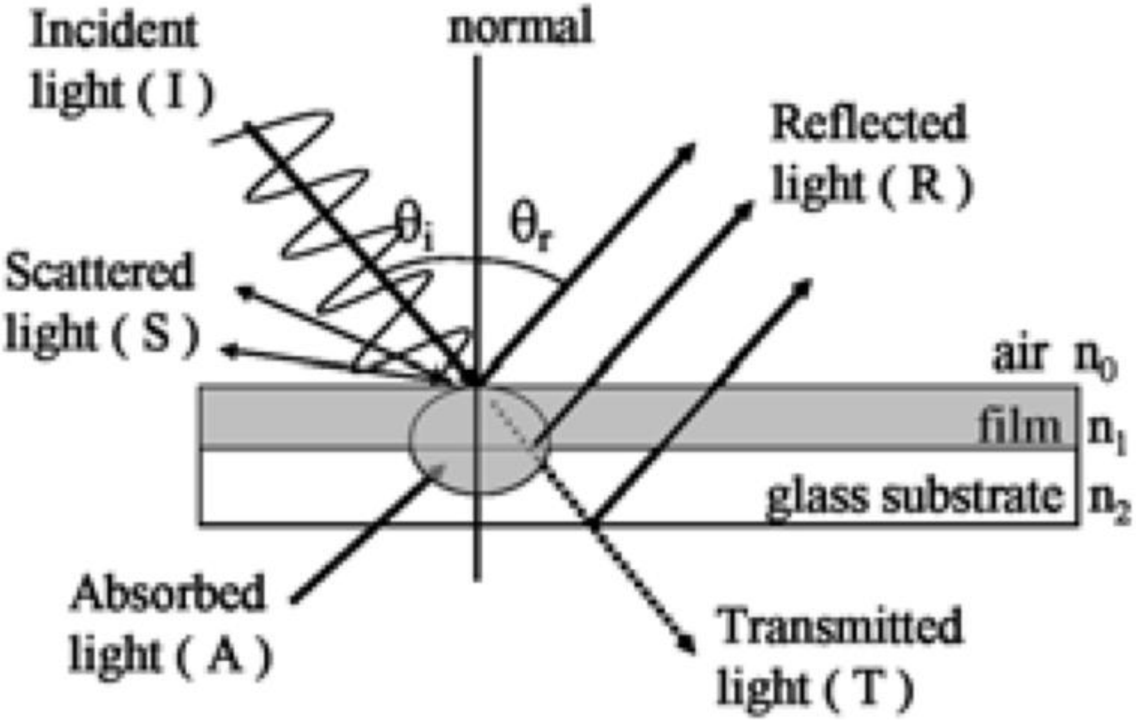

Figure 2.3: The optical mechanisms at the surface of material.

2.4.1 Absorption of Light in Matter

The electrons of atoms vibrate at particular frequencies. When a light wave has the same natural frequency of an electron, then the electrons of that atom tended to follow the vibrational motion, and then the electrons will absorb the energy of the light wave and transform it into vibration motion. During its vibration, the electrons interact with neighboring atoms in such a manner as to convert its vibration energy into thermal energy.

The absorption of light provide electrons with kinetic energy and set it free. In the absorption process, the electrons in the valance band are excited to the conduction band and leaving a hole in their place forming an electron-hole pair [40]. The value of energy required to generate electron-hole pair is at least equal to the energy band gap E_g [41].

2.4.2 Energy Band Gap (E_g)

In solid state physics, an energy gap, is the region where no electron states can exist. The band gap generally refers to the energy difference (in electron volts) between the top of the valence band (the valence band is the highest range of electron energies) and the bottom of the conduction band (conduction band is the lowest range of electron energies) in insulators and semiconductors (shown in figure 2.4). It is the energy required to promote a valence electron to become a conduction electron, which is free to move within the crystal lattice and charge carrier to produce electric current. If the valence band is completely full and the conduction band is completely empty, then electrons cannot move in the solid; however, if some electrons transfer from the valence to the conduction band, then current can flow. Therefore, the band gap is a major factor determining the electrical conductivity of a solid. Substances with large band gaps are generally insulators, those with smaller band gaps are semiconductors, while conductors either have very small band gaps or none, because the valence and conduction bands overlap [42].

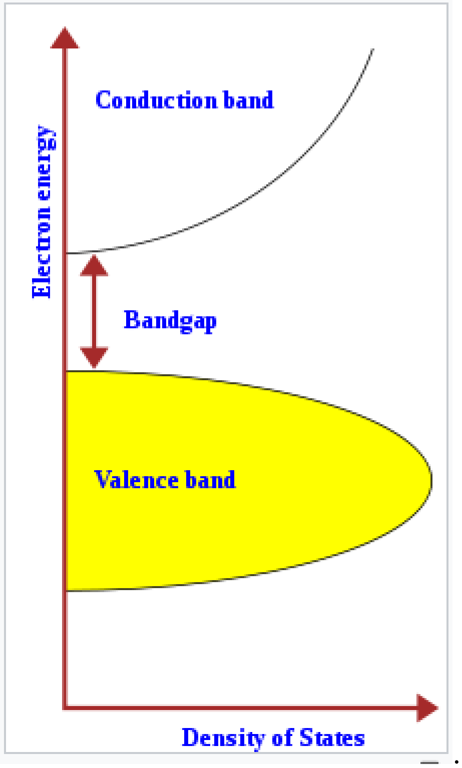

Figure 2.4: Semiconductor band structure.

We can find the energy band gap of semiconductor with the help of Tauc's relation [43]:

$$(\alpha E)^{1/p} = A\left(E - E_g\right) \qquad (2.13)$$

Whereα is the absorption coefficient, $E = hv$ is the photon energy, p is a constant related to the optical transition type and takes value of 2, 1/2, 3 and 3/2 for indirect allowed, direct allowed, indirect forbidden and direct forbidden electronic transitions, respectively, A is a constant defined by transition probability and depends on the material properties, E is the energy, E_g is the energy band gap between valance and conduction band. Tauc's plots $(\alpha E)^{1/P}$ with E to get the Eg from the intercept of the E-axis in the linear region of the absorption with the baseline.

To derive this equation we started from the energy band diagram shown in figure 2.5:

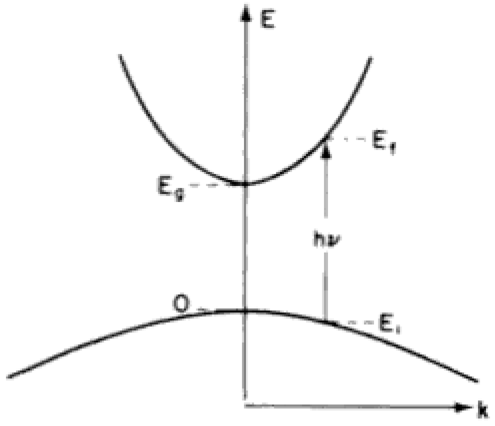

Figure 2.5: The energy band gap diagram.

From figure 2.5 the final energy equal to:

$$E_f = hv - E_i \tag{2.14}$$

Also, the initial and final energy states of the bands are given by [27]:

$$E_f - E_g = \frac{\hbar^2 k^2}{2m_e^*} \tag{2.15}$$

And,

$$E_i = \frac{\hbar^2 k^2}{2m_e^*} \tag{2.16}$$

The electron resides in the valance band up to conduction band when the incident photons interact with solids, where:

$$E_f = hv - |E_i| \tag{2.17}$$

Subtract Eg from both sides of equation (2.17) to get:

$$E_f - E_g = hv - E_g - |E_i| \tag{2.18}$$

Substitute equation (2.15) & (2.16) in equation (2.18) to give:

$$\frac{\hbar^2 k^2}{2m_e^*} = hv - E_g - \frac{\hbar^2 k^2}{2m_h^*} \tag{2.19}$$

Rewrite equation (2.19) in the form:

$$hv - E_g = \frac{\hbar^2 k^2}{2m_e^*} + \frac{\hbar^2 k^2}{2m_h^*} = \frac{\hbar^2 k^2}{2}\left[\left(\frac{1}{m_e^*}\right) + \left(\frac{1}{m_h^*}\right)\right] \tag{2.20}$$

The state density in an energy range extended from (*hv*) to (*hv+d(hv)*) have the form [27]:

$$N(hv)d(hv) = \frac{8\pi k^2 dk}{(2\pi)^3} \tag{2.21}$$

Rewrite equation (2.20) to give:

$$k^2 = \frac{2\left(hv - E_g\right)}{\hbar^2} m_r \tag{2.22}$$

m_r is the reduce mass, where:

$$\frac{1}{m_r} = \left(\frac{1}{m_e^*}\right) + \left(\frac{1}{m_h^*}\right) \tag{2.23}$$

Deriving equation (2.22) with respected to (*hv*), where k is a functional of hv to get :

$$kdk = \frac{m_r}{\hbar^2} d(hv) \tag{2.24}$$

Substitute equation (2.22) in equation (2.21) to give:

$$N(hv)d(hv) = \frac{16\pi(hv - E_g)m_r}{\hbar^2(2\pi)^3}dk \tag{2.25}$$

By employing equation (2.22) in equation (2.24) in the previous equation (2.25) the state density equation will be:

$$N(hv)d(hv) = \frac{16\pi\left(hv - E_g\right)}{\hbar^2(2\pi)^3}\frac{\mathrm{m_r^2}}{\hbar^2\left(\frac{\sqrt{(2\left(\mathrm{hv}-\mathrm{E_g}\right)\mathrm{m_r}}}{\hbar^2}\right)}d(hv) \tag{2.26}$$

Rewriting equation (2.26) in another form:

$$N(hv)d(hv) = \frac{(2m_r)^{\left(\frac{3}{2}\right)}}{2\pi^2\hbar^3}\left(hv - E_g\right)^{\frac{1}{2}}d(hv) \tag{2.27}$$

The absorption coefficient is linearly proportional to the initial and final states density N_i and N_f, respectively:

$$\alpha(hv) = A^*\left(hv - E_g\right)^{1/2} \tag{2.28}$$

Where $A^* = \frac{q^2\left(\frac{2m_h^* m_e^*}{m_h^* + m_e^*}\right)^{\frac{1}{2}}}{nch^2 m_e^*}$ (2.29)

$$= \frac{q^2(m_r)^{\frac{1}{2}}}{nch^2 m_e^*} \tag{2.30}$$

To generalize equation (2.28) rewrite it to become:

$$(aE)^{1/p} = A\left(E - E_g\right) \tag{2.31}$$

2.4.3 Energy Band Tail (E_e)

Band tail states usually exists near conduction and valence band edges. Band tail states arise as a consequence of materials disorder. They are much important in determining the electronic properties of semiconductor. It stand out as a result of impurities doping, such that the impurities levels that leads to forbidden gap deform the valance and conduction bands.

Transition involving impurity induced band tails exponentially increases the absorption spectra at photon energy less than energy gab. It is necessary to derive the relation that conducts the band tails to the absorption coefficient [44] and starting with:

$$N_f = N_0 \, e^{E/Ee} \tag{2.32}$$

Where N_f is the final state density and N_0 is the initial density of the doping .

$$\alpha(hv) = A \int_{E_v}^{hv-E_v} \sqrt{|E_V|} \exp\left(\frac{E}{E_e}\right) dE \tag{2.33}$$

To solve this integration substitute *E-hv* in *E* and we change following variables:

$$x = \frac{hv - E}{E_e} \tag{2.34}$$

Sub equation (2.34) in (2.33) to have the form:

$$\alpha(hv) = -Ae^{hv/Ee}(E_e)^{\left(\frac{3}{2}\right)} \int_{\frac{hv+Ev}{Ee}}^{\mathrm{E}_{\mathrm{V}/\mathrm{E_e}}} \mathrm{x}^{\frac{1}{2}} e^{-x} \, dx \tag{2.35}$$

$$\alpha(hv) = -Ae^{\frac{hv}{Ee}}(E_e)^{\left(\frac{3}{2}\right)}\left(\frac{1}{2}\pi^{\frac{1}{2}} - \int_0^{\mathrm{E_V}/\mathrm{E_e}} \mathrm{x}^{\frac{1}{2}}e^{-x}\,dx\right) \tag{2.36}$$

The width of the band tails near the top of valance band or the bottom of conduction band is given by:

$$E_e = \left(\frac{dln\alpha}{dhv}\right)^{-1} \tag{2.37}$$

So the equation can be used to determine the width of the band tails and is given by:

$$\alpha = \alpha_0 e^{\mathrm{E/Ee}} \tag{2.38}$$

$$\ln(\alpha) = \ln(\alpha o) + \frac{E}{E_e} \tag{2.39}$$

Where α is the absorption coefficient, E is the photon energy and E_e is the energy band tail. To find E_e we plot $ln\ (\alpha)$ versus E, where the intercept is $ln\ (\alpha_0)$ and the slope is $1/E_e$ from equation (2.39) so that the energy band tail equal 1/slope.

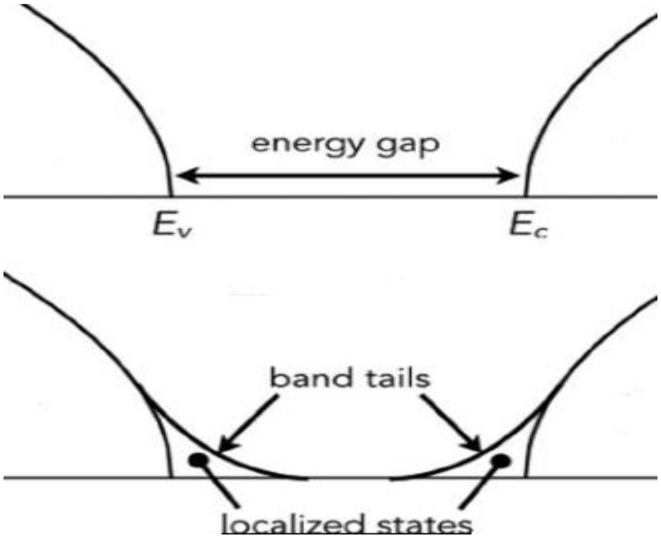

Figure 2.6: Semiconductor band tail structure.

Fig 2.6 demonstrates the localized states in materials. Localized states are states which are not extended enough because of materials disorder. There are many reasons that lead to the formation of these disorders. One of which is the inhomogeneous distribution of atoms in the semiconductor, in the oxide or both, inhomogeneous interface between semiconductor surface and oxide, inhomogeneous distribution of impurities doping or residual ones within the semiconductor, within the oxide, or both at the interface. [45]

2.4.4 Dielectric Spectra

The most important part in studying dielectric materials is that which relates to refractive index dispersion. The dispersion equation which is used to find the refractive index at particular optical wavelength is given by the following equation [46]:

$$N_{\text{complex}} = n(\lambda) + ik(\lambda) \tag{2.40}$$

$$= (\varepsilon_r + i\varepsilon_{im})^{\frac{1}{2}} \tag{2.41}$$

k(λ) is the extinction coefficient, and $\varepsilon_r \; and \; \varepsilon_{im}$ is the real and imaginary parts of the dielectric constants, respectively. The effective dielectric constant ε_{eff} is expressed in terms of the dielectric refractive index *n(λ):*

$$\varepsilon_{eff} = n^2(\lambda), \tag{2.42}$$

and in terms of the real part ε_r and imaginary ε_{im} parts, through the relation,

$$\varepsilon_{eff} = \varepsilon_r + i\varepsilon_{im} \tag{2.43}$$

Squaring both sides of equation (2.40), to write the refractive index *n(λ)* in terms of $\varepsilon_r \ and \ \varepsilon_{im}$:

$$n^2(\lambda) - k^2(\lambda) + i2n(\lambda)k(\lambda) = (\varepsilon_r + i\varepsilon_{im}) \tag{2.44}$$

By comparing the real and imaginary parts of equation (2.44), we find that:

$$n^2(\lambda) - k^2(\lambda) = \varepsilon_r \tag{2.45}$$

$$2n(\lambda)k(\lambda) = \varepsilon_{im} \tag{2.46}$$

The real and imaginary parts of dielectric constant can be written in terms of refractive index *n (λ)*as bellow,

$$\varepsilon_r = \varepsilon_{\text{eff}} - k^2 \tag{2.47}$$

$$\varepsilon_{im} = 2\sqrt{\varepsilon_{eff}}\, k. \tag{2.48}$$

An incident electromagnetic wave inside the dielectric material compromises an electric field [46]:

$$E_x = E_0 e^{i(k-\omega t)} \tag{2.49}$$

Where:

$$k = \left(\frac{\omega}{c}\right) N_{complex} \tag{2.50}$$

To determine $N_{complex}$, we recall that the electric field has an incident and reflected parts moves a long +z axis and –z axis, respectively:

$$E_x = E_1 e^{i(\frac{n}{c}-\omega t)} + E_2 e^{-i(\frac{n}{c}-\omega t)} \tag{2.51}$$

From E_x we can find the relation between E_0, E_1 and E_2:

$$E_0 = E_1 + E_2 \tag{2.52}$$

By using Maxwell's equations, we find the second relation between E_0, E_1 and E_2:

$$\nabla \times E = -\frac{\mu}{c}\frac{dH}{dt} = \frac{i\mu\omega}{c}H \tag{2.53}$$

Where H, is the tangential magnetic field component, c speed of light, μ permeability coefficient and $\omega$is the frequency.

By applying the curl relative to the x-component of the incident electric field:

$$\frac{dE_X}{dz} = \frac{i\mu\omega}{c}H_y \tag{2.54}$$

Equation (2.54) yields:

$$E_O k = E_1\frac{\omega}{c} - E_2\frac{\omega}{c} = E_0\frac{\omega}{c}N_{complex} \tag{2.55}$$

From equation (2.55):

$$E_1 - E_2 = E_0 N_{complex} \tag{2.56}$$

So, the reflection coefficient and the normal reflection condition can be written as:

$$R = \left|\frac{E_2}{E_1}\right|^2 \tag{2.57}$$

$$r = \frac{E_2}{E_1} \tag{2.58}$$

From equation (2.52) & (2.56):

$$E_2 = \frac{1}{2} E_0 \left(1 - N_{complex}\right) \tag{2.59}$$

and,

$$E_1 = \frac{1}{2} E_0 \left(1 + N_{complex}\right) \tag{2.60}$$

We can use equations (2.59) & (2.60) to rewrite the normal reflection coefficient indicated by equation (2.57):

$$R = \left| \frac{1 - N_{complex}}{1 + N_{complex}} \right|^2 = \frac{(1+n)^2 + k^{\,2}}{(1-n)^2 + k^2} \tag{2.61}$$

Alternatively, the reflectance R in terms of effective dielectric constant ε_{eff} and absorption coefficient α can be obtained from the relation,

$$R = \frac{\left(\left(\sqrt{\varepsilon_{eff}} - 1\right)^2 + k^2\right)}{\left(\sqrt{\varepsilon_{eff}} + 1\right)^2 + k^2} \tag{2.62}$$

Where,

$$k = \frac{\alpha \lambda}{4\pi} \tag{2.63}$$

We can rewrite equation (2.62) to obtain $\varepsilon_{eff}$from R as follows,

$$R\left(\sqrt{\varepsilon_{eff}} + 1\right)^2 + Rk^2 = \left(\sqrt{\varepsilon_{eff}} - 1\right)^2 + k^2 \tag{2.64}$$

By squaring $(\sqrt{\varepsilon_{eff}} + 1)$ and $(\sqrt{\varepsilon_{eff}} - 1)$ on both sides, and simplifying the equation we obtain:

$$\varepsilon_{eff} + \frac{2(R+1)}{(R-1)}\sqrt{\varepsilon_{eff}} + k^2 = 0 \tag{2.65}$$

This equation is solved to find a formula for ε_{eff} :

$$\sqrt{\varepsilon_{\text{eff}}} = \frac{-\frac{2(\text{R}+1)}{\text{R}-1} \pm \sqrt{\left(\frac{2(\text{R}+1)}{\text{R}-1}\right)^2 - 4k^2}}{2} \tag{2.66}$$

When we look at equation (2.66) we find that the two roots involved, these roots are squared and separated into two solutions:

$$\varepsilon_{\text{eff1}} = \left(\frac{-\frac{2(R+1)}{R-1} + \sqrt{\left(\frac{2(R+1)}{R-1}\right)^2 - 4k^2}}{2}\right)^2 \tag{2.67}$$

$$\varepsilon_{\text{eff2}} = \left(\frac{-\frac{2(R+1)}{R-1} - \sqrt{\left(\frac{2(R+1)}{R-1}\right)^2 - 4k^2}}{2}\right)^2 \tag{2.68}$$

2.4.5 Drude-Lorentz Model

Approximating the frequency dispersion of the permittivity of materials with simple analytical functions is of fundamental importance for understanding and modeling the optical response of materials and resulting structures. Drude and Lorentz developed a classical theory of refraction and dielectric constant of materials with frequency of light. The model is based on treating electrons as damped harmonically particles undergoing external electric fields[47]. The Drude-Lorentz model describes the dielectric dispersion.

Starting from the equation of motion for system of particles subjected to a resistive force during motion, we can establish the equation of motion as below,

$$m_0\frac{d^2x}{dt^2}+m_0\gamma\frac{dx}{dt}+m_0\omega_0^2x=-eE \qquad (2.69)$$

Where γ is the damping (resisting) coefficient and is inversely proportional to the collision time (τ), e is the electric charge of the electron and E is the electric field of the light. The right hand side is the driving force due to the AC electric field of the light, and the left hand side is the acceleration, the damping and restoring force, respectively.

The interaction of the atoms depends on the frequency ω and the time dependent of the electric field is:

$$E(t)=E_0\cos(\omega t+\Phi)=E_0(\exp(-i\omega t-\Phi)) \qquad (2.70)$$

E_0 is the amplitude of the time dependent electric field and Φ is the phase of light.

The AC electric field will drive oscillation at its own frequency, we substitute equation (2.69) into (2.70), the solution is:

$$x(t)=x_0\left(exp\left(-i\omega t-\Phi'\right)\right) \qquad (2.71)$$

$x_0$is the amplitude and Φ' is the phase of the oscillation. We can add the phase factor of equation (2.70) and (2.71) to the amplitude by both E_0 and x_0 to be complex numbers. We then substitute E (t) =$E_0\mathrm{e}^{-\mathrm{i}\omega\mathrm{t}}$in equation (2.69), and x(t)=$x_0\mathrm{e}^{-\mathrm{i}\omega\mathrm{t}}$. This leads to:

$$-m_0\omega^2x_0\mathrm{e}^{-\mathrm{i}\omega\mathrm{t}}-im_0\gamma\omega x_0\mathrm{e}^{-\mathrm{i}\omega\mathrm{t}}+m_0{\omega_0}^2x_0\mathrm{e}^{-\mathrm{i}\omega\mathrm{t}}=-eE_0\mathrm{e}^{-\mathrm{i}\omega\mathrm{t}} \qquad (2.72)$$

Which implies that:

$$x_0 = \frac{-\frac{eE_0}{m_0}}{\omega_0^2 - \omega^2 - i\gamma\omega} \qquad (2.73)$$

The displacement of the electron produce a dipole moment p(t), if N is the number of atoms per unit volume, the resonant polarization is given by:

$$p(resonant) = Np = -Nex$$

$$= \frac{Ne^2}{m_0}\frac{1}{\omega_0^2 - \omega^2 - i\gamma\omega}E \qquad (2.74)$$

The magnitude of the R_{esonant} is small unless the frequency is close to ω_0. The complex relative dielectric constant ε_r, and the electric displacement D of the medium is related to $E$and P through:

$$D = \varepsilon_0 E + P \qquad (2.75)$$

We split the polarization into a non-resonant background and resonant term and driven response of the oscillator:

$$D = \varepsilon_0 E + P(background) + P(resonant) = \varepsilon_0 E + \varepsilon_0 xE + P(resonant) \quad (2.76)$$

The relative dielectric constant is defined by:

$$D = \varepsilon_0 \varepsilon_r E \qquad (2.77)$$

Combine equation (2.74), (2.75) and (2.76) with (2.77) to obtain:

$$\varepsilon_r(\omega) = 1 + x + \frac{Ne^2}{\varepsilon_0 m_0}\frac{1}{\omega_0^2 - \omega^2 - i\gamma\omega} \qquad (2.78)$$

This can split into real and imaginary parts, to become:

$$\varepsilon_1(\omega) = 1 + x + \frac{Ne^2}{\varepsilon_0 m_0} \frac{\omega_0^2 - \omega^2}{(\omega_0^2 - \omega^2)^2 + (\gamma\omega)^2} \tag{2.79}$$

$$\varepsilon_2(w) = \frac{Ne^2}{\varepsilon_0 m_0} \frac{\gamma\omega}{(\omega_0^2 - \omega^2)^2 + (\gamma\omega)^2} \tag{2.80}$$

The generalized form of Drude-Lorentz model is given by the equation [48]:

$$\varepsilon_{im} \sum_{i=1}^{k} \frac{\omega_{pei}^2 \omega}{\tau_i((\omega_{ei}^2 - \omega^2)^2 + \omega^2 \tau i^{-2})} \tag{2.81}$$

Where i refer to number of linear oscillators , ω_{pe} is the Plasmon frequency and equal to:

$$\omega_{pe} = \sqrt{\frac{4\pi n e^2}{m^*}} \tag{2.82}$$

n is the free electron density and m^* is the effective mass of free electron, ω_e is the resonant frequency and γ is the damping rate.

2.5 Impedance Spectroscopy in Semiconductors

Impedance spectroscopy is a method to find the electronic density of states in semiconductor materials. The method consists in measurement of the charge transfer resistance, conductance, capacitance and other of a semiconductor interface at different frequencies, it is a basic tool for studying semiconductor electrodes, it leads to find information about the structure of the electronic interface.

2.5.1 Alternating Current Conductivity

In many amorphous semiconductors and insulators, the AC conductivity obeys the universal and important law, which depends on temperature and relative frequency (ω)[49]:

$$\sigma_{ac}(\omega, T) = A\omega^s \tag{2.83}$$

Where $\omega = 2\pi f$ is the angular frequency of the applied AC field, A is the constant dependent on temperature, s is the frequency exponent and take value ($0 \leq s \leq 1$) and also dependent on temperature, it called Jonscher's coefficient.

In particular, the AC conductivity dependence on the linear frequency, when the density of state n (τ) is proportional to $1/\tau$, the relaxation time is given by this relation[49]:

$$\tau = \tau_0 e^{(\zeta)} \tag{2.84}$$

ζ random variable that arises from probability calculation:

$$\zeta = 2\alpha R_\omega \tag{2.85}$$

α is a decay parameter for wave functions employed to describe the localized length of state and$R_\omega$is the hopping distance at a particular frequency (ω) as given in equation[50]:

$$R_\omega = \frac{\ln\left(\frac{v_{ph}}{\omega}\right)}{2\alpha} \tag{2.86}$$

Where v_{ph} is the phonon frequency and equal $1/\tau$.

In order to explain the behavior of the AC electrical conductivity, we have many models proposed for amorphous semiconductors. Some of these models are: quantum mechanical tunneling (QMT) model and correlated barrier hoping (CBH) model [51].

2.5.2 Quantum-Mechanical Tunneling Model (QMT)

Quantum mechanical tunneling is the phenomenon where a particle tunnels through a barrier. The tunneling phenomenon is majority carrier effect. A tunneling current occurs when electrons are not able to move over the energy barrier. From classical point of view, if the electron doesn't have enough energy to move over a barrier the electron cannot pass. In the limit of large barriers, the probability of tunneling decreases for higher and wider barriers. The carrier tunnel through a potential barrier if the barrier is sufficiently thin [28].

The mechanism of quantum mechanical tunneling is employed to explain the AC conductivity of many semiconductors. To understand the behavior of conductivity as a function of signal frequency, the conductivity is analyzed in accordance with the existing theories of electrical conduction. The AC conductivity for this model takes the form [3, 52]:

$$\sigma_{tun}(\omega) = \frac{\pi^4}{24} e^2 kT\alpha^{-1} \left(N\left(E_f\right)\right)^2 \omega\, R_{\omega}^4 \tag{2.87}$$

Where N (E_f) is the density of localized states near the Fermi level, α is the decay parameter, $R_{\omega}$is the tunneling distance and is given by equation (2.86).

On the other hand, the frequency exponent s for the quantum mechanical tunneling process to dominate takes the form, [50]:

$$s = 1 - \frac{4}{\frac{1}{\ln(\omega\tau_0)}} \tag{2.88}$$

Where τ_o is the relaxation time and equal to (10^{-9}-10^{-7}) s. The domination of tunneling process should be valid at s equal (0.5-1.0).

To derive the AC conductivity for the quantum mechanical tunneling model, we begin from the general formula for AC conductivity [53]:

$$\sigma_{ac}(\omega) = N_p \int c(\tau) \frac{\omega^2\tau}{1+\omega^2\tau^2} P(\tau) d\tau \tag{2.89}$$

N_p is the number of dipoles, ω is the angular frequency, τ is the relaxation time, c(τ) is the polarizability and P(τ) is the probability function that describe the relaxation time.

The first relation of the AC conductivity was expressed in equation (2.83), after that this equation conducted to hop of electron near the Fermi energy in semiconductors, so in this case (hopping) N_p is the number of carriers, and the polarizability c (τ) is given by [53]:

$$c(\tau) = \frac{(eR)^2}{12K_BT\left(\cosh\left(\frac{\delta E}{2K_BT}\right)\right)^2} \tag{2.90}$$

R is the hopping distance, K_B is the Boltzmann constant, T is the temperature and $\delta E = (E_f - E_i)$ is the average separation of energy levels.

The hopping or tunneling rate ($\Gamma = 1/\tau$) from a state of energy $E_i$toE_f ($E_f > E_i$) for n-type is equal to:

$$\Gamma = v_{ph} \exp\left(-2R\alpha - \frac{\delta E}{k_BT}\right) \tag{2.91}$$

$v_{ph} = \frac{1}{\tau_0}$ is the photon frequency and α is a decay parameter**.** Then we can derive τ as function of R as below,

$$d\tau = 2v_{ph}^{-1}\alpha \exp(2R\alpha)\, dR = 2\tau\alpha dR \tag{2.92}$$

The probability function of distribution of the relaxation time P(τ) in equation (2.89) can be written in another form in the cases of random distribution sites N :

$$p(\tau)d\tau = p(R)dR = 4\pi NR^2 dR \tag{2.93}$$

By substituting equation (2.90) & (2.92) in equation (2.89):

$$\sigma_{ac}(\omega) = \frac{\pi NN_p e^2\omega}{\alpha 6K_BT}\int R^4 \frac{\omega^2}{1+\omega^2\tau^3} d\tau \tag{2.94}$$

We can write $p = \left[N\left(E_f\right)K_BT\right]^2$, because the number of carriers for hopping near E$_f$ are given by $(N(E_f)K_BT)$. Also $(\omega^2/(1+\omega^2\tau^2)$ is like the δ-function at $(\omega\tau = 1)$, taking out R from the integral. The formula of R_ω is shown in equation (2.86) so the integral in equation (2.94) becomes:

$$\int (\frac{\omega^2}{1+\omega^2\tau^2})\frac{d\tau}{\tau} \approx \frac{\tau}{2} \tag{2.95}$$

Substituting equation (2.86), (2.93) & (2.95) in equation (2.94) to get the equation of AC conductivity:

$$\sigma_{tun}(\omega) = \frac{\pi^4}{24}e^2kT\alpha^{-5}\left(N\left(E_f\right)\right)^2 \omega\left[\ln\left(\frac{v_{ph}}{\omega}\right)\right]^4 \tag{2.96}$$

When we compared equation (2.96) with equation (2.87) for the quantum mechanical tunneling (QMT) model, we see that the both equation agrees with each other.

2.5.3 Correlated Barrier Hopping Model (CBH)

The CBH is another conduction mechanism which could dominate in semiconductor devices. In CBH the electron can hop from the barrier, and the conductivity decreases through the change in the thickness of the barrier . To determine the conductivity by CBH we used proceed as below [50]:

$$\sigma_{CBH}(\omega) = \sigma_H(\omega) + \frac{\sigma_L(\omega) - \sigma_H(\omega)}{1 \, + \, \omega^2\tau^2} \tag{2.97}$$

In this equation, $\sigma_L$and $\sigma_H$means high and low frequency saturation conductivities, respectively.The random variable ζ in equation (2.85) in the hopping term is:

$$\zeta = \frac{\mathrm{W}}{K_B T} \tag{2.98}$$

W is the hopping barrier height and equal to:

$$W = W_M - \frac{2e^2}{\pi\varepsilon\varepsilon_0 R} \tag{2.99}$$

W_M is the maximum barrier height, ε and ε_0 are the dielectric constants for the material and free spaces, respectively, and R is the distance between the two neighbor sites.

The AC conductivity for the correlated barrier hopping model in a narrow band limit ($\Delta_0 \ll K_B T$) is defined as [53, 54]:

$$\sigma(\omega) = \frac{\pi^3}{12} N^2 \varepsilon\varepsilon_0 \omega R_\omega^6 \tag{2.100}$$

Where N the concentration of pair sites, and the hopping distance R_ω is given by [54]:

$$R_\omega = \frac{2e^2}{\pi\varepsilon\varepsilon_0\left(W_M + K_B T ln(\omega\tau_0)\right)} \tag{2.101}$$

For (CBH) model, the frequency exponent s is equal:

$$s = 1 - \frac{6K_B T}{W_M + K_B T ln(\omega\tau_0)} \tag{2.102}$$

From the approximation ($\Delta_0 \ll K_B T$) yield to the large value of $W_M/(K_B T)$, then equation (2.102) becomes [53]:

$$s = 1 - \frac{6K_B T}{W_M} \tag{2.103}$$

The frequency exponent s for the (CBH) model depends on the temperature in the linearly relationship (when the temperature increases the frequency exponent will increase).

When the conductivity depends on high and low frequency values, the correlated barrier hopping (CBH) model AC conductivity takes the form [52]:

$$\sigma_{ac}(\omega) = \sigma_{ac\,H}(\omega) + \frac{[\sigma_{ac\,L}(\omega) - \sigma_{ac\,H}(\omega)]}{1 + (\omega\tau)^2} \tag{2.104}$$

To get an integrated picture for conductivity mechanism, we consider the contribution from both CHB and tunneling conductivities to the total conductivity through the relation [50]:

$$\frac{1}{\sigma(w)} = \frac{1}{\sigma(\omega)_{Tun}} + \frac{1}{\sigma(\omega)_{CBH}} \tag{2.105}$$

2.5.4 AC Capacitance

The capacitance is the ability to store electrical energy. Almost all things, can store some electrical energy and therefore have capacitance. It is very important part in studying many amorphous semiconductors and insulators. The AC capacitance depends on frequency as expressed in Qasrawi modified Ershov equation [50]:

$$C(\omega) = C_0 + \frac{a_n\tau_n}{1+(\omega-\omega_n)^2\tau_n^2} - \frac{a_p\tau_p}{1+\left(\omega-\omega_p\right)^2\tau_p^2} \qquad (2.106)$$

Where C$_0$ is the static capacitance, $a_n\ and\ a_p$ are the parameters, $\omega_n\ and\ \omega_p$ are the Plasmon frequencies for n-type material and p-type material, respectively, and τ_0, $\tau_n\ and\ \tau_p$ are the relaxation times.

The Qasrawi modified Erchov equation is derived as below [55]:

$$C(\omega) = \frac{1}{\omega} Im[Y(\omega)] \qquad (2.107)$$

Where:

$$Y(\omega) = \frac{\delta I(\omega)}{\delta V(\omega)} \qquad (2.108)$$

If heterojunctions have the small signal harmonic current and small signal voltage$\delta I\ and\ \delta V$ are proportional to$\sim e^{iwt}$. Let us consider the transient current in a semiconductor device in response to an applied voltage. Since,

$$\delta V(t) = V(t) - V(0-) = V\Delta\theta(t) \quad ,\text{then} \qquad (2.109)$$

$$\delta I(t) = I(t) - I(0-) = [I(t) - I(\infty)]\theta(t) + [I(\infty) - I(0-)]\theta(t). \tag{2.110}$$

Here $\theta(t)$ is unity step function, The quantities of "+" and "-" superscripts denote single-sided values of the discontinuous functions for example: $(0-) = \lim_{t\to 0} V(t), t < 0$, let the transient current equal $\delta J(t) = [I(t) - I(\infty)]\theta(t)$ so that $\delta J(t) \to 0\ as\ t \to \infty$.

Substituting equation (2.109) & (2.110) in equation (2.108) and noting that$\int_{-\infty}^{\infty} \theta(t) e^{iwt} = \frac{1}{i\omega}$:

$$Y(\omega) = i\omega \int_0^\infty \delta I(t) e^{i\omega t}\, dt \tag{2.111}$$

Separation of real and imaginary parts in equation (2.111) to get the formula of capacitance:

$$C(\omega) = \frac{1}{\Delta V}\int_0^\infty \delta J(t)\cos(\omega t)\, dt \tag{2.112}$$

In general:

$$\delta J(t) = C_0 \Delta V \delta(t) + \delta j(t) \tag{2.113}$$

Where C_0 is the static capacitance and $\delta(t)$ is the delta function.

Rewriting equation (2.112) in terms of$\delta j(t)$:

$$C(\omega) = C_0 + \frac{1}{\Delta V}\int_0^\infty \delta j(t)\cos(\omega t)\, dt \tag{2.114}$$

Integrating equation (2.114) by parts we get,

$$C(\omega) = C_0 + \frac{1}{\omega \Delta V} \int_0^\infty [-\frac{d\delta j(t)}{dt}] \sin(\omega t)\, dt \tag{2.115}$$

The capacitance equation has two parts (C_0 *and* C_1). By comparing equations (2.114) & (2.115):

$$C_1 = \frac{1}{\Delta V} \int_0^\infty \delta j(t) \cos(\omega t)\, dt = \frac{1}{\omega \Delta V} \int_0^\infty [-\frac{d\delta j(t)}{dt}] \sin(\omega t)\, dt \tag{2.116}$$

If we assume two different frequency domains (ω-ω_n) and (ω-ω_p), where ω_n and ω_p are the domain frequencies in the n-region and p-region, respectively [48]and if we rewrite equation (2.116), it take the form,

$$C_1 = \frac{1}{\Delta V} \int_0^\infty \delta j(t) \cos(\omega - \omega_{n,p}) t\, dt = \frac{1}{\omega \Delta V} \int_0^\infty [-\frac{d\delta j(t)}{dt}] \sin(\omega - \omega_{n,p}) t\, dt \tag{2.117}$$

To explain these considerations, let us consider a simple general type of transient response composed of negative and positive exponential components:

$$\delta j(t) = \Delta V \left(a_n \exp\left(-\frac{t}{\tau_n}\right) - a_p \exp\left(-\frac{t}{\tau_p}\right)\right) \tag{2.118}$$

By substituting equation (2.118) in equation (2.117) and integrate we get,

$$C_1 = \frac{a_n \tau_n}{1 + (\omega - \omega_n)^2 \tau_n^2} - \frac{a_p \tau_p}{1 + (\omega - \omega_p)^2 \tau_p^2}\ . \tag{2.119}$$

Where $\mathrm{C}(\omega) = C_0 + C_1$, so that the final formula for the capacitance in terms of frequency is:

$$C(\omega) = C_0 + \frac{a_n \tau_n}{1 + (\omega - \omega_n)^2 \tau_n^2} - \frac{a_p \tau_p}{1 + \left(\omega - \omega_p\right)^2 \tau_p^2} \qquad (2.120)$$

The subscript in the above equation relate to n or p-type semiconductor.

2.6 Direct Current Conduction Mechanism

The current across a metal-semiconductor junction is due to majority carriers. Three distinctly different mechanisms can exist: diffusion of carriers from the semiconductor into the metal, thermionic emission of carriers across the Schottky barrier and quantum-mechanical tunneling through the barrier. The thermionic emission theory on the other hand postulates that only energetic carriers, which have an energy equal to or larger than the conduction band energy at the metal-semiconductor interface can leave the barrier and go to the conduction band and contribute to the current flow. Quantum-mechanical tunneling through the barrier takes into account the wave-nature of the electrons, allowing them to penetrate through thin barriers. In a given junction, a combination of all three mechanisms could exist. The analysis reveal that the diffusion and thermionic emission currents can be derived and we suppose that there is a flow of electrons in the x direction [56]:

$$J_{\mathrm{x}} = \int \mathrm{q}\, \mathrm{n(E)} \mathrm{v_x(E)dE} \qquad (2.121)$$

Where $J_{\mathrm{x}}$the current density, q is the charge of electron, $\mathrm{n(E)}$ is the density of electrons and $\mathrm{v_x(E)}$ is the speed of electron. This integral perform in all free electrons that can move from barrier to conduction band.

From statistical physics point of view, the density of particles:

$$n(E) = g(E)f(E) \tag{2.122}$$

Where $g(E)$ is the density of states and $f(E)$ is the probability of a selected state energy E to be occupied.

Both functions can be written as a Fermi-Dirac statistics because the electrons are half spin particles. Hence,

$$g(E) = \frac{8\sqrt{2}\pi}{h^3} m^{\frac{3}{2}} \sqrt{E} \tag{2.123}$$

$$f(E) = \frac{1}{1 + \frac{\exp(E - E_f)}{kT}} \tag{2.124}$$

Where h is Plank constant, k is Boltzmann constant and E_f is Fermi energy. Only electron of highest energy (E>>E_f) can move from barrier to conduction band so:

$$f(E) = exp \frac{-(\mathrm{E} - E_f)}{kT} \tag{2.125}$$

We can rewrite equation (2.122):

$$n(E)dE = \frac{8\sqrt{2}\pi}{h^3} m^{\frac{3}{2}} \sqrt{E} exp \frac{-(\mathrm{E} - \mathrm{E_f})}{kT} dE \tag{2.126}$$

The kinetic energy is a function of velocity:

$$E = \frac{1}{2} m v^2 \tag{2.127}$$

$$\sqrt{E} dE = \frac{1}{\sqrt{2}} m^{3/2} v^2 dv \tag{2.128}$$

Insert equation (2.128) in equation (2.126):

$$n(E)dE = \frac{8\pi}{h^3} m^3 \exp(\frac{-(\mathrm{E} - \mathrm{E_f})}{kT})\, v^2 dv \qquad (2.129)$$

Insert equation (2.129) in equation (2.121):

$$J_x = \int q v_x(E) \frac{8\pi}{h^3} m^3 exp \frac{-(\mathrm{E} - \mathrm{E_f})}{kT} v^2 dv \qquad (2.130)$$

$$J_x = \int q v_x(E) \frac{8\pi}{h^3} m^3 exp\left(-\frac{E}{kT}\right) \exp(\frac{E_f}{\mathrm{kT}})\; v^2 dv \qquad (2.131)$$

$$J_x = \frac{2\mathrm{q}}{\mathrm{h}^3} \mathrm{m}^3 \exp(\frac{E_f}{\mathrm{kT}}) \int v_x(E)\, exp\left(-\frac{E}{kT}\right)\; 4\pi v^2 dv \qquad (2.132)$$

Because only electron with velocity higher than $v_{x,min}$ will leave metal, so the integral over v_x start from minimum velocity, and insert equation (2.127) and energy is a function of velocity component in three dimension so equation (2.132) become:

$$J_x = \frac{2\mathrm{q}}{\mathrm{h}^3} \mathrm{m}^3 \exp\left(\frac{E_f}{\mathrm{kT}}\right) \int_{v_{x,min}}^{\infty} v_x \exp\left[-\frac{mv_x^2}{2kT}\right] dv_x \int_{-\infty}^{\infty} \exp\left[-\frac{mv_y^2}{2kT}\right] dv_y \int_{-\infty}^{\infty} \exp\left[-\frac{mv_z^2}{2kT}\right] dv_z \quad (2.133)$$

To solve this integral we used:

$$\int_{-\infty}^{\infty} \exp(cx^2)\, dx = \sqrt{\frac{\pi}{c}} \qquad (2.134)$$

So that:

$$J_x = \frac{2\mathrm{q}}{\mathrm{h}^3} \mathrm{m}^3 \exp\left(\frac{E_f}{\mathrm{kT}}\right) \exp\left(\frac{-E}{\mathrm{kt}}\right) \frac{kT}{m} \sqrt{(\frac{2\pi kT}{m})} \sqrt{\left(\frac{2\pi kT}{m}\right)} \qquad (2.135)$$

$$J_x = \frac{4\pi \mathrm{q} m k^2}{\mathrm{h}^3} \mathrm{T}^2 \exp\left(\frac{E_f - E}{\mathrm{kT}}\right) \qquad (2.136)$$

$$J_x = \mathrm{A}^{**}\mathrm{T}^2 \exp\left(\frac{-U}{\mathrm{kT}}\right) \tag{2.137}$$

Where A** is Richardson constant and equal:

$$\mathrm{A}^{**} = \frac{4\pi \mathrm{q} m k^2}{\mathrm{h}^3} = 120 m^* \ \mathrm{A/m^2k^2} \tag{2.138}$$

$m^*$is the effective mass. Since,

$$U = E - E_f = \frac{q\left(\varphi_0 - \frac{\sqrt{qE}}{4\pi\epsilon_0\varepsilon_r}\right)}{kT} \tag{2.139}$$

and $J_x = I/A$. Then, the final form for the Richardson Schottky current is:

$$I = AA^{**}T^2 \exp\left[\frac{q\left(\varphi_0 - \frac{\sqrt{qE}}{4\pi\epsilon_0\varepsilon_r}\right)}{kT}\right] \tag{2.140}$$

Where A is the area of the contact point, T is the temperature, E is the electric field.

We can write equation (2.140) in another form as below:

$$I = AA^{**}T^2V^{\gamma}e^{q\varphi_b/kT} \tag{2.141}$$

$$\varphi_b = \varphi_0 - \text{ῄ}\left(\frac{e\square}{4\pi\epsilon_0\varepsilon_r}\right)^{\frac{1}{2}}\left(\frac{\sqrt{V}}{\sqrt{w}}\right) \tag{2.142}$$

With $, \gamma\ and \square$ are integer numbers,ῄ is ideality factor, ϵ_0 is the permittivity of free space, ε_r is the optical dielectric constant, V is the applied voltage, w is the depletion width and φ_0 is the Schottky barrier height. For $\gamma = 0$, this means that the theory is Richardson Schottky type, at $\gamma = 2$ the Trap assisted conduction dominates, at$\gamma = 1/2$ Poole Frenckel effect and at $\gamma = 3/2$ is Childs effect.

Chapter Three

Experimental Details

3.1 Substrate Cleaning

At first, the glass substrate to be used for thin film deposition is cleaned in several steps which include the use of alcohol to remove impurities, dust and contaminants from the surface. The cleaning by alcohol is followed by ultrasonic shaking in distilled water at 70 ^{o}C for 30 min and then, the glass substrate drying.

3.2 Thin Film Preparation

The physical evaporation technique (PVD) is used for the formation of the heterojunction structure. InSe crystals layer were weighed (70mg) and placed in a tungsten boat (item 1 in figure 3.1) which is fixed inside the system. The glass substrates are placed on the substrate holder (item 2). The shutter (item 3) which is located between the boat and substrate is closed. The thickness of the films was measured by a crystal oscillator thickness monitor (STM-2) (item 4), the resolution of the quarts type monitor was 0.037A^{o}.The monitor can carry 300 measurements per second [57]. During evaporation process, the PVD system is closed completely. It then discharged from the air by rough and turbo molecular pumping. We wait the vacuum pressure till it reached 10^{-5} mbar, then the evaporation process begins. The current is raised till suitable temperature ~800 ^{o}C is reached, then the shutter was opened for 8 minutes where the in situ monitor read 500nm. The shutter was then closed and the system is left to cool.

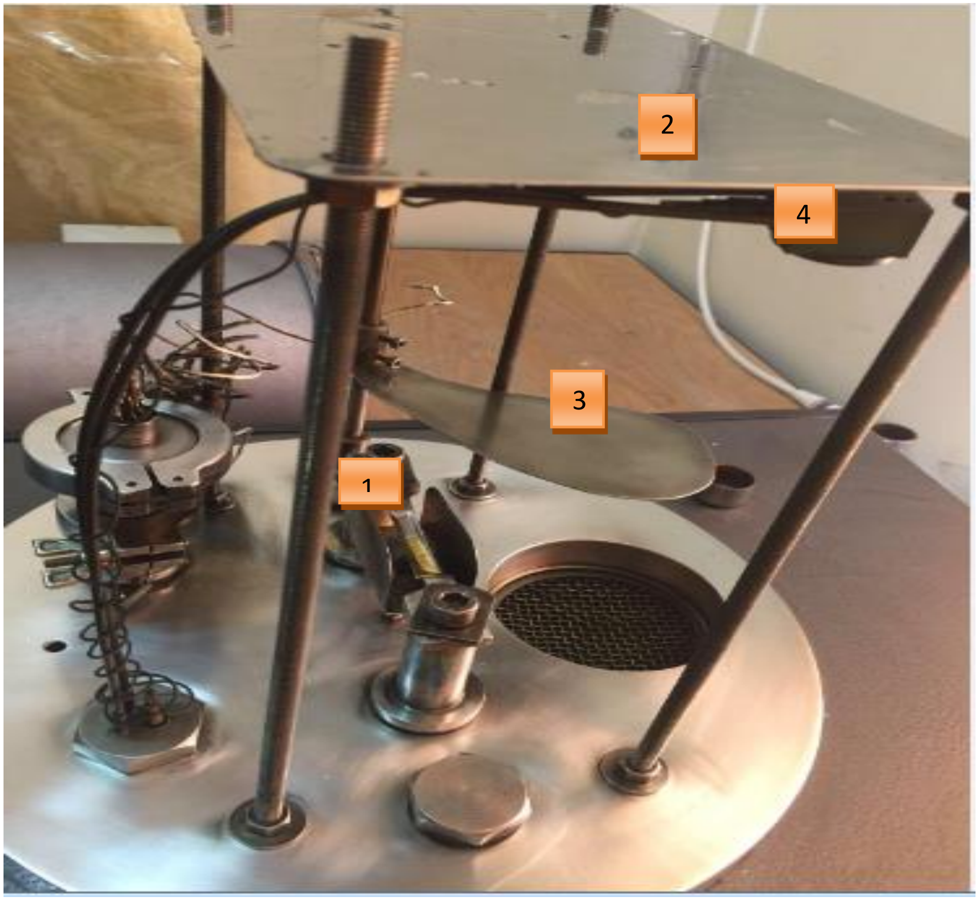

Figure 3.1: The VCM evaporation system.

After the hot substrate/annealing system was run to deposit InSe at 250 °C to obtain γ-phase of In_2Se_3, where it is done by processing the hot substrate/annealing procedure includes, connecting the system near to the power supply and ammeter, where when we increase the voltage, the current increases then the temperature will increase, we continue to do until the temperature reach to 250 °C. The temperature was monitored by *k*-type thermocouple attached to temperature reader (MASTCH-6200), the temperature was fixed at 250 °C for an hour and we take the reading of current, time, temperate and vacuum. After the deposition ends, the system was left to cool until it reach room temperature after ~2.5 hours.

Figure 3.2: The Hot substrate/Annealing system.

With the same evaporating steps, we evaporate CuO films onto glass and γ-In_2Se_3 substrates to get CuO and γ-In_2Se_3/CuO interfaces. The interfaces are demonstrated in figure 3.3((a), (b) and (c)).

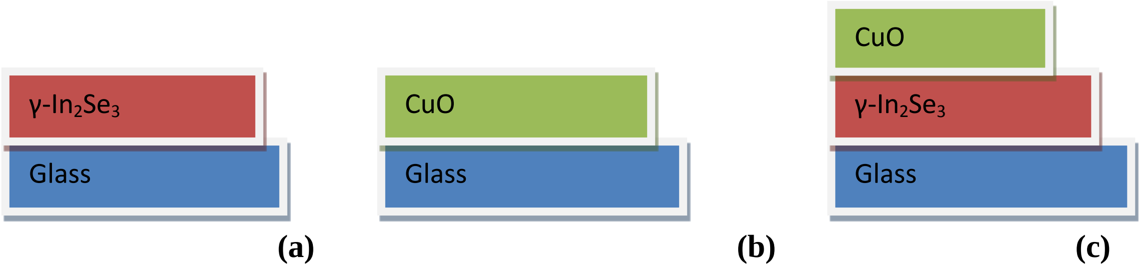

Figure 3.3: The geometrical design of (a) γ-In_2Se_3, (b) CuO and (c) γ-In_2Se_3/CuO heterojunctions.

3.3 Thin Film Analysis

The thin film analysis in this thesis is presented by means of structural analysis using x-ray, optical using spectrophotometer, impedance spectroscopy and current voltage characteristics in following subsequent sections.

3.3.1 The X-Ray Diffraction Measurements

XRD measurements were taken using a Rigaku diffractometer with copper anode K_α radiation operating at 40 kV and 15 mA to reveal 600 WX-ray power diffraction. The θ-2θ scan method was employed. The 2θ range was 10–70° and the 2θ step size was 0.05^o and the scan rate was 1^o/min. The x-ray diffraction is used to determine the lattice structure of γ-In_2Se_3, CuO and γ-In_2Se_3/CuO interfaces. The system contains a monochromator, a detector, a slit set and a sample holder. The sample rotates by 2θ and the detector is collect the intensity of the x-ray beam. Also the slits are used in order to control the size and shape of the x-ray beam. The data are analyzed by using TREOR-92 software.

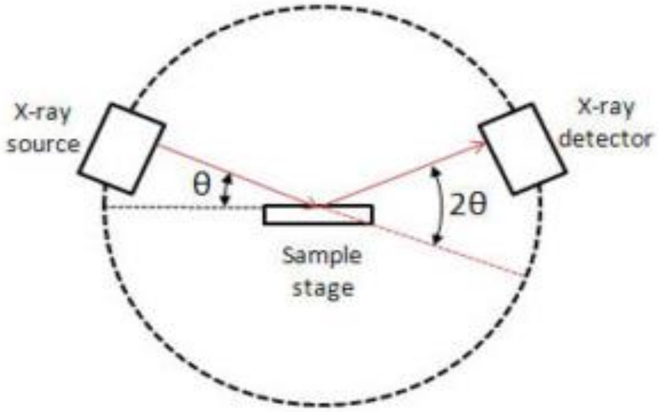

Figure 3.4: Schematic of x-ray diffraction.

3.3.2 Optical Measurements

The optical parameters presented by transmittance (T) and reflectance (R) were measured in the incident light wavelength range of 300-1100 nm with scan speed of 1200 nm/min. The measurements were carried out using a thermo-scientific evolution 300 spectrophotometer that is linked with VeeMax I I reflectometer. The system is shown in figure 3.5. This system includes wavelengths ranging from UV to near the IR region. The T% and R% are used to determine the absorption coefficient, interbands transitions, optical energy band gap and band tails. The dielectric dispersion is also determined. The data are collected using VISION Pro software package.

Figure 3.5: The UV-VIS spectrophotometer.

The UV-VIS spectrophotometer as shown in above figure contains the following parts: 1-detector cavity, 2- measuring hole, 3- light apparatus cavity, 4-normal incidence reflectometer, 5-referance blinding apparatus and 6-holder.

3.3.3 Impedance Spectroscopy Measurements

The impedance spectroscopy technique was chosen for studying the impedance (Z), resistance (R), reactance (X), parallel capacitance (C_p), series capacitance (C_s), conductance (G) and reflection confection (|r|). All measurements were done as function of frequency (10 MHz-1.8 GHz) using Agilent 4291B RF Signal Generation Impedance Analyzer. This technique is used to define the return loss and voltage standing wave ratio (VSWR). The data are collected and analyzed with the help of MATLAB software.

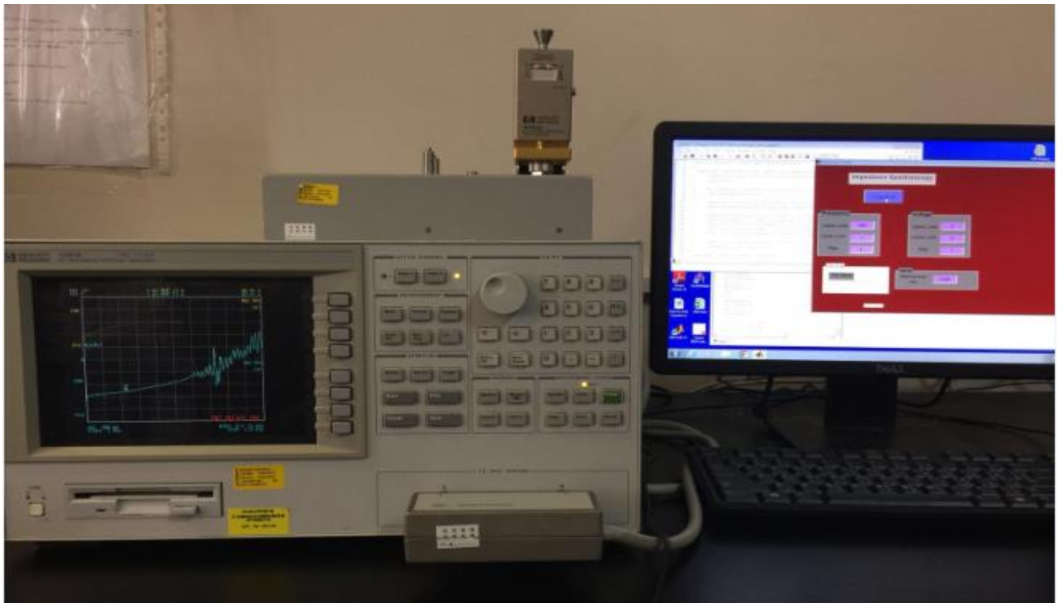

Figure 3.6: Impedance measurement including Agilent 4291B RF Signal Generation Impedance Analyzer.

In this section, we should not forget the basic principle of this system, presented by RLC circuit. The RLC circuit is an electrical circuit consisting of three basic elements resistor (R), inductor (L) and a capacitor (C) connected together in series or in parallel, the name of the circuit is derived from the letters that are used to denote the constituent components of this circuit.

When resistor, inductor and capacitor are all connected in one complete loop in series across an AC power supply, the circuit is then called series RLC circuit. In this circuit we can be impose two or more sinusoidal signals provided they have the same frequency. The current flowing through the three components remains the same and equal to the supply current or total current (I_S). The supply voltage consists of three parts: the resistor voltage (V_R), the inductor voltage (V_L) and capacitor voltage (V_C). The voltage for each branch will be different and the supply voltage is equal to the sum of three voltages [58].

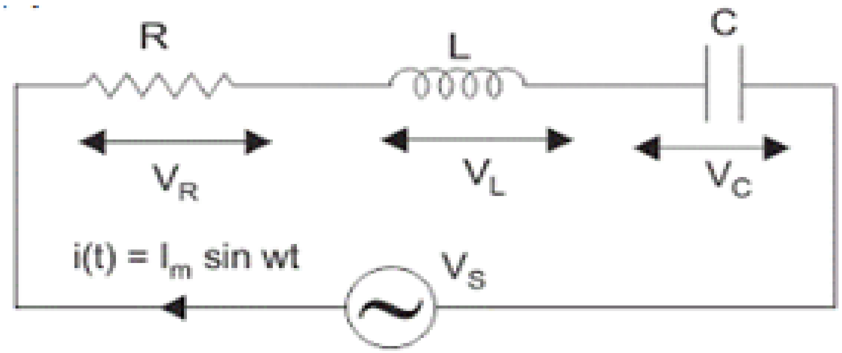

Figure 3.7: The series RLC circuit.

The source voltage is given by:

$$V_l = Iwl, \qquad V_R = IR, \qquad V_C = \frac{1}{wc} \tag{3.1}$$

By Kirchhoff's voltage law we can find the supply voltage [58]:

$$V_S = IR + L\frac{dI}{dt} + \frac{Q}{C} \tag{3.2}$$

The final supply voltage for series LRC circuit is gives by:

$$V_S = \sqrt{V_R^2 + (V_L - V_C)^2} = I\sqrt{R^2 + (X_L - X_C)^2} = I.Z \tag{3.3}$$

Where Z is the impedance of the circuit and depend on the resistance (R)and on indicative and capacitive reactance (X_L, X_C)[59]. The phase of this circuit is shown in Fig. 3.8.

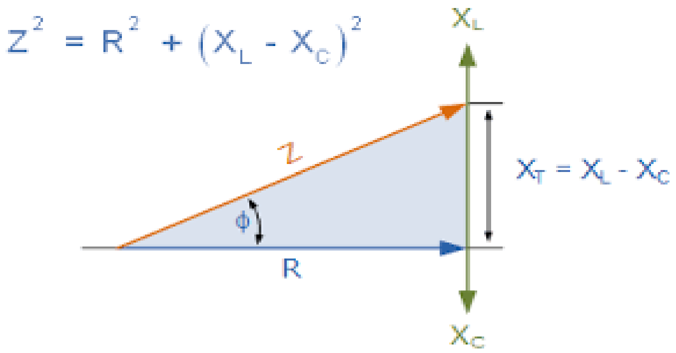

Figure 3.8: The impedance triangle of series RLC circuit.

In the parallel RLC circuit (Fig. 3.9), we know that the supply voltage (V_S) is common to all three components. The supply current (I_S) consists of three parts: the current flowing through the resistor (I_R), the current flowing through the inductor (I_L) and the current through the capacitor (I_C). The total current (I_S)is the vector sum of the three currents.

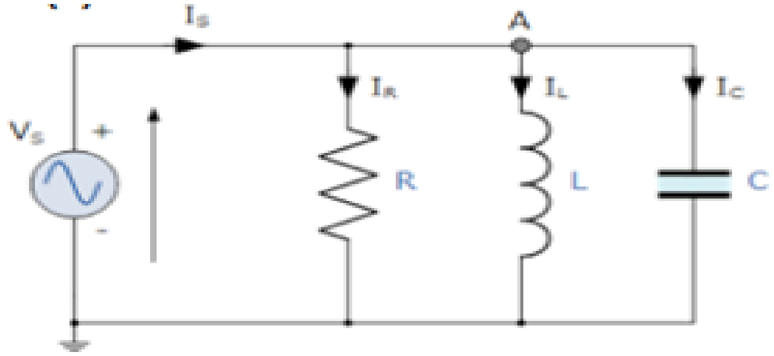

Figure 3.9: The parallel RLC circuit.

By using Kirchhoff's Current law, we can find the current through each branch [58]. Particularly,

$$I_S = \frac{1}{RC}\frac{dV}{dt} + \frac{V}{CL} + C\frac{d^2V}{dt^2} \tag{3.4}$$

From current triangle we get:

$$I_S = \sqrt{I_R^2 + (I_L - I_C)^2} = \sqrt{\left(\frac{V}{R}\right)^2 + \left(\frac{V}{X_L} - \frac{V}{X_C}\right)^2} = \frac{V}{Z} \tag{3.5}$$

Where $I_R = \frac{V}{R}, I_L = \frac{V}{X_L},\ I_C = \frac{V}{X_C}$

From R, $X_L \ and \ X_C$ we can find the relation of the current impedance Z which is given as:

$$Z = \frac{1}{\sqrt{\left(\frac{1}{R}\right)^2 + \left(\frac{1}{X_L} - \frac{1}{X_C}\right)^2}} \tag{3.6}$$

When we look at the final relation of Z in series and parallel RLC circuit, we find that the indicative reactance(X_L) and capacitive reactance $(X_c)$are shown in it. When

X_L and $X_c$equal zero the impedance equal the resistance (Z=R), and at this condition the frequency is called resonant frequency.

3.3.4Hot Probe Technique

The hot probe is a method used to determine the conductivity type of materials. Whether a semiconductor sample is n (majority carriers are electrons) type or p (majority carriers are holes) type is determined by this method. For measurements, the sample is attached to a voltmeter or an ammeter and a heat source. The heat source will cause charge carrier motion. The heat given from the positive probe creates an increased number of higher energy carriers which then diffuse away from the contact point. This will cause a current/voltage difference, where if the voltmeter reading connected to the semiconductor is positive, the semiconductor sample will be (n-type). This means that the number of electrons in the material is predominant. When the voltmeter reading is negative, the semiconductor sample is (p-type).When we did this test on our samples we found: the CuO sample is p-type, InSe is n-type, InSe/CuO is p-type, γ-In_2Se_3 is n-type and γ-In_2Se_3/CuO is p-type.

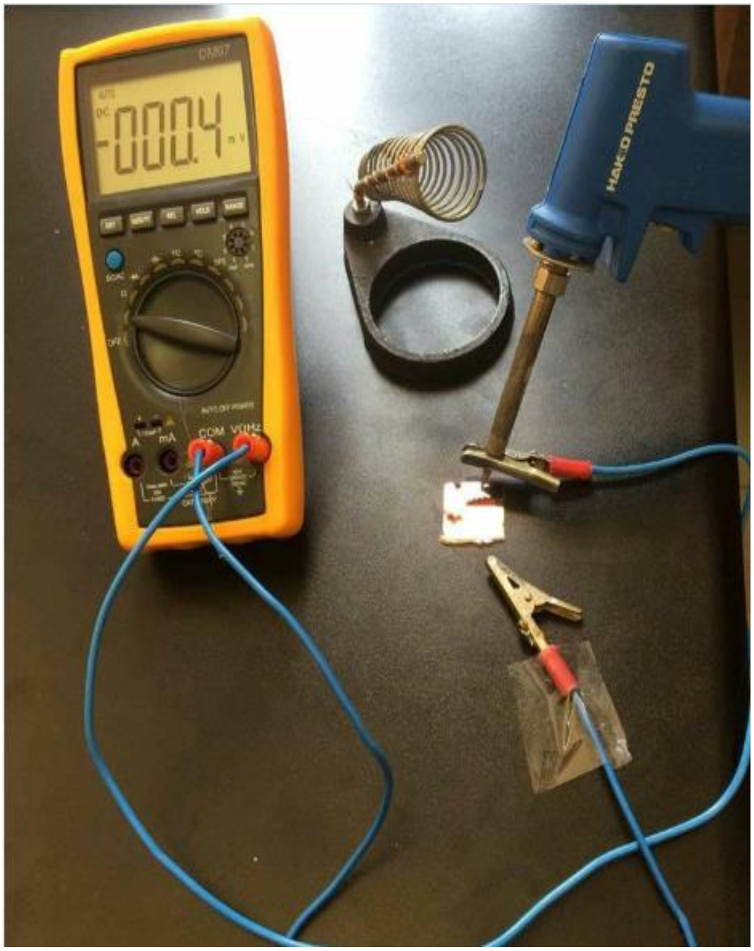

Figure 3.10: The hot probe device.

3.3.5 Current–Voltage Characteristic Measurements

Keithley 6485 picoammeter and Keithley 235 voltage source are used to determine the current-voltage (I-V) characteristics. The 6485 picoammeter device can measure very low currents (100 fA). The current-voltage (I-V) characteristics technique allows knowing the nature of metal-semiconductor contact or film is fit to be electronic device and what are the appropriate applied voltages.

In our experiments, the range that was used for the voltage is from -1.0 to 1.0volts in steps of 0.01volt.

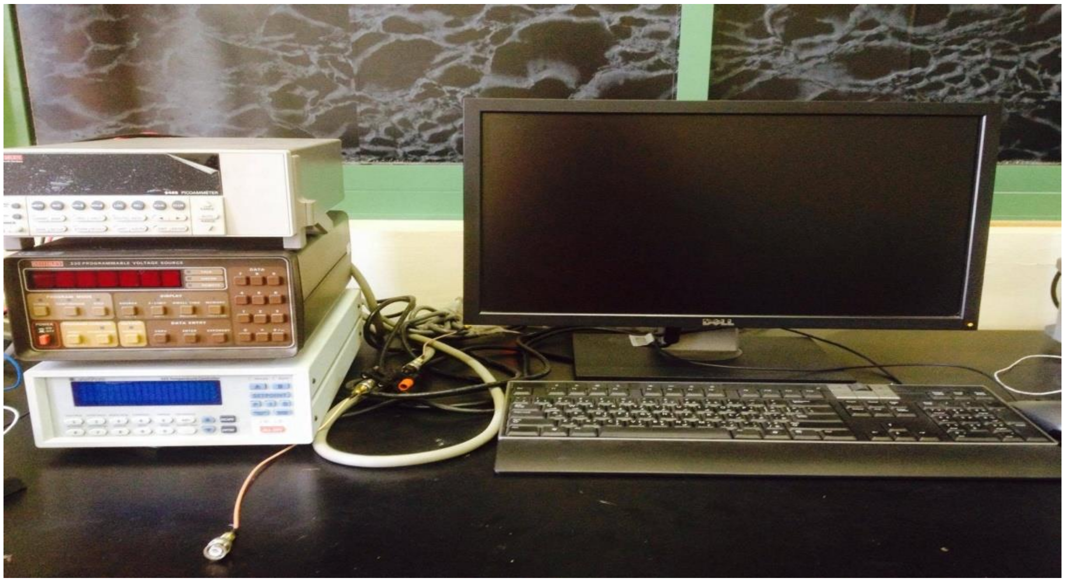

Figure 3.11: Current-voltage (I-V) measurement including Keithley 6485 Picoammeter and Keithley 230 Voltage Source.

Chapter Four

Results and Discussion

In this chapter we discuss the formation nature as well as the optoelectronic properties of the InSe/CuO interfaces. The analysis of the structural, optical and electrical properties of this heterojunction will provide information about the applicability of the InSe/CuO in technology.

4.1 Structural Analysis

We first recall that the current work include the growth of InSe and CuO onto glass substrates and the growth of CuO onto InSe and γ-In_2Se_3. The latter is obtained by either annealing the InSe as grown films at 250 ^oC for one hour under vacuum media of pressure 10^{-5} mbar or by raising the substrate temperature to 250 ^oC. The novelty of γ-In_2Se_3 appears in its moderate energy band gap value and well crystallinity.

The X-ray diffraction patterns for as grown and annealed glass/InSe, glass/CuO and InSe/CuO thin films are presented in figure 4.1. The X-ray diffraction show no sharp patterns for glass/InSe and glass/CuO meaning the amorphous nature of growth. On the other hand, γ-In_2Se_3 display sharp diffraction patterns which should refer to a polycrystalline nature. The X-ray diffraction ofγ-In_2Se_3 has three peaks; the first one at appeared at $2\theta = 19.65^o$with intensity of 7344 (a.u.), the second peak appeared at $2\theta = 25.6^o$ with intensity of 30695 (a.u.) and the third peak appeared at $2\theta = 28.3^o$ with intensity of 184225 (a.u.).These peaks are found to correspond to a hexagonal unit cell ofγ-In_2Se_3 where lattice constant with help of equation (2.2 (b)) are observed to exhibit values of a= 4.015 A^o and c= 18.90 A^o. The Miller indices (hkl) for the first, second and third peaks are (112), (100), (006), respectively. In comparison with similar works, the lattice parameters of the hexagonal phase are reported to be a = 4.00 A^o and c = 19.38 A^o, and the main reflection appeared in the (006) direction [48]. The lattice constants values and plane orientation are consistent.

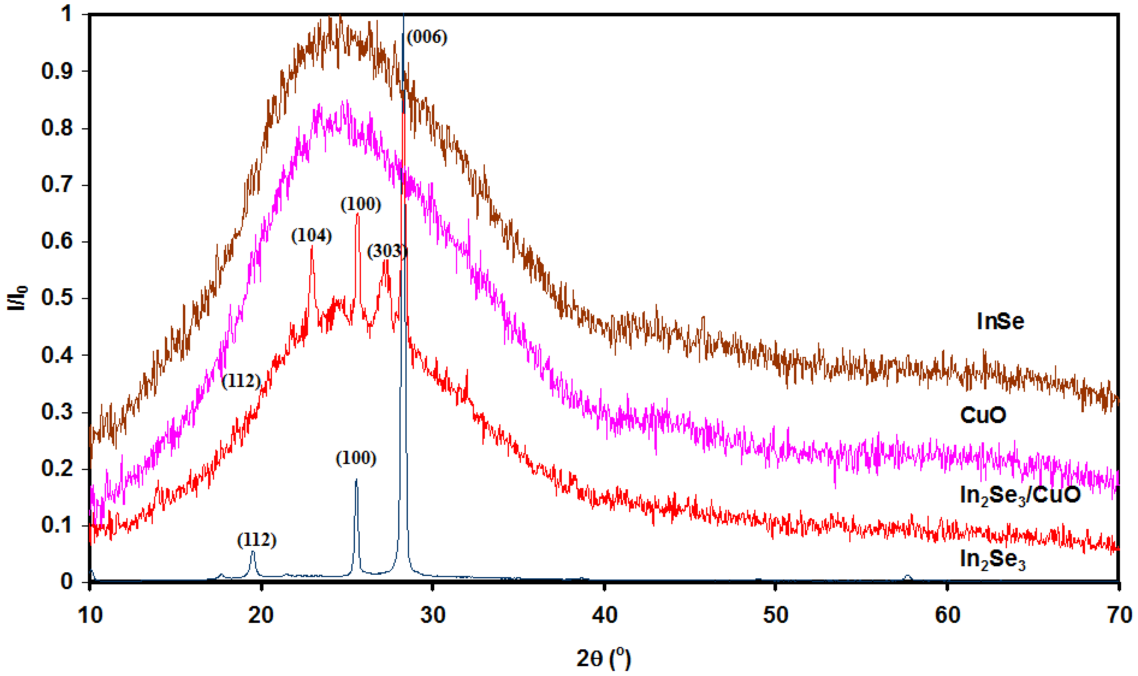

Fig. 4.1: The x-ray diffraction patterns for CuO, InSe, γ-In_2Se_3 and γ-In_2Se_3/CuO.

The reason beyond the conversion of structure from amorphous to polycrystalline is assigned to the crystallization and recovery processes in amorphous materials which indicate that small grains are randomly distribution revealing the high defective structure. Defective materials are thermodynamically unstable upon annealing, atoms gain extra thermal energy that allow it to move and reduce the number of available defects. Such mechanism strongly affects the grains [60].

Generally, only a partial recovery is possible because the dislocation structures is not completely removed, but reaches a metastable state that is called a recrystallization. During recrystallization, larger grains grow and consume the old grain, resulting in a new grain structure with a less dislocation density[60]. γ-In_2Se_3 phase is preferred at 250 ^oC because it is believed that at this temperature every In atom is surrounded by three Se atoms and every Se atom is surrounded by three In atoms. Thus, the formation of γ-In_2Se_3 indicates that only two of the Se atoms are able to get rid of one of their *p* electrons and become three-valent, In this case, the third selenium atom is able to bind only two In atoms in an angular configuration[61].

Naturally, CuO is amorphous if prepared by physical vapor deposition techniques. The morphology of CuO is due to the high oxygen vacancy, since the oxygen vacancy is large compared to Cu, firing technique is usually preferred, this technique is not available in our laboratory [62]. The oxygen atoms have large number of vacancy and do not locate in its right place. Therefore it cannot balance with Cu leading random arrangement of atoms, which make the CuO amorphous [63]. .

The X-ray diffraction pattern for the γ-In_2Se_3/CuO are replaced on the same normalized scale with that of γ-In_2Se_3 in figure 4.2. As seen from the figure, and table 4.1

Table 4.1: The structural parameters of γ-In_2Se_3 and γ-In_2Se_3/CuO interfaces.

Spectrum	**γ-In_2Se_3**	**γ-In_2Se_3/CuO**
2θ (^{o})	28.3	28.3
Intensity (a.u.)	184225	002751
d (nm)	0.315	0.315
β (x10^{-3}rad)	3.48	5.23
D (nm)	42.78	28.52
εx10^{-3}	3.46	5.19
SF x10^{-3}	1.32	1.99
(hkl)	(006)	(006)
a (Å)	4.015	4.007
c (Å)	18.90	18.90
δx10^{11} (line/cm^2)	3.022	6.812

The maximum peaks, which are observed for glass/γ-In_2Se_3 resides at 28.3^{o}and exhibit intensity value of 184225 (a.u.). Comparing with γ-In_2Se_3/CuO we find the two maximum peaks resides at the same angle but the intensity of γ-In_2Se_3/CuO decreased to 2751 (a.u.). A complete evaluation of the observed diffraction patterns is shown in table 4.1. Equations ((2.4), (2.13), (2.14), (2.15) and (2.16))were used to calculate d, D, ε ,SF and δrespectively. As seen from the table, while the lattice constant along the a-axis and grain size decreased, the dislocation density, strain and stacking faults increased upon interfacing of γ-$In_2Se_3$with CuO. This behavior is explained by taking into account the possible ,

possible reasons like deformation, ionic radius, bonding mechanism, lattice mismatch and critical thickness effect. Particularly, the ionic radius of In is 0.940A^o [64], for Se is 1.84A^o [65], for Cu is 0.73A^o [66], and for O is 1.38A^o [67]. The data suggest that Cu can replace vacant sites In and O can replace Se leading to the observed decrease in the lattice constant. However, because oxygen atoms in CuO contain many vacancies This may also lead to the formation interstitial defect in the arrangement of atoms within the molecule which explains the increase in $\epsilon, \delta$and SF values [68,69].

As also seen from figure 4.2 the maximum peak of γ-In_2Se_3 become broaden, fell down and widened after adding CuO. The intensity of the maximum peak of γ-In_2Se_3/CuO decreased upon CuO interfacing meaning that there is a non-uniform deformation at the interface. The non-uniform deformation arises from stress that is associated with the strain values listed in table 4.1[70, 71].

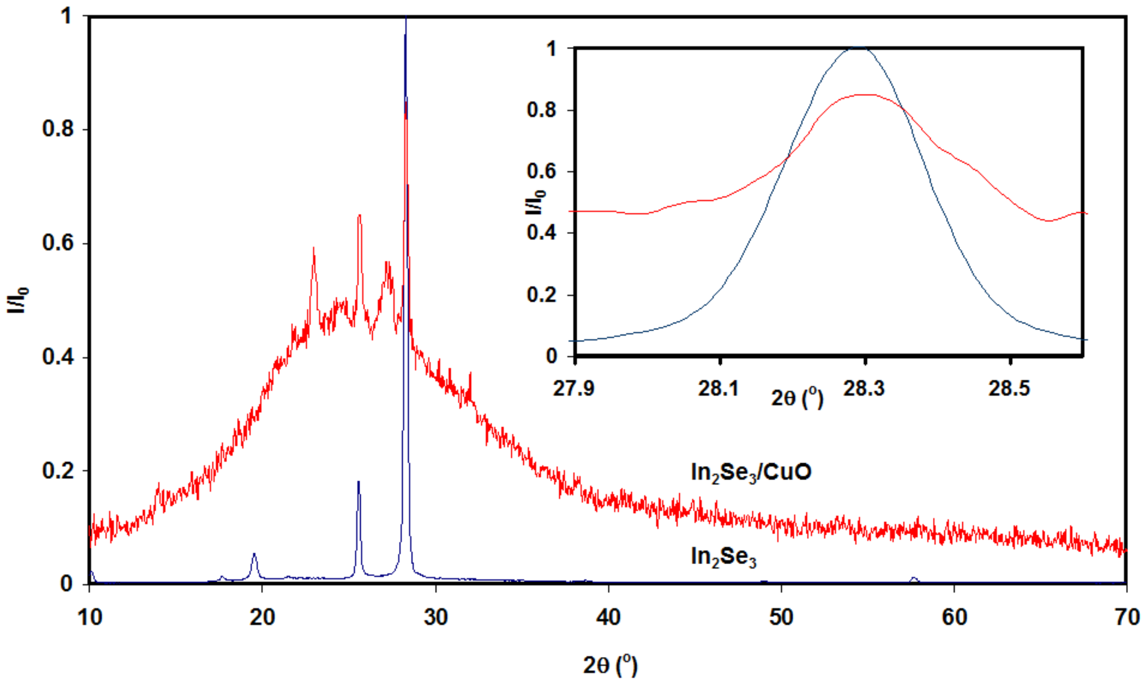

Figure 4.2: The maximum peaks of γ-In_2Se_3 and γ-In_2Se_3/CuO.

If the bonding mechanism is taken into consideration, the bond lengths of In-In, Se-Se, Cu-Cu, In-Se, Cu-Se, Cu–O, In-O are 2.82A^o [72], 2.37A^o [73], 3.64A^o [74], 2.68A^o [75], 2.46A^o [76], 1.85A^o [77], 2.16A^o [78], respectively. When comparing bond length for In-Se and In-O we find that the bond length for In-Se is greater than the bond length for In-O. Thus, unbonded In atoms would prefer to bond with O as a result of strong interaction. Also when comparing bond length for Cu-Cu and Cu-Se we find that the bond length for Cu-Cu is greater than the bond length for Cu-Se so Cu would prefer to interact with unbonded Se atoms. Because the bond length of In-Se is small so the force in this molecule is high ($F \propto \frac{1}{r^2}$)leading to high orientation and high dipole interaction [79]. The presence of these newly established interaction forces at the indium selenide-copper oxide interfaces explains the changes on the mechanical parameters.

The theoretical lattice mismatches between polycrystalline InSe and polycrystalline CuO are calculated using lattice parameters and epitaxial relationship [28].

$$\Delta = \left|\frac{a_e - a_s}{a_e}\right| \times 100\% \qquad (4.1)$$

Where, a_s is the lattice constant of the substrate In_2Se_3 equal 4.0 A^o[80] and a_e is the lattice constant of the epitaxial layer CuO equal 4.26 A^o [81]. The lattice mismatches of γ-In_2Se_3/CuO is 6.10% .

The critical thickness (t_c) between In_2Se_3 and CuO is calculated using lattice parameters with the help of equation [28]:

$$t_c = \frac{a_e}{2\Delta} \tag{4.2}$$

The critical thickness of γ-In_2Se_3-CuO is 34.9 A^o. Based on these values, the interface formation is sufficiently good to actualize quantum confinement and to form depletion width.

4.2 Optical Analysis

The spectral data of transmittance (T) for the γ-In_2Se_3 (500 nm), CuO (500 nm) and γ-In_2Se_3/CuO (1000 nm) being recorded in the wavelength (λ) range of (300-1100) nm appears in figure 4.3. As it is shown in the figure, the transmittance of γ-In_2Se_3 slightly increased with increasing incident light wavelengths until a highest transition value of 63.6% at 650 nm is reached. After this value of wavelength, the transmittance decreased reaching value of 53% at 834 nm where it then tends to remain constant. The transmittance spectra for CuO is increasing with increasing λ. It reaches a value of 27.1% at 560 nm. Above 560 nm, the transmittance slightly decreased and then remain constant. On the other hand, the T% of γ-In_2Se_3/CuO initially grows until a value of 15% at 576 nm is revealed. In the range of 576-644 nm, the T% remain constant. Above 644 nm, the T% decreased in small range and then immediately increased for all λ values greater than 792 nm. In general, the T% for γ-In_2Se_3, CuO and γ-In_2Se_3/CuO have the same behavior approximately for all λ< 600 nm. But for λ>600 nm, the T% exhibit different behavior. In addition, the T% values for γ-In_2Se_3 is higher than that of CuO and CuO is higher than that of γ-In_2Se_3/CuO, such behavior is ascribed to the thickness of the heterojunction as well as the crystalline nature and the energy band gaps of the materials [82].

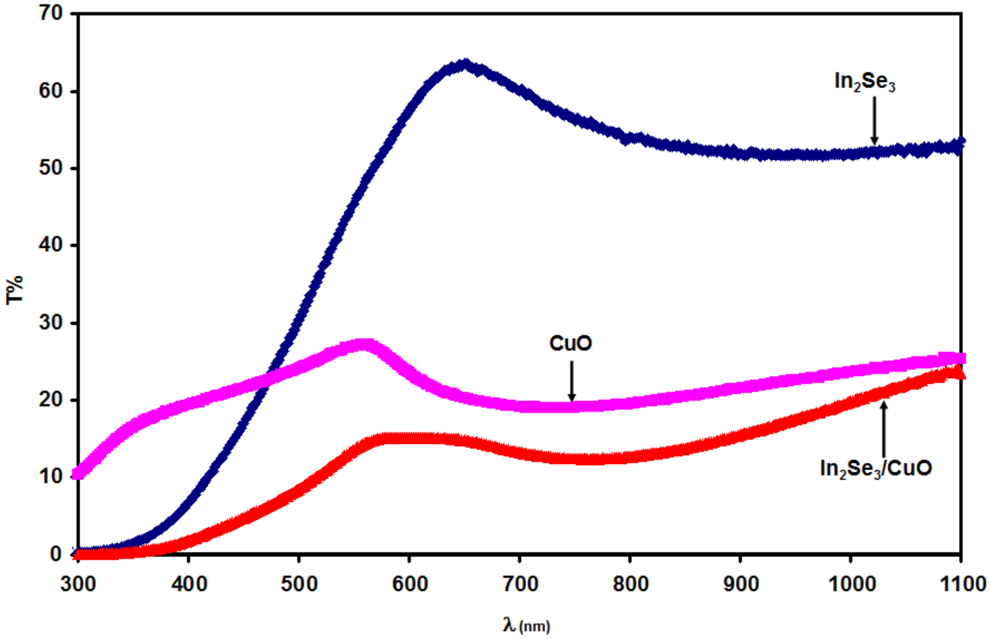

Figure 4.3: The transmittance spectra for γ-In_2Se_3, CuO and γ-In_2Se_3/CuO interfaces, respectively in the range of 300-1100 nm.

On the other hand, the reflectance (R) spectra for γ-In_2Se_3 which is illustrated in Fig. 4.4,slowly increases with increasing light wavelength until a value of 13% is reached at 434 nm. for larger λ value, R% decreased with increasing λ reaching a minima at 584 nm. Further increase in λ value increases R%. when λ exceeds900 nm, R% tended to remain constant. The spectra of γ-In_2Se_3/CuO heterojunction displayed two maximum at 392 nm and 632 nm and one minima at 510 nm, for λ greater than 900 nm, R% values tended to remain constant again. However, CuO exhibit an increasing R% in the range of (300-700) nm. For CuO andγ-In_2Se_3/CuO, at λ>>700 nm, R% decrease with increasing λ values.

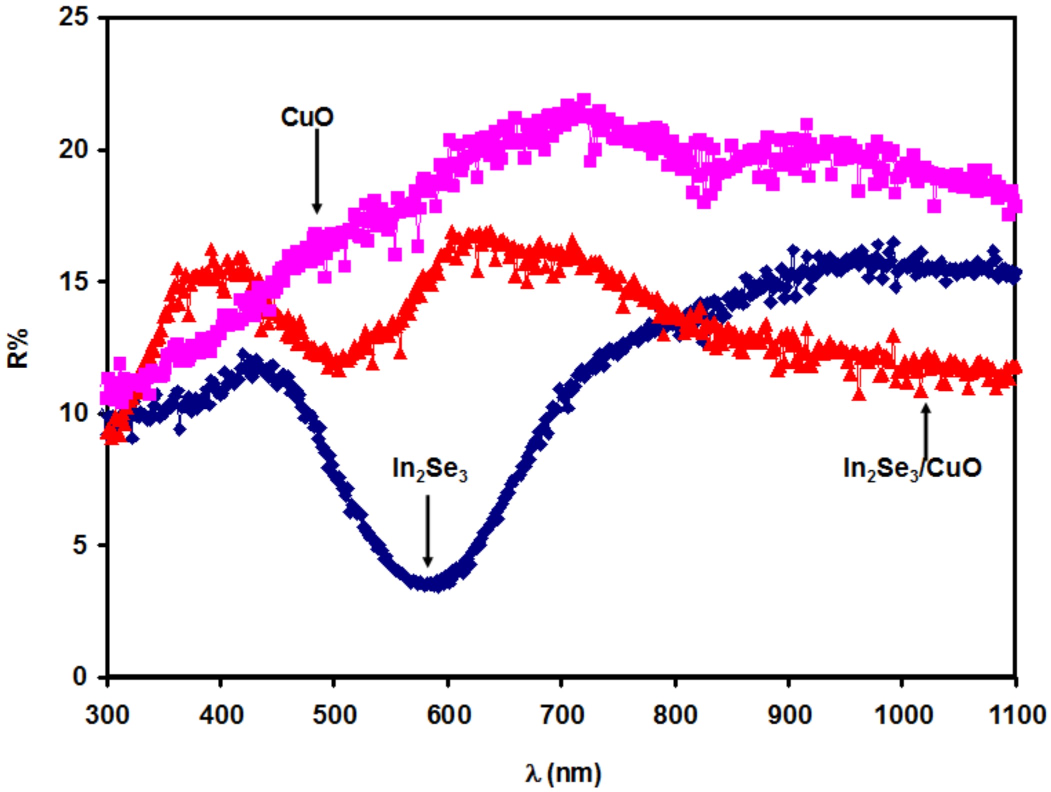

Figure 4.4: The reflectance spectra of γ-In_2Se_3, CuO and γ-In_2Se_3/CuO interfaces, respectively in the range of 300-1100 nm.

The optical absorbance (A) which is calculated from the measured from R and T spectra by the equation [83]:

$$A\% = 100\% - T\% - R\%, \tag{4.3}$$

is shown in figure 4.5. The figure display a full picture for the light dynamics on the films surfaces. The A% of γ-In_2Se_3 remain constant in the incident photon energy range of (1.0-2.0) eV. The A% increases with increasing energy for values of E above 2.0 eV. The A% of CuO is lower than that of γ-In_2Se_3 and follow the same behavior in the range of (1.0-2.1) eV. The A% constant slightly increases above 2.2 eV. For γ-In_2Se_3/CuO has the highest value of absorbance. It increases in the range of (1.0-1.5) eV, then it remains constant in the range of (1.5-2.3) eV. For all energy values larger than 2.3 eV, A% sharply increases. Possible reasons for the enhanced absorption for the γ-In_2Se_3/CuO heterojunction are the lattice mismatch between the two layers, the inability of electron-hole recombination at the interface due to the crystalline nature, defects and sample inhomogenuities as we observed through structural analysis [82].

Looking at the E-axis, we find that the absorbance nearly reaches zero in low energy region. This indicates the presence of band tails which causes band transition. The interband processes lead to transition of holes and electrons from level to level though the energy band gap [82].

Reasons for these bands could be the electric field that result from free moving charges (externally charge) and bound charges (internally charge), the scattering of electrons at interface and the electron-phonon interaction [82].

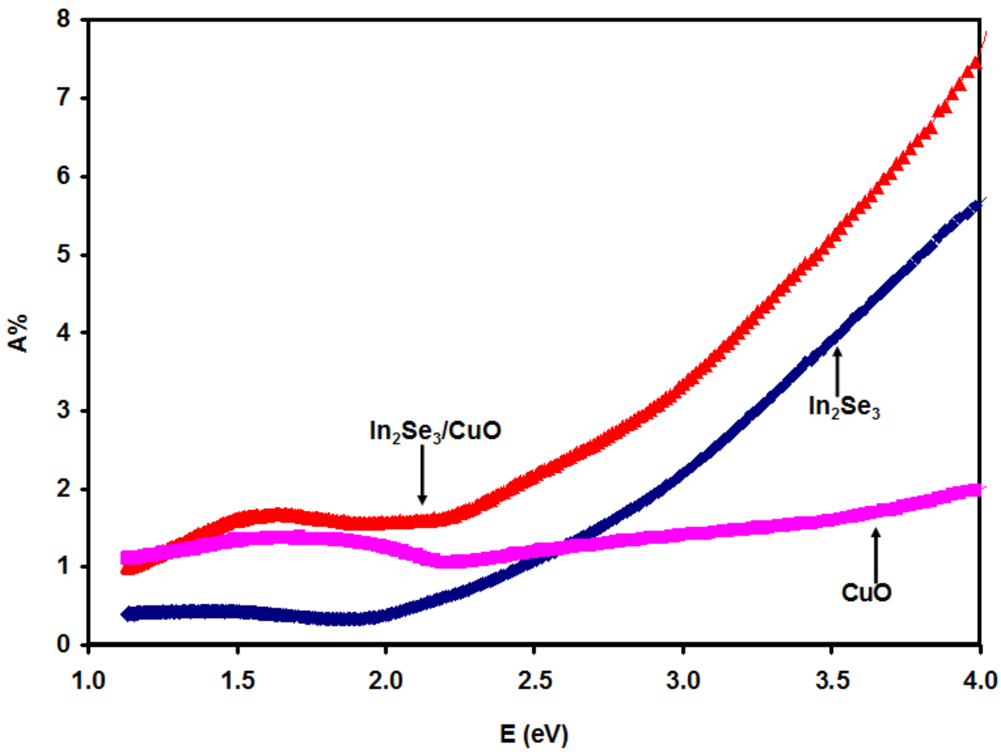

Figure 4.5: The optical absorbance verses photon energy range of 1-4 eV for the γ-In_2Se_3, CuO and γ-In_2Se_3/CuO films.

It is worth noting that in this part of the chapter , while the measured transmittance (T%) and reflectance (R%) spectra will be presented as functions of incident light wavelength (λ), the absorption coefficient spectra will be presented as function of incident photon energy (E). The reason for this way of presentation is the fact that both of T% and R% are determined geometrically by measuring the transmitted or reflected intensity of light which results from light spectrum of wavelengths passing through a grating slit system (exhibiting space divisions in nanometers). The calculation method of the absorption coefficient is reached through geometrical extraction of the transmitted and reflected light intensities. On the other hand, because the analysis of the calculated absorption coefficient spectra depend on the quantum mechanical derivation of the energy bands, which get use from the incident photon energy, the absorption coefficient spectra will be presented as function of energy.

As complementary information, the absorption coefficients (α) was determined from the relation [84]:

$$\alpha = \frac{2.3026A}{d} \tag{4.4}$$

Where d is thickness. Absorption coefficient (α) represent foundation to design optoelectronic devices. The relation between the absorption coefficient (α) and the incident photon energy (E) is represented in figure 4.6. It is clearly observed that the absorption coefficient values are very similar to that of previously described absorbance.

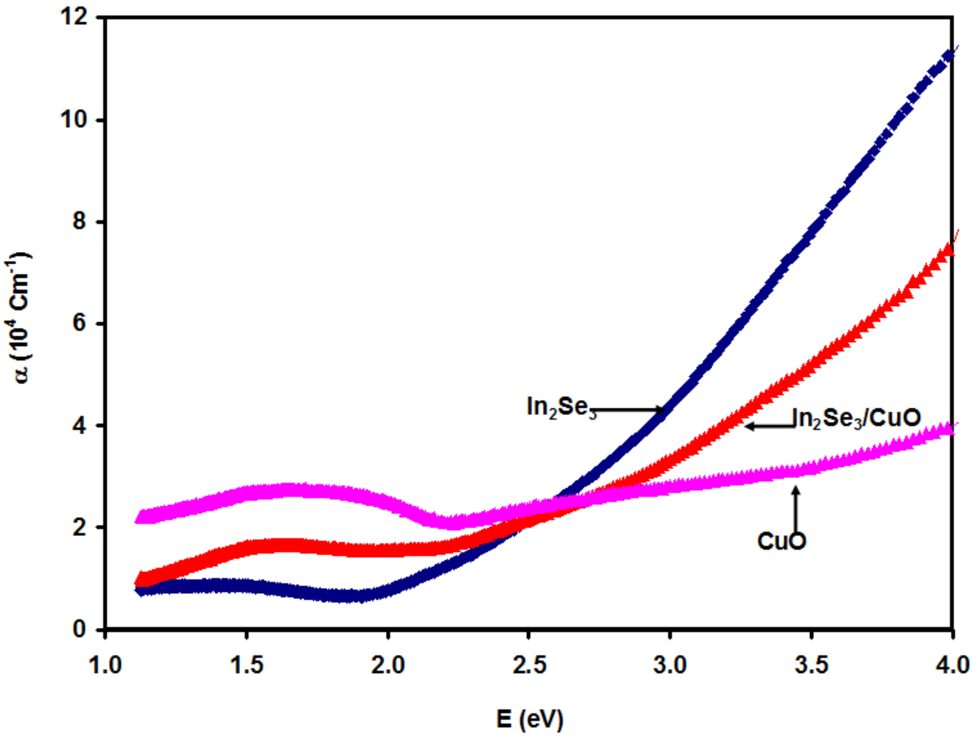

Figure 4.6: The absorption coefficient (α) as a function of photon energy in the range of 1.0- 4.0 eV.

The calculated absorption coefficient (α) is used to get information about the changes in the energy band gap of the studied materials. To find the energy band gap, the Tauc's relation is employed [44, 85]. It take the form:

$$(\alpha E)^{1/p} \propto \left(E - E_g\right) \qquad (4.5)$$

Where E is the photon energy and p takes values of 1/2, 2, 3 or 3/2. Touc's plots $(\alpha\ E)^{1/P}$ with E to get the E_g from the intercept of the E-axis in the linear region of $(\alpha E)^{1/p} - E$ variation. To apply this relation we plot $(\alpha E)^2$, $(\alpha E)^{1/2}$, $(\alpha E)^3$ and $(\alpha E)^{2/3}$ versus E as shown in figure 4.7. To find the energy band gap, we choose the power or the value of p that gives most linear fit which pass through widest range of data, and when we look to figure 4.7 we find that the most linearity at p equal 2.The values of energy band gap (E_g) which are calculated with the help of Fig. 4.8, are displayed in table 4.2.

In one of the published works, the value of E_g for γ-In_2Se_3 is reported to be 1.55 eV [86], in another work, the value of E_g was 1.92 eV [87]. Literature data also reported a value of 2.1 eV [88] for γ-In_2Se_3.The latter one coincides with the value we determined as 2.1 eV in this work. This difference in energy band gap values form one work to another maybe due to defects, and degree of crystallization.. In addition; the incomplete bonds at the interfaces of the heterojunction leads to change in energy band gap [89].

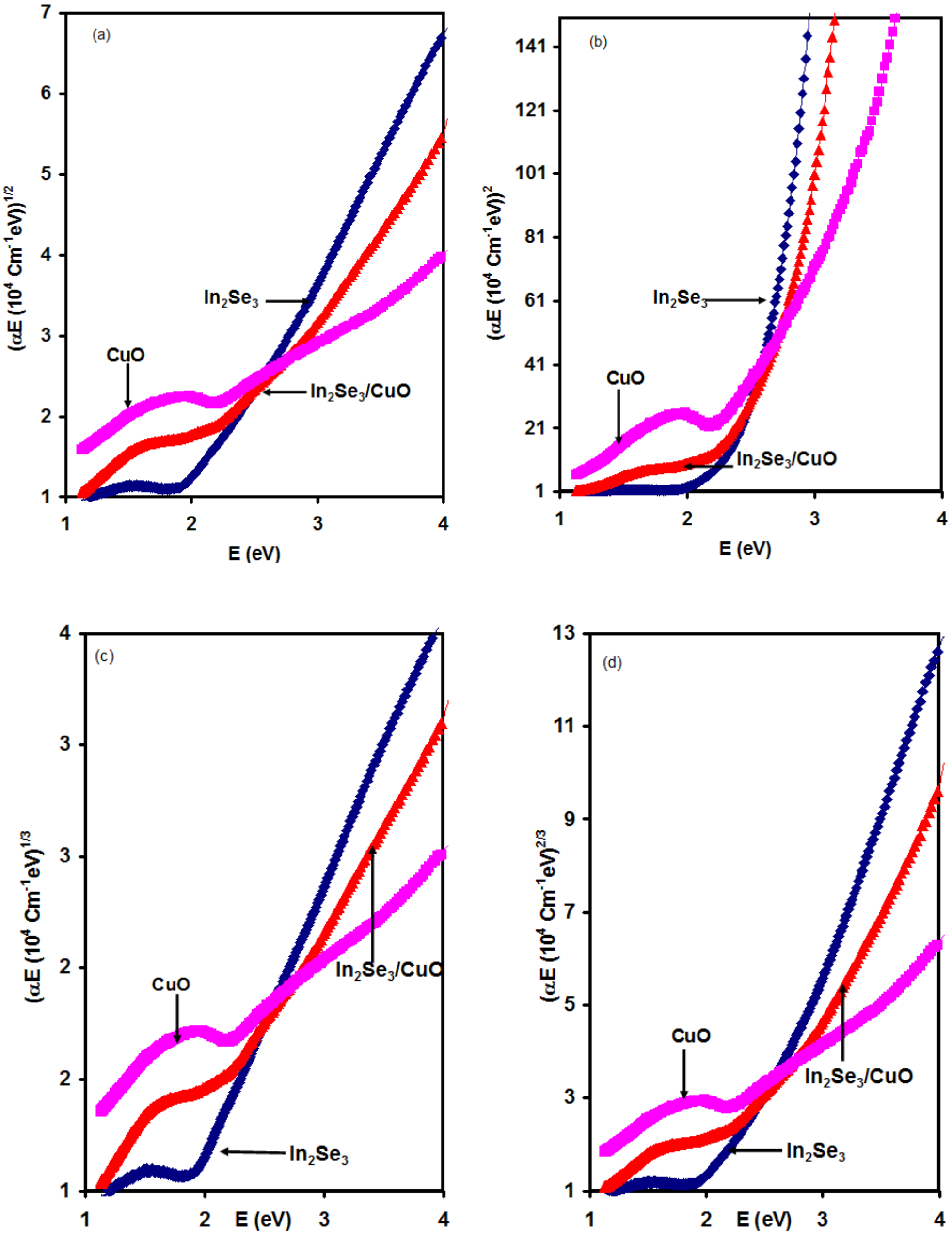

Figure 4.7: The $(\alpha\ E)^{1/P}$- E variation for the γ-In_2Se_3, CuO and γ-In_2Se_3/CuO films, for (a) p=1/2, (b) p=2, (c) p=3 and (d) p=2/3.

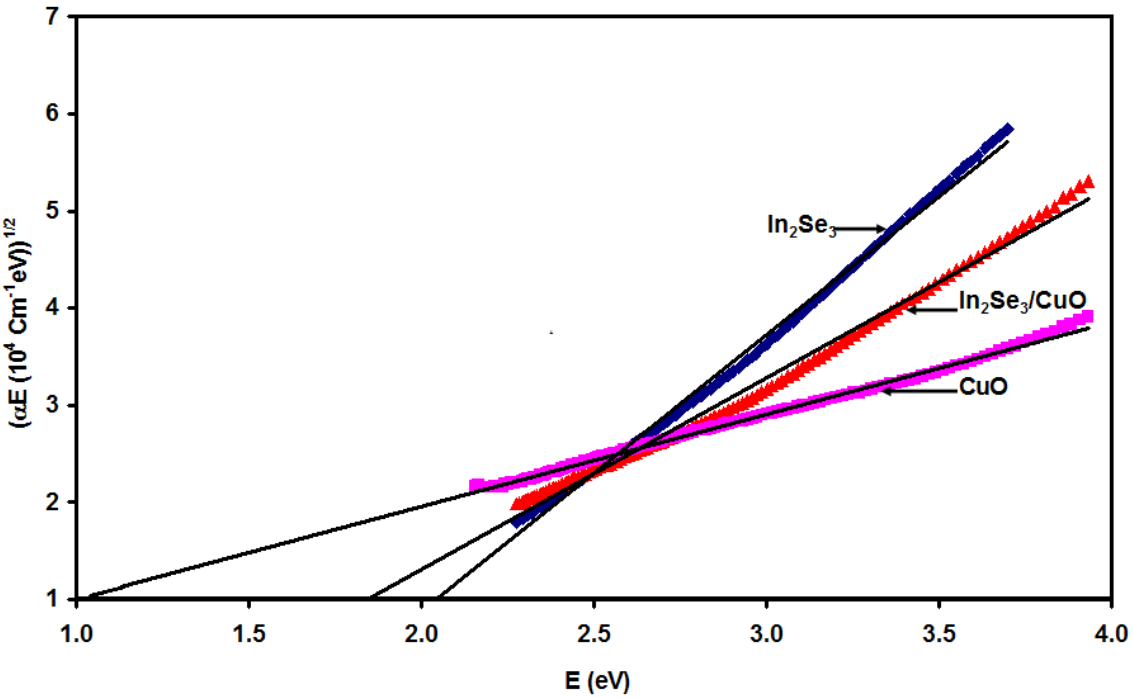

Figure 4.8: The values of energy band gap for γ-In_2Se_3, CuO and γ-In_2Se_3/CuO films.

In an attempt to observe the presence of energy band tails or interband transition in the γ-In_2Se_3, CuO and γ-In_2Se_3 /CuO we have used the equation:

$$\alpha = \alpha_0 \exp\left(\frac{E}{E_e}\right) \tag{4.6}$$

Where plotting ln (α) versus E, we find that the intercept is ln (α_0) and the slope is $1/E_e$ from equation (4.6).

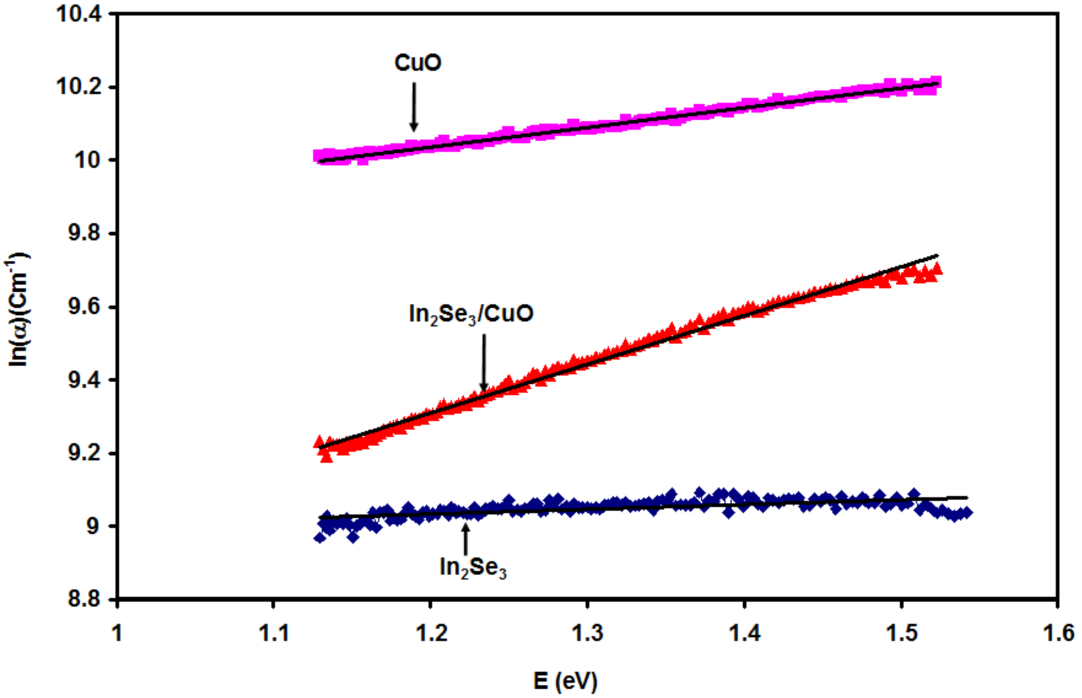

Figure 4.9: The values of energy band tail for γ-In_2Se_3, CuO and γ-In_2Se_3/CuO films.

It is clear from the calculated values of energy band tails which are shown in Table 4.2 that E_e is larger than the band gap of γ-In_2Se_3 and band gap of CuO. This indicates that there is no band tails in these two materials and the observed decay in α value in the incident photon energy range (1.1-1.6) eV, may be due to the presence of second energy band gap in the materials. However, the interface exhibit E_e values less than E_g indicating that there may exist some band tails in interface boundaries. The presence of band tails at the interface or in the depletion region of the heterojunction could have resulted from the bond formation Cu-Se and In-O at the junction surface.

Table 4.2: Energy band gap and energy band tail values for the heterojunctions.

Sample	**E_g (eV)**	**Ee (eV)**
γ-In_2Se_3	2.1	7.68*
CuO	1.1	1.80*
γ-In_2Se_3/CuO	1.8	0.75

*Cannot be assigned as band tail. Probably they represent secondary band gap

The optical picture becomes clearer for the γ-In_2Se_3/CuO through the calculation of energy band offsets. . The conduction (E_c) and valance (E_v) bands offsets of this structure are [90]:

$$\Delta E_c = q\chi_{InSe} - q\chi_{CuO} \tag{4.7}$$

$$\Delta E_g = |E_{g(InSe)} - E_{g(CuO)}| \tag{4.8}$$

$$\Delta E_v = |\Delta E_c - \Delta E_g| \tag{4.9}$$

Where $q\chi$ is the electron affinity. It exhibit values of is 4.07 eV [91] and 4.60 eV [92], for CuO and InSe, respectively. The energy band gap value for CuO is 1.35 eV [91] and for InSe is 1.45 eV [93]. From these data, the$\Delta E_c$is equal 0.53 eV, $\Delta E_g$is 0.1 eV and ΔE_v is 0.43 eV.The band offset leads to quantum confinement. The quantum confinement affects the electron-hole recombination rates [94] as well as emission mechanisms [95]. The difference between the theoretical and the experimental data of the valance band offsets can be assigned to the low crystal symmetry, large lattice mismatch, different particle size and different strain values [96].

To expand the possible application of this structure dielectric properties are investigated. To determine the effective dielectric constant ($\varepsilon_{\mathrm{eff}}$) we used the equation [97]:

$$R = \frac{\left(\sqrt{\varepsilon_{eff}} - 1\right)^2 + k^2}{\left(\sqrt{\varepsilon_{eff}} + 1\right)^2 + k^2} \tag{4.10}$$

$\varepsilon_{\mathrm{eff}}$ has an equation in two terms the first term is the real part (ε_{r}) and the second term is imaginary part ($\varepsilon_{\mathrm{im}}$)[98,99]:

$$\varepsilon_r = \varepsilon_{eff} - k^2 \tag{4.11}$$

$$\varepsilon_{im} = 2\sqrt{\varepsilon_{eff}}k \tag{4.12}$$

The components of the effective dielectric constant are

$$\varepsilon_{eff} = \varepsilon_r + i\varepsilon_{im} \tag{4.13}$$

Where both terms are given in terms of extinction coefficient (*k*), with:

$$k = \frac{\alpha\lambda}{4\pi} \tag{4.14}$$

The spectra of real and imaginary parts of the dielectric constant are shown in figure 4.10 and figure 4.11, respectively. From figure 4.10, in the frequency domain of (270-500) THz the real part of the dielectric constant for γ-In_2Se_3 slightly decreases with increasing incident light frequency F. In the higher frequency domain, ε_r increases with increasing F till a value of 4 is reached at 669 THz. After this frequency the ε_r remain constant with the minimum value of 3.5. Similarly, for the CuO, ε_{r} increases with increasing F reaching a value 7.5 at 416 THz. For higher frequency values,ε_{r} decreases till 850THz is arrived where it then remain constant. When we look to γ-In_2Se_3/CuO curve we find it exhibit mediatevalues between those of γ-In_2Se_3 and CuO.

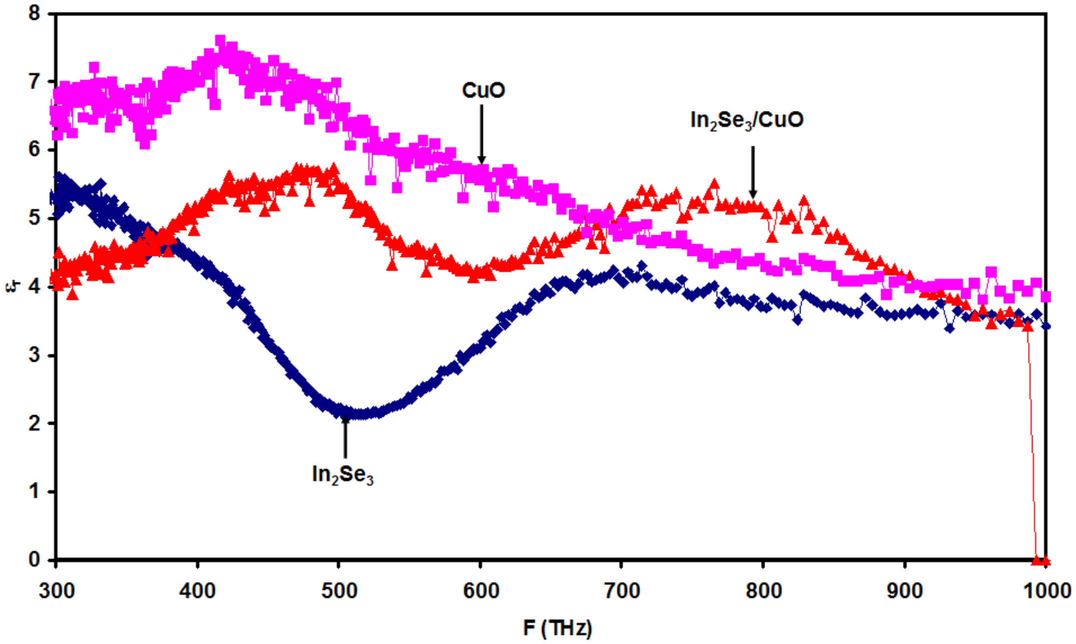

Figure 4.10: The real dielectric constant for γ-In_2Se_3, CuO and γ-In_2Se_3/CuO films in the range of 300-1000 THz.

On the other hand, the imaginary part of dielectric constant is shown in figure 4.11. When we look at this figure we find that the maximum value of $\varepsilon_{im}$for γ-In_2Se_3 to be ~1.1 at 974 THz, and the minimum value 0.4 at 1000THz for CuO, but when we formed the heterojunction γ-In_2Se_3/CuO theε_{im}has a mediate value ~0.8 at 986THz.

The imaginary part of dielectric constant is modeled by Drude-Lorentz model which connected with incident the light frequency by the relation [48]:

$$\varepsilon_{im} = \sum_{i=1}^{k} \frac{\omega_{pei}^2 \omega}{\tau i((\omega_{ei}^2 - \omega^2)^2 + \omega^2 \tau i^{-2})} \tag{4.15}$$

Where k is the number of possible linear oscillators. In this experiment k = 4 .τ is the electron scattering time, ω_e is the resonant frequency, ω_{pe} is the Plasmon frequency given by the relation:

$$\omega_{pe} = \sqrt{\frac{4\pi n e^2}{m^*}} \qquad (2.16)$$

Where n is the density of free electrons, the modeling also allow determining the values of drift mobility (μ) through the relation,

$$\mu = \frac{e\tau}{m*} \qquad (4.17)$$

To find ε_{im} we need to find the effective mass of γ-In_2Se_3, CuO and γ-In_2Se_3-CuO where the effective mass (m^*) is equal:

m^*=((m_e(InSe))$^{-1}$+(m(CuO))$^{-1}$)$^{-1}$for γ-In_2Se_3-CuO

m^*=((m_e(InSe))$^{-1}$)$^{-1}$for γ-In_2Se_3

m^*= ((m (CuO))$^{-1}$)$^{-1}$for CuO

Here m_e of InSe , InSe/CuO and m of CuO are 0.156m_o [100], 0.056 m_o and 0.089m_o [101] respectively. In addition, the values of τ, ω_e, ω_{pe}, n and μ are found with the help of equation (4.13). The values are tabulated in table (4.3). The correlation between the theoretical and experimental solutions can be observed from the colored plotting in figure 4.11.

The tabulated data show the presence of resistive force as the damping coefficient $\gamma = \tau^{-1}$ for γ-In_2Se_3 is 1.0 (fs) $^{-1}$and for CuO is 1.67 (fs) $^{-1}$, the interface is dominated by that of CuO. The higher damping coefficient in CuO is assigned to amorphous nature of films. The amorphous films have random grain distribution which make the electronic motion hard. Reasons of damping are the collision of carriers with impurities, phonons and other carriers [99].

It is also seen that, the free carrier density forγ-In_2Se_3 are 9x10^{17} cm^{-1} and for CuO it is 7.5x10^{18} $cm^{-1}$when they wave interfaced, the density reduced to 2.0x10^{17}. The reason beyond these decrement is the recombination at the interface between the n-type and p-type materials.

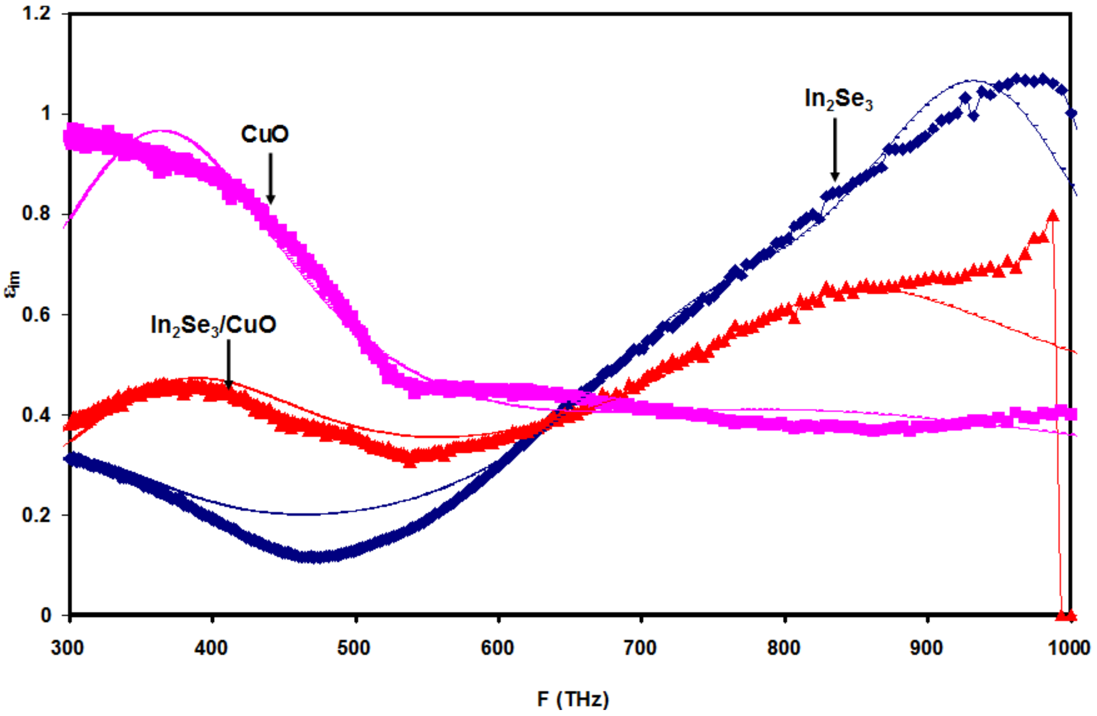

Figure 4.11: The imaginary dielectric constant for γ-In_2Se_3, CuO and γ-In_2Se_3/CuO films in the range of 300-1000 THz.

Table 4.3: The fitting parameters of Drude model for the γ-In_2Se_3, CuO and γ-In_2Se_3/CuO heterojunctions.

	γ-In_2Se_3				**CuO**				**γ-In_2Se_3/CuO**			
m^*/m_o	0.156				0.089				0.056			
$\tau_i(fs)$	1.00	0.70	0.60	0.60	0.60	0.25	0.20	0.20	0.60	0.50	0.30	0.20
n (x 10^{17} cm^{-3})	9.00	25.0	100	370	75.0	100	100	100	20.0	50.0	59.0	75.0
ω_{ei}(x10^{15} Hz)	1.50	2.00	4.70	5.95	2.40	5.30	7.00	9.00	2.50	5.40	5.50	6.90
ω_{pei} (GHz)	1.43	2.38	4.76	9.15	5.45	6.30	6.30	6.30	3.55	5.61	6.10	6.88
$\mu(cm^2/Vs)$	11.2	7.88	6.76	6.76	11.8	5.03	3.95	3.95	18.8	15.6	6.27	9.41

Table 4.3 shows that the scattering time at femto second level for CuO is shorter than that of γ-In_2Se_3. The scattering time depends on the crystalline nature and number of free carriers in the materials. The shorter the scattering time, the larger the electronic friction in the material. Since in accordance with the tabulated data the free carrier density in CuO is much larger than in γ-In_2Se_3 , then the interface is strongly affected by the this large amount. However, due to the pn junction formation, some of the free holes recombine with electrons at the interface to form the depletion layer in the junction and others are not able to be screened due to the quantum confinement and lattice mismatches. The amorphous nature of CuO is a main reason for the short scattering time that resulted in this degree of freedom for charge carrier motion. The scattering time strongly affects the drift mobilities of the materials. As seen from the figure forming the heterojunction increased the drift mobility from 11.2 and 11.8 to 18.8 cm^2/Vs upon interfacing. This value of drift mobility is large enough to nominate the γ-In_2Se_3/CuO heterojunction device for use as thin film transistors.

4.3 Impedance Spectroscopy

When dealing with electrical current and its entry and exit from the material, the type of current inside or outside the material, is an important issue that should be considered. There are two types of current conduction mechanisms called DC and AC conductions. The DC conduction is dominated by thermionic or variable range hopping or tunneling. In the AC conduction, the current is given as time dependent and, thus, the lifetime of the current maybe short. Therefore the electron cannot response to the electric field resulting from this current. In this case, the electron either complete its motion, shake in its place or not to feeling the behavior of the electric field. The impedance spectroscopy is an important tool that help exploring the AC signal processing mechanism through devices.

The hybrid device design of the Al/ CuO/C, Al/ CuO/Au, Al/γ-In_2Se_3/C, Al/γ-In_2Se_3 /Au,Al/γ-In_2Se_3/CuO/Au and Al/γ-In_2Se_3/CuO/C were actualized by evaporating the materials onto Al substrates. The Al film thickness was 0.5 µm. The carbon past and coated Au metal were used as the Schottky point contacts.

4.3.1 Conductivity Spectra

At first we will show the conductance , to understand the behavior of the conductivity as a function of frequency, we have analyzed the electrical conductivity assuming the domination of quantum mechanical tunneling (QMT) and correlated hopping conduction mechanisms, which are explained in chapter two section 2.5.3. To estimate the correlation between experimental and theory, a fitting template was designed.

To understand this model let us see figure 4.12, when we look at this graph we find that the conductance increase with increasing frequency, where the maximum value of the conductivity is $1.4\text{x}10^{-5}$ (Ωcm^{-1}) at 1154 MHz and the minimum value is $2.5\text{x}10^{-8}$ (Ωcm^{-1}) at 14 MHz. This behavior of the conductivity due to the increase of frequency lead to an increase in free carrier density and to increases the conductivity of the device [102].

Looking at the same figure, we find that it consists of two colored curves (pink and blue). The blue colored curve represents the experimental conductivity and the pink colored curve represents the model that has been applied to it.

All this study was based on the equation of AC conductivity for an electron undergoing quantum mechanical tunneling in which conductivity is given by [50]:

$$\sigma_{tun}\omega = \frac{\pi^4}{24} e^2 kT\alpha^{-1}\left(N\left(E_f\right)\right)^2 \omega R_\omega^4 \tag{4.18}$$

In this equation $N(E_f)$ is the density of localized states near the Fermi level, α is a parameter for wave functions employed to describe the localized length of state and $R_\omega$is the hopping distance at a particular frequency (ω).$R_\omega$is given by the equation[50]:

$$R_\omega = \frac{\ln\left(\frac{v_p}{\omega}\right)}{2\alpha} \tag{4.19}$$

Where v_p is the phonon frequency and equal to 6.5x10^{12} s^{-1} [11] for γ-In_2Se_3, and 1.8x10^{13} s^{-1} [11] for CuO.

The fitting of the AC conductivity ($\sigma(w) \propto w^s$) using equation (4.18) takes into account the density of localized states near Fermi level. The optimized and fitting of the experimental data are obtained assuming the validity of the parameter shown in table (4.4).The increasing of conductance with increasing frequency when the value of *s* being in the range from (0.5-1.0) indicates the probable phenomenon of tunneling effect in the materials.

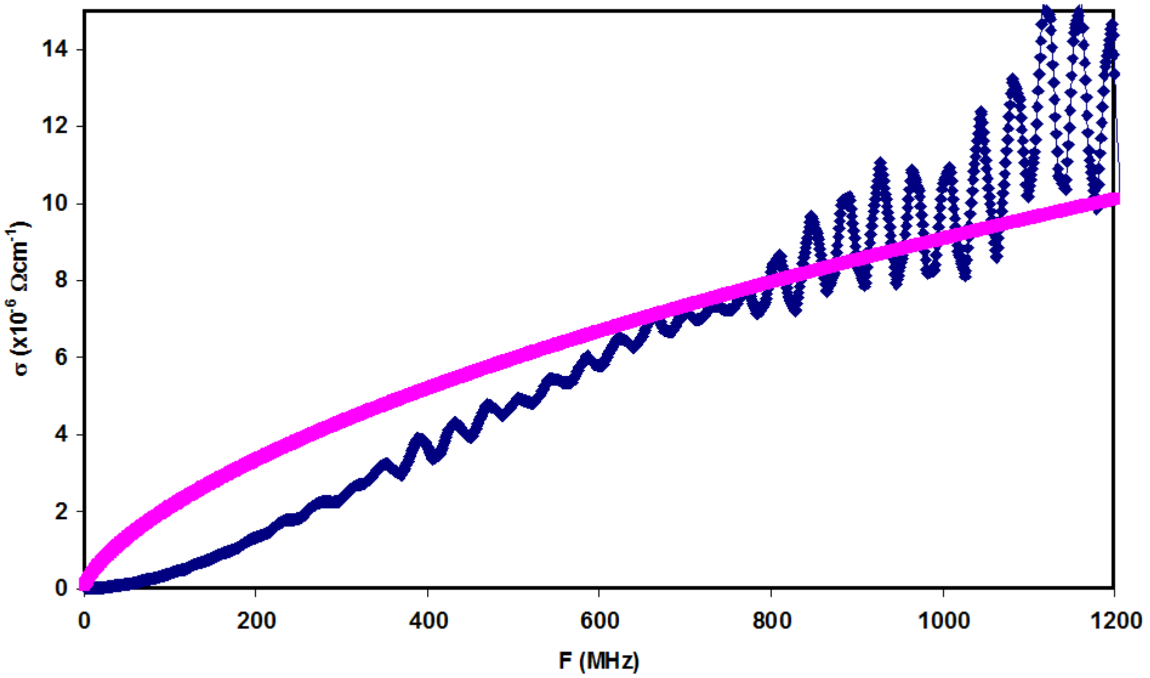

Figure 4.12: The conductivity spectra for the Al/CuO/C tunneling devices.

On the other hand, for Al/CuO/ Au device, the conductivity spectral behavior which is presented in Fig. 4.13 is different. As seen in the figure one note the conductivity decreases with increasing frequency exhibiting low frequency conductivity value of 6.9×10^{-5} (Ωcm^{-1}) at 118 MHz and the high frequency conductivity value of 3.13×10^{-6} (Ωcm^{-1}) at 1748 MHz. The reasons for this behavior of conductivity is ascribed to the correlated barrier hopping [50].

The hopping phenomenon occurs when the conductivity decreases with increasing frequency and the value of S less than 0.5. The AC conductivity in this case is given by the correlated barrier hopping conduction (CBH) equation which is explained in chapter two section (2.5.3) [50]:

$$\sigma_{CBH}(\omega) = \sigma_H(\omega) + \frac{\sigma_L(\omega) - \sigma_H(\omega)}{1 + \omega^2 t^2} \qquad (4.20)$$

Where σ_H and σ_L are the high and low frequency saturation conductivity, respectively, and τ is the relaxation time and given by the equation [50]:

$$\tau = \tau_0 e^{(\zeta)} \tag{4.21}$$

Where τ_o is variable having a value ranges of (10^{-9}- 10^{-7}s) and ζ is based on the probability calculation and equal to:

$$\zeta = 2\alpha R_\omega \tag{4.22}$$

The total experimental conductivity is explained when both transport mechanisms are taken into account [50],

$$\frac{1}{\sigma(\omega)} = \frac{1}{\sigma_{tun}(\omega)} + \frac{1}{\sigma_{CBH}(\omega)} \tag{4.23}$$

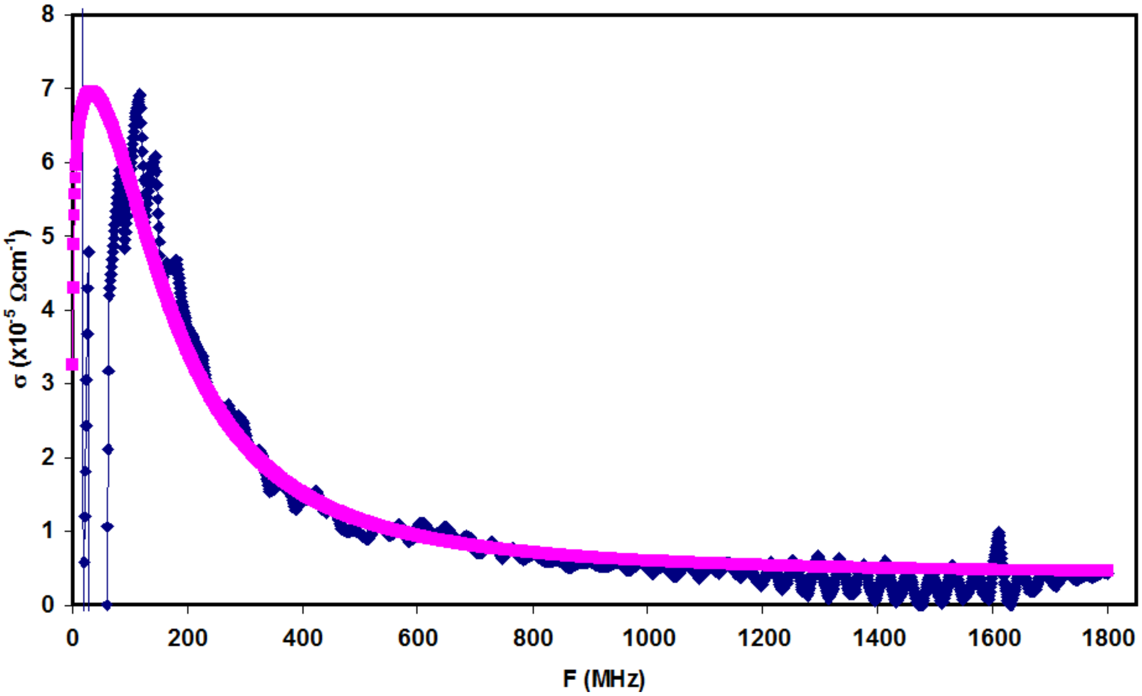

Figure 4.13: The conductivity spectra for the Al/CuO/Au hopping devices.

When we look at the conductivity curve of Al/ γ-In_2Se_3/Au and Al/ γ-In_2Se_3/C in figure 4.14, we note that the curves of conductivity are like the behavior of both conductivities(tunneling and hopping).In Al/ γ-In_2Se_3/Au the conductivity initially equal $2.9x10^{-5}(\Omega cm^{-1})$ after that it increases with increasing frequency exhibiting value of $1.07x10^{-3}$ (Ωcm^{-1}) and finally it decreases reaching a value of $9.03x10^{-6}(\Omega cm^{-1})$. Also in Al/ γ-$In_2Se_3$/C, the conductivity initially equals $4.44x10^{-4}(\Omega cm^{-1})$ then increases to $7.46x10^{-4}(\Omega cm^{-1)}$ and decreases to $1.2x10^{-5}(\Omega cm^{-1})$.

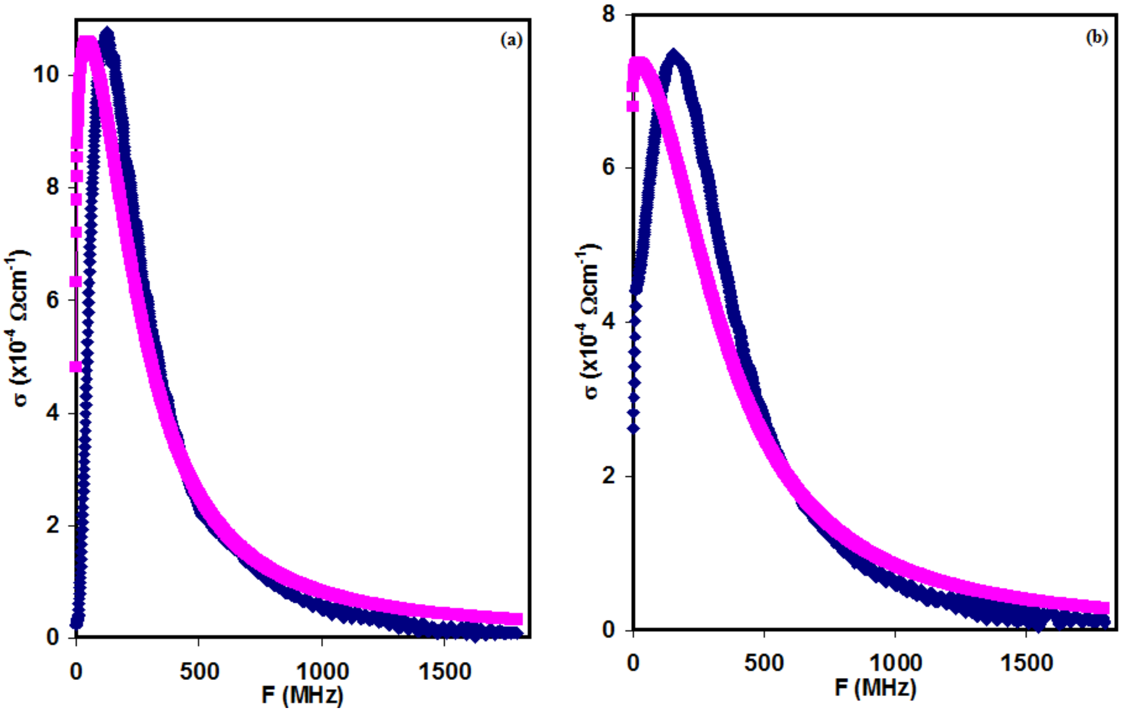

Figure 4.14: The conductivity spectra for the (a) Al/ γ-In_2Se_3/Au, (b) Al/ γ-In_2Se_3/C tunneling-hopping devices.

Figure 4.15, the same behavior for Al/ γ-In_2Se_3/CuO/Au, the conductivity started in $1.02x10^{-4}(\Omega cm^{-1})$ then increased to $7.9x10^{-3}$ (Ωcm^{-1}) and finally decreased to become

$6.1x10^{-6}$ (Ωcm^{-1}). For Al/ γ-In_2Se_3/CuO/C the conductivity started in $4.1x10^{-4}$(Ωcm^{-1}) then increased to $5.6x10^{-4}$(Ωcm^{-1}) and finally decreased to become $3.15x10^{-5}$(Ωcm^{-1}).

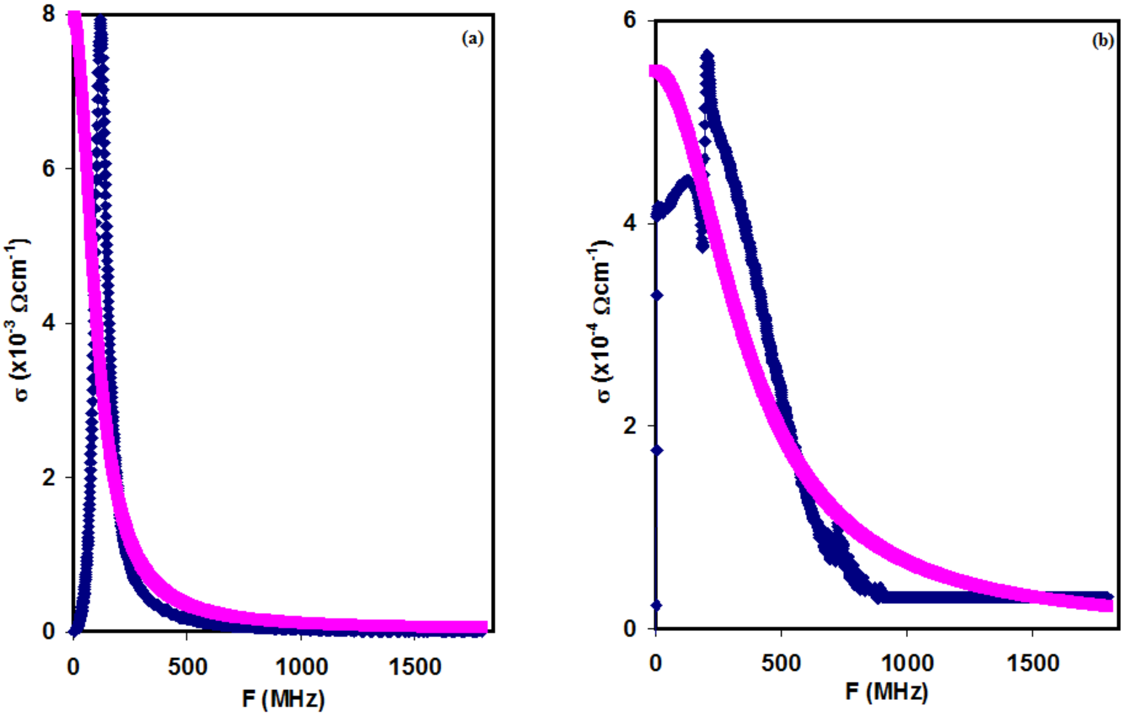

Figure 4.15: The conductivity spectra for the (a) Al/ γ-In_2Se_3/CuO/Au, (b) Al/ γ-In_2Se_3/CuO/C tunneling-hopping devices.

The fitting parameters that produce the experimental conductivity are displayed in table 4.4. In accordance with the table, the value of $N(E_f)$ for Al/ γ-In_2Se_3/ Au is less than the value for Al/ γ-In_2Se_3/ C, the same behavior for Al/ CuO/Au and Al/ CuO/C, respectively, but when we look at Al/ γ-In_2Se_3/CuO/ Au and Al/ γ-In_2Se_3/CuO/ C we note that both samples have the same value of $N(E_f)$. The same observation apply for τ, $\sigma_{ac}(H)$ and $\sigma_{ac}(L)$ where the values for each one vary by type of contact point for each device structure. Such behavior is assigned to different work functions of Au and Carbon. The work function of Au is 5.34 eV while that of Carbon is 5.1 eV. In addition, the Au metal with the electronic configuration can reach higher orbital's in CuO or in γ-In_2Se_3 leading to orbital overlapping and hence it causes strong bonding and less localization in density of states N$\left(E_f\right)$. When the heterojunction is formed, the depletion region at the γ-In_2Se_3/CuO interface becomes more important due to the complex crystalline- amorphous interface. For this reason $N\left(E_f\right)$ remain constant and are extremely high compared to not interfaced materials.

Table 4.4: The fitting parameters of conductance model for the Al/ γ-In_2Se_3/Au, Al/ γ-In_2Se_3/C, Al/ CuO/Au, Al/ CuO/C, Al/γ-In_2Se_3/CuO/Au and Al/γ-In_2Se_3/CuO/C heterojunctions. . .

	Al/ γ-In_2Se_3/ Au	**Al/ γ-In_2Se_3/ C**	**Al/CuO/Au**	**Al/CuO/C**	**Al/ γ-In_2Se_3/CuO/Au**	**Al/ γ-In_2Se_3/CuO/C**
S	0.54	0.54	0.54	0.54	0.54	0.54
$N(E_f) \times 10^{19}\ (eV^{-1}cm^{-3})$	6.50	20.0	1.50	560	200	200
$\tau \times 10^{-9}$(s)	3.90	2.80	6.00	10.0	9.70	2.70
$\sigma_{ac}(H) \times 10^{-3}(\Omega cm)^{-1}$	9.60	0.10	4.00	-	27.9	0.12
$\sigma_{ac}(L) \times 10^{-4}(\Omega cm)^{-1}$	12.0	7.40	0.80	-	80.0	0.05

4.3.2 Capacitance Spectra

The results of the capacitance spectra discussed in this section relate to measurements of series connections. The connections of the RLC circuit was discussed in section 3.3.3.

As seen from figure 4.16, For Al/CuO/Au device, we note that the capacitance started from the negative value -208 nF , then it increased to -3.15 nF at 86 MHz and after this value of frequency the capacitance is mostly remain constant in all the spectra range. The reasons for the negative capacitances was previously assigned to the non-equilibrium interfacial states which force electron conduction by hopping from interfacial to the bulk states, and is also attributed to the existence of the deep and shallow trap states at the two interfaces [50].

In order to give the complete picture of the capacitance and the discontinuity in the values of capacitance spectra, we have analyzed the electrical capacitance through assuming the domination of the Ershov model that take into account the monotonic variations in the transient currents. The model is explained in chapter two section (2.5.4) [50]. It can be summarized by the relation,

$$C(\omega) = C_0 + \frac{a_n \tau_n}{1 + (\omega - \omega_n)^2 \tau_n^2} - \frac{a_p \tau_p}{1 + \left(\omega - \omega_p\right)^2 \tau_p^2} \tag{4.24}$$

Where C_0 is the static capacitance, a_n and $a_p$are the parameters, ω_n and $\omega_p$are the Plasmon frequencies for n-type material (γ-In_2Se_3) and p-type material (CuO and γ-In_2Se_3/CuO), respectively, and τ_0,τ_n and τ_p are the respective relaxation times and assumed to be equal. In this section, we will talk about two solutions: the first one when the parametersa_n and $a_p$are variables and the other solution when they are assumed to exhibit a value of one. On the other hand, when the capacitance spectra of Al/ γ-In_2Se_3/Au and Al/ γ-In_2Se_3/C which are shown in figure 4.17 are considered, we see that the capacitance in both figures is nearly following the same behavior but with different values. For Al/ γ-In_2Se_3/Au the capacitance started from the positive value and equal 10.3 nF, then, the capacitance increasing sharply with frequency 66.2 nF and directly decreasing with frequency to become -35.5 nF, after that the capacitance increases to reach -0.852 nF at 299 MHz, and the final behavior mostly remain constant to reach 1800 MHz . The behavior of Al/ γ-In_2Se_3/C is the same but the first value of capacitance is equal to 10.6 nF. The capacitance increases to 14.6 nF, then it will decrease to become -23.6 nF, and thereafter it increases to -0.701 nF at 211 MHz. Above 211 MJZ, the capacitance remains constant in all the studied range. This decline and rise in the values of capacitance which forms top and bottom (or peak) called resonance and anti-resonance phenomena.

The resonance is established when all the circuit parameters (L, R and C) are balanced and working in equal harmony. In that state, the efficiency of the circuit is very high and very little power is needed to get sustain oscillation at its given frequency. In resonance the current flows freely in the loop and builds to a large quantity, very sharp, high Q and narrow resonances. Thus, the capacitance is very high and changes from negative to positive [103].In anti-resonance case, the circuit parameters are not balanced. In that state, the efficiency of the circuit is very low and very high power is needed to get sustain oscillation at its given frequency. In the anti-resonance case, the little current flows in the loop and builds to a low quantity, very sharp, low Q and narrow resonances, so the capacitance is very low and changes from positive to negative [103].

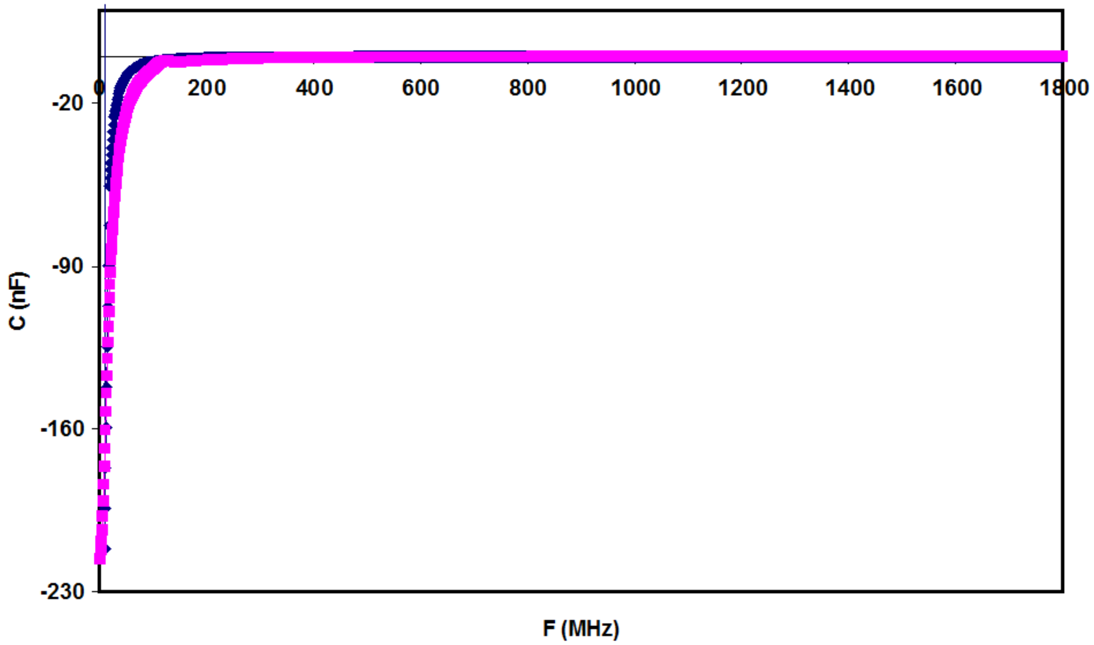

Figure 4.16: The capacitance spectra for the Al/CuO/Au devices.

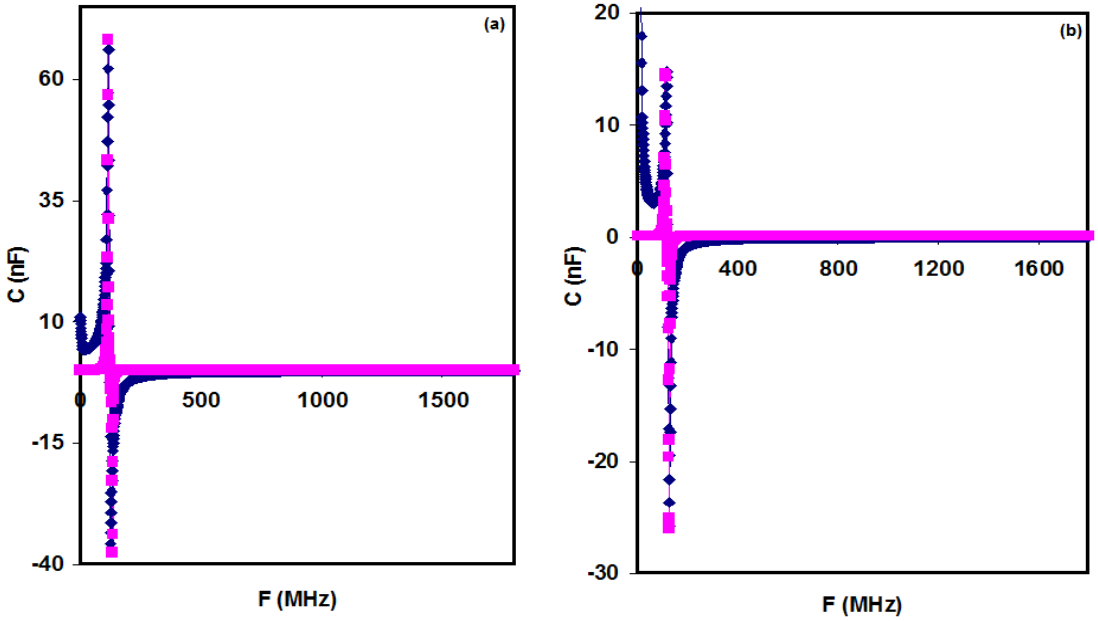

Figure 4.17: The capacitance spectra for the (a) Al/γ-In_2Se_3/Au and (b) Al/γ-In_2Se_3/C devices.

In addition, the Al/γ-In_2Se_3/CuO/Au and Al/γ-In_2Se_3/CuO/C, have the same behavior of capacitance spectra. For Al/γ-In_2Se_3/CuO/Au, the capacitance spectra which are shown in figure 4.18 reveal a resonance profile in the frequency domain of 110–126MHz, and an anti-resonance profile in the frequency domain of 127–131MHz. For Al/γ-In_2Se_3/CuO/C, the capacitance spectra exhibit a resonance profile in the frequency domain of 7–29MHz, and reveal an anti-resonance profile in the frequency domain of 216–221MHz.

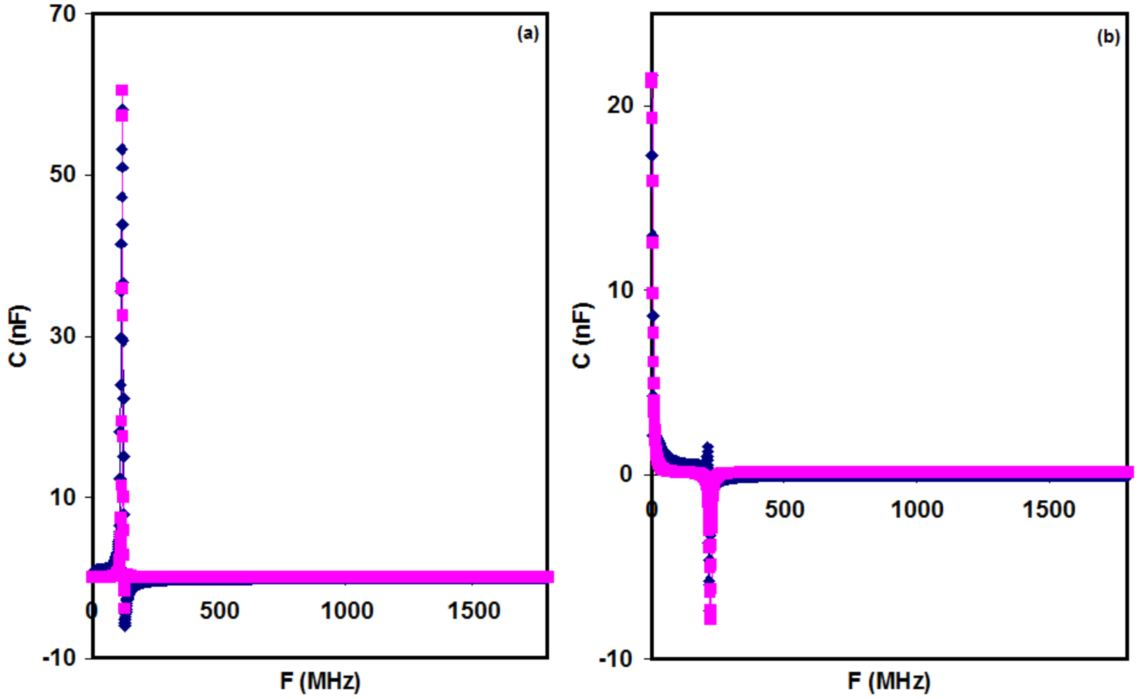

Figure 4.18: The capacitance spectra for the (a) Al/ γ-In_2Se_3/CuO/Au and (b) Al/γ-In_2Se_3/CuO/C devices.

Assuming that a_n and $a_p$in Eqn. 4.24 are fixed and equals one, the experimental data are reproduced through substituting the fitting parameters which are shown in Table 4.5 and Table 4.6. The behavior of capacitance appears to be insensitive to the a_n and a_p parameters. Alternatively, the solution was also obtained assuming their variety. The reproduced experimental data were obtained by the help of the tabulated data. In accordance with the table, the value of τ for Al/ γ-In_2Se_3/ Au is greater than that for Al/ γ-In_2Se_3/ C, the same behavior for Al/ γ-In_2Se_3/CuO/Au and Al/ γ-In_2Se_3/CuO/ C, respectively. When we look at the values of $\omega_{\mathrm{n},}$ we note that nearly all samples have the same value. For ω_{p} the values for Al/ γ-In_2Se_3/ Au and Al/ γ-In_2Se_3/ C are close but the values for Al/ γ-In_2Se_3/CuO/Au and Al/ γ-In_2Se_3/CuO/ C are different. The difference in the parameters for the same sample can be assigned to the difference in the work function of contact point (Au and C).

Physically, the above mentioned model can explained as follows. The capacitance is directly proportional to the dielectric constant. The dielectric constant represent the degree of polarization. When an alternating electric field is incident into the material, the electric dipoles oscillate in response to that field. When the frequency of the dipoles is larger than the AC signal frequency, the dielectric constant is in the static mode and no capacitance change can be observed. As the dipole frequency become close to signal frequency, all dipoles start responding to the alternating current signal. At particular signal frequency (w) equal to that of the materials dipole frequency ($w_n$or w_p) all dipoles oscillate with the field and no free charge can be observed. In this case, the capacitance should reach very high values (infinity). When the value of w become much larger than that of the dipole, the dielectric constant (capacitance) decrease reaching a constant frequency independent value and start not feeling the signal’s frequency. This phenomena is known as typical resonance phenomena. However, because our heterojunction is composed of two materials that contains two opposite type of charges, the point of discontinuity in the capacitance appears when the signal frequency (w) exhibit values close to both of $w_n$and w_p . Particularly, while one material has all positive charges being completely polarized, the other one of negative charge is also completely polarized. Such condition forces no charge to move between the two layers causing the appearance of the discontinuity in the capacitance.

Table 4.5: The fitting parameters of capacitance model for the first solution (a_n *and* a_p are valuable) for the Al/ γ-In_2Se_3/Au, Al/ γ-In_2Se_3/C, Al/ CuO/Au, Al/γ-In_2Se_3/CuO/Au and Al/γ-In_2Se_3/CuO/C heterojunctions.

	Al/ γ-In_2Se_3/ Au	**Al/ γ-In_2Se_3/ C**	**Al/CuO/Au**	**Al/ γ-In_2Se_3/CuO/Au**	**Al/γ-In_2Se_3/CuO/C**
$\boldsymbol{\tau_0 = \tau_n = \tau_p (x10^{-8} s)}$	10	6.80	2.0	10.0	4.00
$\boldsymbol{\omega_n\ (x10^{8} Hz)}$	7.3	7.00	7.5	7.50	1.00
$\boldsymbol{\omega_p\ (x10^{8} Hz)}$	8.5	8.00	1.0	8.00	13.0
$\boldsymbol{a_n}$	0.70	0.23	0.30	0.65	0.54
$\boldsymbol{a_p}$	0.40	0.40	10	0.10	0.20

Table 4.6: The fitting parameters of capacitance model for the second solution (a_n, a_p *are fixed and equal* 1) for the Al/ γ-In_2Se_3/Au, Al/ γ-In_2Se_3/C, Al/ CuO/Au, Al/γ-In_2Se_3/CuO/Au and Al/γ-In_2Se_3/CuO/C heterojunctions.

	Al/ γ-In_2Se_3/ Au	**Al/ γ-In_2Se_3/C**	**Al/CuO/Au**	**Al/γ-In_2Se_3/CuO/Au**	**Al/ γ-In_2Se_3/CuO/C**
$\boldsymbol{\tau_0 = \tau_n = \tau_p (x10^{-8} s)}$	7.00	2.00	90.0	6.00	2.10
$\boldsymbol{\omega_n\ (x10^8 Hz)}$	7.30	7.50	0.17	7.50	1.00
$\boldsymbol{\omega_p\ (x10^8 Hz)}$	8.50	8.80	1.50	8.20	14.0

4.4 Current Conduction Mechanism

The geometrical design of the Al/γ-In_2Se_3/CuO/Au diode is shown in the inset of figure 4.19. The current voltage characteristic curve which was recorded with the help of a Keithley characterization system is displayed in figure 3.11. As can be seen from figure 4.19, for an applied forward voltage we note that the current jumped in two places, from low level current injection "off" mode to high level current injection "on" mode. At 0.123 volt and the current ratio "on/off" of this jump is equal to 15.8, and the second jump at 0.146 volt and the current ratio is 1.55. When voltage is reversed the reverse current tend to remain constant or slightly increase with decreasing voltage.

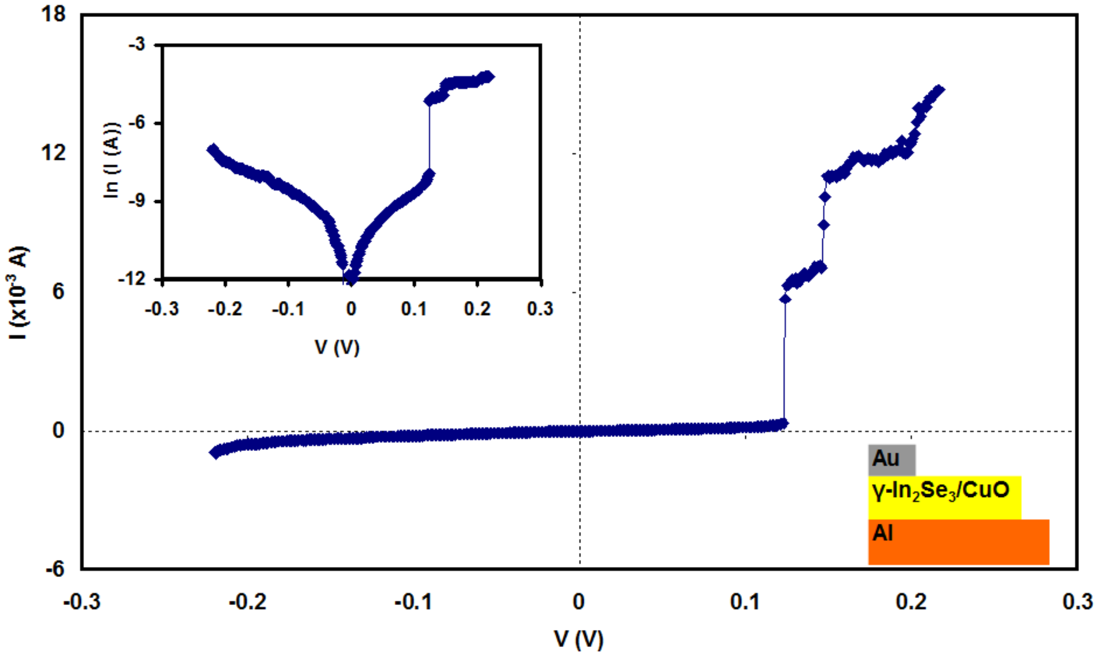

Figure 4.19: The current voltage characteristics for Al/γ-In_2Se_3/CuO/Au diode.

To explore the current conduction mechanism of the I-V characteristics, the theoretical approaches given in chapter two were employed. Particularly, the ln (I) versus ln (V) plots which are shown in figure 4.20 indicating the effect of Richardson Schottky conduction which means that the current conduct through the thermionic emission of charged particles over the barrier height of the diode. Figure 4.20 (a) and (b) shows the linear relationship between the current and voltage in the forward and reverse injection direction, respectively.

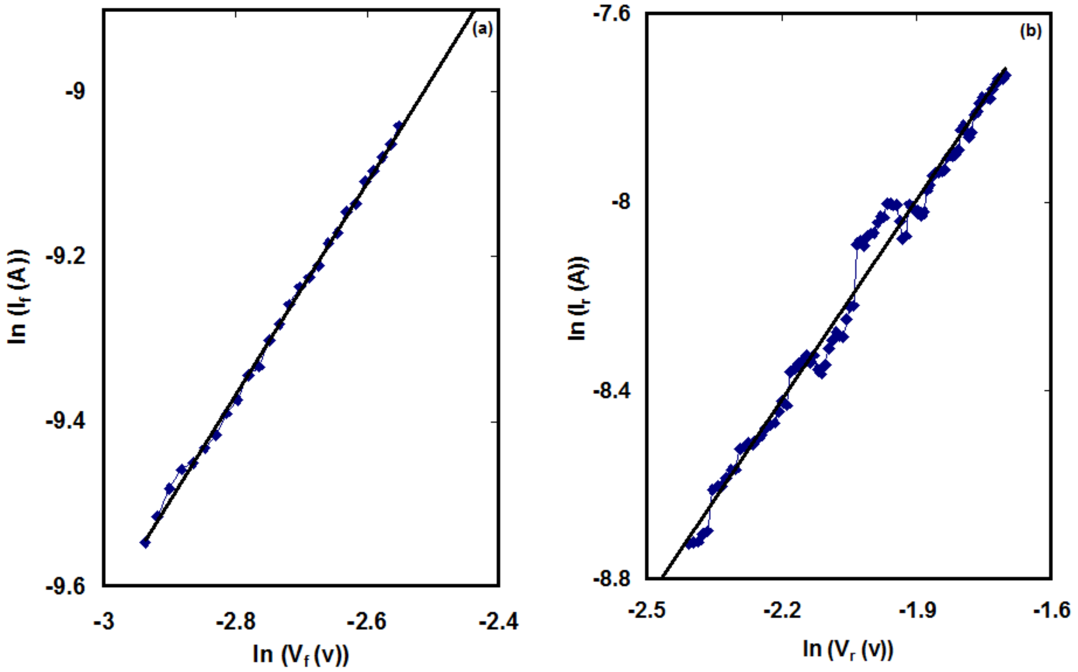

Figure 4.20: The relation between (a) ln (I_f) vs ln(V_f) and (b) ln(I_r) vs ln(V_r) for Al/γ-In_2Se_3/CuO/Au diode.

The Richardson Schottky mechanism takes the form [104, 105] :

$$I = AA^{**}T^2V^{\gamma}e^{q\varphi b/KT} \tag{4.25}$$

$$\varphi_b = \varphi_0 - ή\left(\frac{q□}{4\pi\epsilon_0\varepsilon_r}\right)^{\frac{1}{2}}\left(\frac{\sqrt{V}}{\sqrt{w}}\right) \tag{4.26}$$

Here, q is the electron charge, V is the applied voltage, ή is the ideality factor, T is the temperature (300 K in our case),K is the Boltzmann's constant, A**=120 m*, A is the area (0.0183cm^2) and m* is an effective mass of γ-In_2Se_3/CuO and equals to 0.056m_0. With ή being identity factors, □ and $\gamma$are integers, ϵ_0 is the permittivity of free space, ε_r is the optical dielectric constant and equal 3.428 (Fig. 4.10) for γ-In_2Se_3-CuO, w is the depletion width and φ_0 is the on biased Schottky barrier height.

The relation between ln(I) and $V^{1/2}$ in figure 4.21 ((a) and (b)) is investigated to determine the value of depletion width for the crystal (w) and the value of energy barrier height to the electron flow φ_0 by equation (4.27).

When we plot ln (I) versus the square root of V, we got a direct relation. For Richardson Schottky η, ή =1 and γ =0 so that:

$$\ln\left(\frac{I}{AA^{**}T^2}\right) = \frac{q}{kT}\varphi_0 - \frac{q}{kT}\left(\frac{e}{4\pi\epsilon_0\varepsilon_r}\right)^{1/2}\left(\frac{\sqrt{V}}{\sqrt{w}}\right) \tag{4.27}$$

From (4.27) relation we find that the intercept is equal to $\frac{q}{kT}\varphi_0$, and the slope is equal to $-\frac{q}{kT}\left(\frac{e}{4\pi\epsilon_0\varepsilon_r}\right)^{1/2}\left(\frac{1}{\sqrt{w}}\right)$. From these relations we determine the value of the Schottky barrier height from intercept and the depletion width from slope.

From figure 4.21 (a) the values of depletion width (w) is $5.96\text{x}10^{-7}$ cm and the energy barrier height (φ_0) is 0.307eV. For the reverse part (b), the values of (w) and (φ_0) are equal to $9.95\text{x}10^{-7}$ cm and 0.285eV, respectively. The value means that the electrons will always need an energy greater than 0.307 eV during forward biasing, and greater than 0.285 during reverse biasing to be able to overcome the energy barrier height through the Electric Field Assisted (Tunneling). The barrier height obtained through foreword biasing is larger than reverse biasing probably due to the electronic transform from amorphous to polycrystalline.

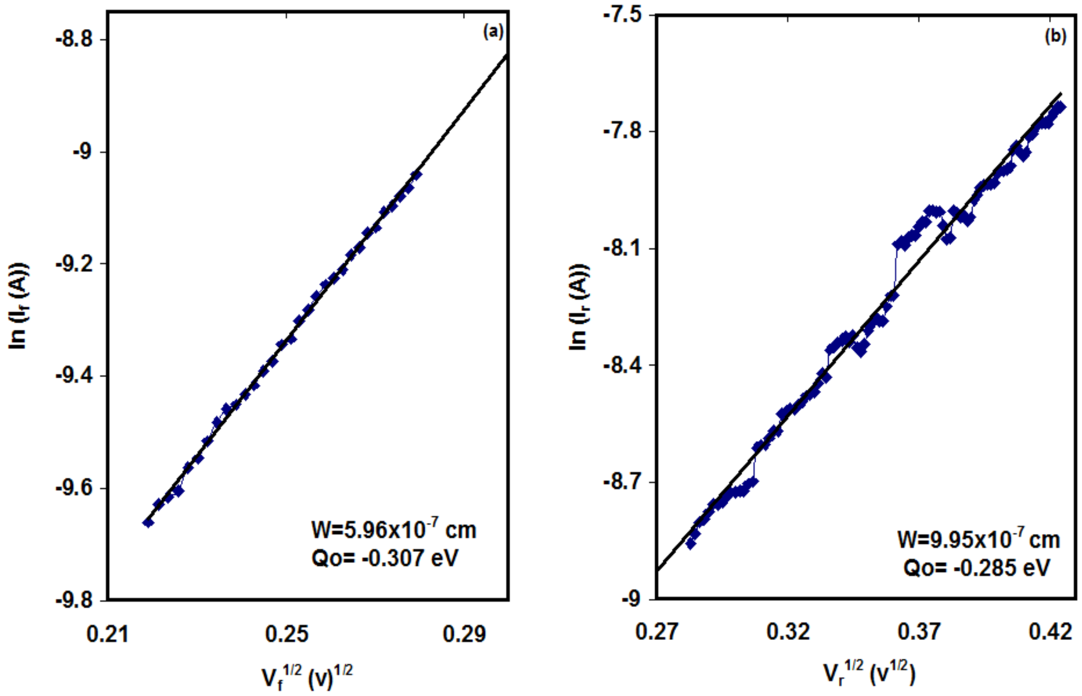

Figure 4.21: The relation between (a) ln (I_f) vs $V_f^{1/2}$ and (b) ln(I_r) vs $V_r^{1/2}$ for Al/γ-In_2Se_3/CuO/Au diode.

When carbon is used as a contact point for γ-In_2Se_3/CuO crystal to become Al/γ-In_2Se_3/CuO/C diode, we find that the I-V characteristics for this diode are shown in figure 4.22. For an applied forward voltage we note that the current jumped in one place only at applied voltage 0.13 volt, and the current ratio of this jump is equal to 6. When voltage is reversed the reverse current slightly increases with decreasing voltage.

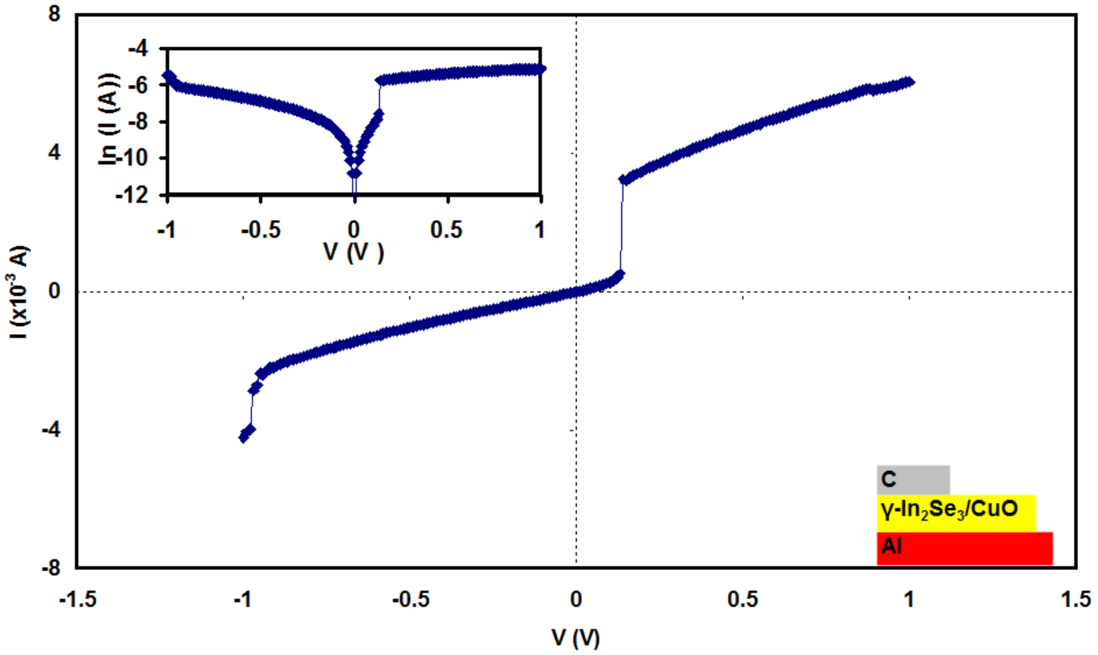

Figure 4.22: The current voltage characteristics for Al/γ-In_2Se_3/CuO/C diode.

To explain the values of (w and φ_0) for this diode, we repeated the analysis as in figure 4.23, for the forward bias the depletion width is 5.58x10^{-5}cm and the energy barrier height is found to be 0.158eV. However, for the reverse biasing condition, the values of w and φ_0 are 5.57x10^{-6}cm and 0.238eV, respectively. These values means that the electrons will always need an energy value greater than 0.158 eV in forward and greater than 0.238 in reverse to be able to overcome the energy barrier height through the electric field assisted (Tunneling).

Comparing these results for energy barrier height with others experiments, we find that the values for energy barrier height for InSe/$CdGa_2Se_4$ is equal 0.75 eV [106], for Au/InSeis 0.76 eV [107], for Al/InSe/C is 0.53 eV [105], and equal to 0.78 eV for Al/InSe/BN/Ag [108]. On the other hand, to compare the value of depletion width in our experiment with other experiments we find that the values of depletion width for Al/InSe/C is 64 nm [102], and for InAs/InSe layer is 694 nm [109].

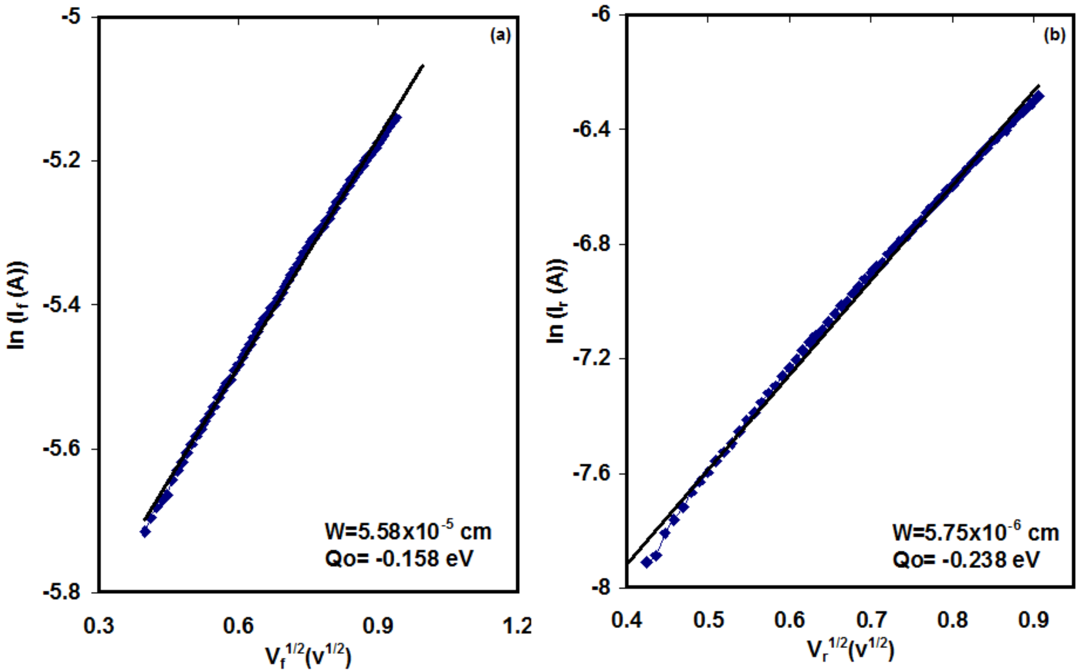

Figure 4.23: The relation between (a) ln (I_f) vs $V_f^{1/2}$ and (b) ln(I_r) vs $V_r^{1/2}$ for Al/γ-In_2Se_3/CuO/C diode.

The values of the depletion width and energy barrier height give us impression of having electric field assisted DC tunneling mechanism and it is the same mechanism which was seen in AC impedance, and they are complementary physics and not new.

The device is Schottky/pn/Schottky, so it is important to draw the energy band diagram for the device. For glass, Al/γ-In_2Se_3/CuO/(Au,C) interface, the band gap was estimated using equation (4.8). In accordance of the data in table 4.7, the conduction band offset for glass, Al/γ-In_2Se_3/CuO/(Au,C) is calculated by using equation (4.7). Eventually, for the valance band offset, equation (4.9) was used.

Table 4.7: The calculated band gap, conduction and valance band discontinuity for γ-In_2Se_3/CuO heterojunction.

	ΔEg (eV)	**ΔEc (eV)**	**ΔEv (eV)**
γ-In_2Se_3-CuO	1.00	0.47	0.53

To draw the band diagram of γ-In_2Se_3/CuO heterojunction is displayed in figure 4.24, we need to define the energy band gap for In_2Se_3which is experimentally found to be 2.1 eV and for CuO is 1.1 eV. The electron affinity of In_2Se_3 and CuO are 3.6 eV [110] and 4.07 eV [91], respectively. Also the work function for In_2Se_3 and CuO are 4.35 eV [111] and 5.13 eV [112], and for Au and Al are 5.34 eV [113] and 4.23 eV [114], respectively.

The measurement of valance band edge shift for the mentioned samples, which are shown in figure 4.24. The valance band splitting value for the studied samples are large enough to nominate the interface for use as thin film transistors.

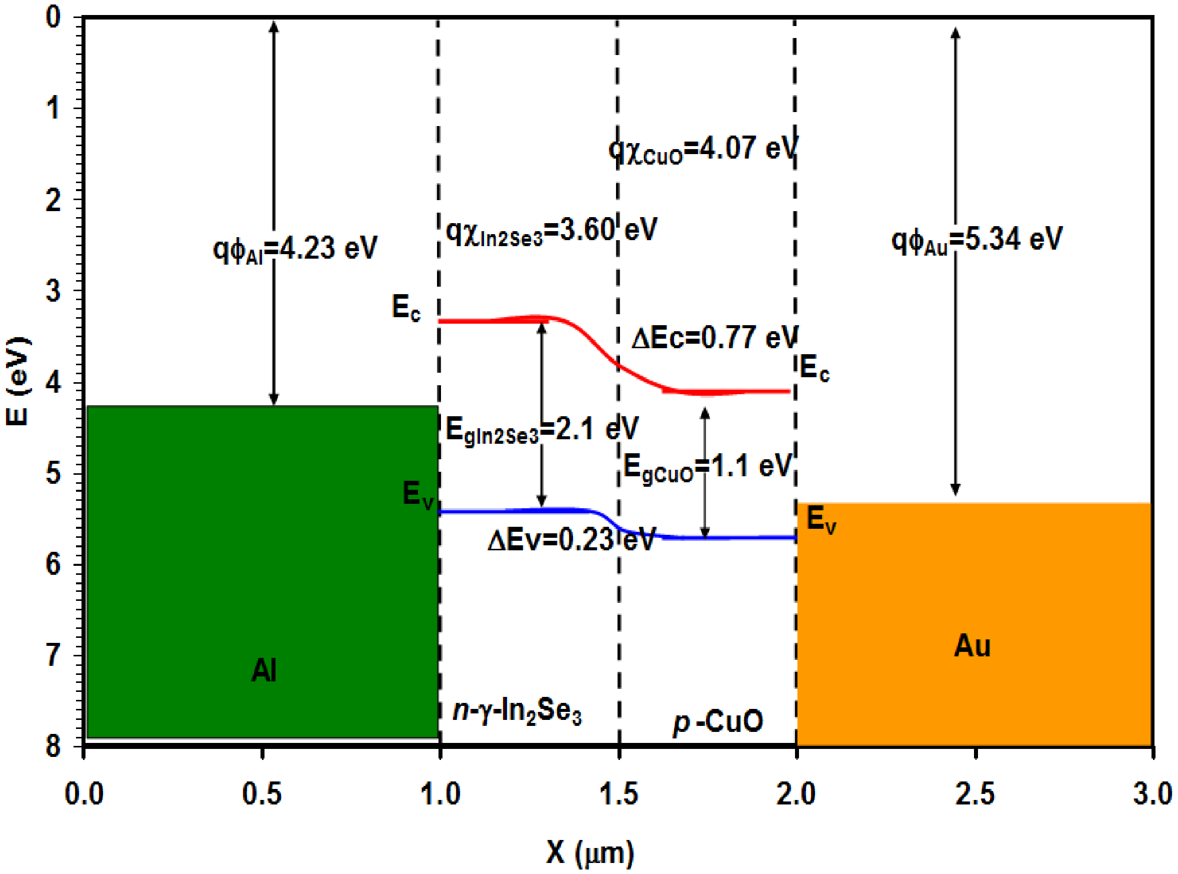

Figure 4.24: The energy band diagram of Al/γ-In_2Se_3/CuO/Au heterojunction.

Chapter Five

Conclusions

In this work a new class of InSe and CuO based devices are produced and characterized. This device has been formed to study several aims. At first, CuO has been evaporated on InSe to form InSe/CuO. After studying the characteristics of this film and because this film has amorphous structure it was redeposited at 250 C^o to obtain polycrystalline phase. As a result of hot substrate γ-In_2Se_3 was formed. For γ-In_2Se_3/CuO device we studied the structural, optical and electrical properties represented by crystalline nature, grain size, strain, dislocation density and, optical absorption, energy band gaps and tails as well as conductivity, capacitance and current-voltage characteristics. The structural analysis for the γ-In_2Se_3/CuO interface revealed hexagonal structure with lattice parameters of values of a= 4.007 A^o and c= 18.90A^o, Stacking Faults (SF) of values of $1.99x10^{-3}$and dislocation density of δ=$6.81X10^{11}$ (line/cm^2). On the other hand, the optical analysis revealed energy band gap value of 1.80 eV and valence and conduction band offsets of values of 0.23 and 0.77 eV, respectively. The electrical properties for this device was studied after depositing Au and C as contact points to form Al/ γ-In_2Se_3/CuO/Au, Al/ γ-In_2Se_3/CuO/C, Al/γ-In_2Se_3/Au, Al/γ-In_2Se_3/C, Al/ CuO/Au and Al/CuO/C device structures. Generally, the AC current conduction in the devices was dominated by conductance the quantum mechanical tunneling and correlated barrier hopping. It was also observed that DC current conduction mechanism are dominated by the Richardson Schottky mechanism. The main transport mechanism of these devices were dominated by the electric field assisted thermionic emission of charge carriers through a depletion width ~ $5.58x10^{-6}$cm and an energy barrier height ~ 0.238 eV.

The results of the electrical analysis of the device nominate it for use as wide spectrum photo detectors, microwave and light signal resonators at the same time and the devices are also expected to behave as a typical transistor that carries the traditional duties of the transistors.

Even though many of the characteristics were clearly investigated, still the “on/off” current ratio need to be improved to make this type of devices more effective. One other major problem we faced is the amorphous nature of the oxide layer. Still efforts must be spent to convert the CuO to polycrystalline phase. This will tack the material to a single phase and will unify its optoelectronic behavior.

References:

[1] Neamen, Donald A. *Semiconductor physics and devices*. Vol. 3. New York: McGraw-Hill, (1997).

[2] Nagatsuma, Tadao, Guillaume Ducournau, and Cyril C. Renaud. "Advances in terahertz communications accelerated by photonics." *Nature Photonics* 10, no. 6 (2016): 371.

[3] Dhyani, Veerendra, and Samaresh Das. "High-Speed Scalable Silicon-MoS 2 PN Heterojunction Photodetectors." *Scientific reports* 7 (2017): 44243.

[4] Sharma, Basant Lal, and Radha Krishna Purohit. *Semiconductor heterojunctions*. Vol. 5. Elsevier, (2015).

[5] Abay, Bahattin. "Barrier Characteristics of Molecular Semiconductor-Based Organic/Inorganic Au/$C_{42}H_{28}$/n-InP Hybrid Junctions." *Red* 860 (2017): 79232.

[6] Li, Ming-Yang, Chang-Hsiao Chen, Yumeng Shi, and Lain-Jong Li. "Heterostructures based on two-dimensional layered materials and their potential applications." *Materials Today* 19, no. 6 (2016): 322-335.

[7] Ma, Dongge, and Yonghua Chen. *Organic Semiconductor Heterojunctions and Its Application in Organic Light-Emitting Diodes*. Vol. 250. Springer, (2017).

[8] Kressel, H. "The application of heterojunction structures to optical devices." *Journal of Electronic Materials* 4, no. 5 (1975): 1081-1141.

[9] Kumar, Challuri Vijay, Lydia Cabau, Emmanuel N. Koukaras, Ganesh D. Sharma, and Emilio Palomares. "Synthesis, optical and electrochemical properties of the A–π-D–π-A porphyrin and its application as an electron donor in efficient solution processed bulk heterojunction solar cells." *Nanoscale* 7, no. 1 (2015): 179-189.

[10] Milnes, Arthur George. *Heterojunctions and metal semiconductor junctions*. Elsevier, (2012).

[11] Madelung, Otfried. *Semiconductors: data handbook*. Springer Science & Business Media, (2012).

[12] Eisenmann, B., and H. Schäfer. "InPrS-InSeTe." *Sulfides, Selenides, Tellurides (Part 2)*. Springer, Berlin, Heidelberg, (1986). 150-165.

[13] Cui, Yanhua, et al. "First-Principles Study of MoO3/Graphene Composite as Cathode Material for High-Performance Lithium-Ion Batteries." *Applied Surface Science* 433 (2018): 1083-1093.

[14] Shmakov, A. N., et al. "Vacancy Ordering in γ-Fe2O3: Synchrotron X-ray Powder Diffraction and High-Resolution Electron Microscopy Studies." *Journal of Applied Crystallography*28.2 (1995): 141-145.

[15] Qin, Jinwen, et al. "Synthesis of porous CuO–CeO 2 nanospheres with an enhanced low-temperature CO oxidation activity." *Nanoscale* 2.12 (2010): 2739-2743.

[16] Sánchez-Royo, Juan F., et al. "Electronic structure, optical properties, and lattice dynamics in atomically thin indium selenide flakes." *Nano Research* 7.10 (2014): 1556-1568.

[17] Bras, Patrice, et al. "Ga-grading and Solar Cell Capacitance Simulation of an industrial Cu (In, Ga) Se2 solar cell produced by an in-line vacuum, all-sputtering process." *Thin Solid Films* 636 (2017): 367-374

[18] Kröger, Michael, et al. "P-type doping of organic wide band gap materials by transition metal oxides: A case-study on Molybdenum trioxide." *Organic Electronics* 10.5 (2009): 932-938.

[19] Vayssieres, Lionel, et al. "One-dimensional quantum-confinement effect in α-Fe2O3 ultrafine nanorod arrays." *Advanced Materials* 17.19 (2005): 2320-2323.

[20] Koffyberg, F. P., and F. A. Benko. "A photoelectrochemical determination of the position of the conduction and valence band edges of p-type CuO." *Journal of Applied Physics* 53.2 (1982): 1173-1177.

[21] Bhalerao, Anuradha B., et al. "(Photo) electrochemical analysis of electrosynthesized fibrous cadmium indium selenide (CdIn2Se4) thin films." *Journal of Photochemistry and Photobiology A: Chemistry* 336 (2017): 69-76.

[22] Pankove, J. I., and H. Schade. "Photoemission from GaN." *Applied Physics Letters* 25.1 (1974): 53-55.

[23] Al Garni, S. E., and A. F. Qasrawi. "TUNABLE Au/Ga 2 S 3/Yb VARACTOR DIODES DESIGNED FOR HIGH FREQUENCY APPLICATIONS." *Chalcogenide Letters* 14.9 (2017).

[24] Rapp, M. "Charging of mesospheric aerosol particles: the role of photodetachment and photoionization from meteoric smoke and ice particles." *Annales geophysicae: atmospheres, hydrospheres and space sciences*. Vol. 27. No. 6. (2009).

[25] Khurram, A. A., et al. "ZnSe/ITO thin films: candidate for CdTe solar cell window layer." *Journal of Semiconductors* 38.9 (2017): 093001

[26] Tanaka, Tooru, et al. "Improved Open-Circuit Voltage and Photovoltaic Properties of ZnTeO-Based Intermediate Band Solar Cells With n-Type ZnS Layers." *IEEE Journal of Photovoltaics* 7.4 (2017): 1024-1030.

[27] Khusayfan, Najla M., and Hazem K. Khanfar. "Design and performance of (Au, Yb)/ZnS/InSe/C heterojunctions as plasmon resonators, photodetectors and microwave cavities." *Journal of Electronic Materials* 46.3 (2017): 1650-1657.

[28] Sze, Simon M., and Kwok K. Ng. *Physics of semiconductor devices*. John wiley & sons, (2006).

[29] Hook, John R., and Henry Edgar Hall. "Solid State Physics (The Manchester Physics Series)." (1991).

[30] AROYO, MOIS I., U. L. R. I. C. H. Muller, and HANS WONDRATSCHEK. "International Tables for Crystallography (2006). Vol. A, Chapter 1.1, pp. 2–5." *Group* (1995) (1992): (2002).

[31] Wadhwa, Amandeep Singh, and Er Harvinder Singh Dhaliwal. *A Textbook of Engineering Material and Metallurgy*. Firewall Media, (2008).

[32] Ruan, Jiafeng, et al. "Nitrogen and sulfur dual-doped carbon films as flexible free-standing anodes for Li-ion and Na-ion batteries." *Carbon* 126 (2018): 9-16.

[33] Chen, Yuanyuan, et al. "High-rate FeS 2/CNT neural network nanostructure composite anodes for stable, high-capacity sodium-ion batteries." *Nano Energy* (2018).

[34] Wang, L. C., et al. "Oxygen Adsorption and Low-Temperature CO Oxidation on a Nanoporous Au Catalyst: Reaction Mechanism and Foreign Metal Effects." *Topics in Catalysis* (2018): 1-16.

[35] Biot, Maurice A. *Mechanics of incremental deformations*. (1965).

[36] West, A. R. (2014). *Solid state chemistry and its applications*. John Wiley & Sons.

[37] Nong, H. T. T., et al. "Stacking faults density driven collapse of magnetic energy in hcp-cobalt nano-magnets." *Advances in Natural Sciences: Nanoscience and Nanotechnology* 8.2 (2017): 025012.

[38] Bhargava, A. K., and C. P. Sharma. *Mechanical Behaviour and testing of materials*. PHI Learning Pvt. Ltd., (2011).

[39] Tilley, Richard JD. *Colour and the optical properties of materials: an exploration of the relationship between light, the optical properties of materials and colour*. John Wiley & Sons, (2010).

[40] Fox, Mark. *Quantum optics: an introduction*. Vol. 15. OUP Oxford, (2006).

[41] Ursu, I., et al. "Damage studies in cubic ZnSe single crystals grown from melt." *Applied Physics A* 48.5 (1989): 451-456.

[42] Raghuvanshi, G. S. *Engineering Physics*. PHI Learning Pvt. Ltd., (2016).

[43] Jalali, Reza, et al. "The effect of Al content, substrate temperature and nitrogen flow rate on optical band gap and optical features of nanostructured TiAlN thin films prepared by reactive magnetron sputtering." *Applied Physics A* 122.11 (2016): 978.

[44] Pankove, Jacques I. *Optical processes in semiconductors*. Courier Corporation, (1971).

[45] Shklovskii, Boris Isaakovich, and Alex L. Efros. *Electronic properties of doped semiconductors*. Vol. 45. Springer Science & Business Media, (2013).

[46] Fox, Mark. *Optical properties of solids*. Vol. 3. Oxford university press, (2010).

[47] Vial, Alexandre, et al. "Improved analytical fit of gold dispersion: Application to the modeling of extinction spectra with a finite-difference time-domain method." *Physical Review B* 71.8 (2005): 085416.

[48] Omareya, Olfat A., A. F. Qasrawi, and S. E. Al Garni. "Effect of Au nanosandwiching on the structural, optical and dielectric properties of the as grown and annealed InSe thin films." *Physica B: Condensed Matter* 520 (2017): 57-64.

[49] Ghosh, Aswini. "Frequency-dependent conductivity in bismuth-vanadate glassy semiconductors." *Physical review B* 41.3 (1990): 1479.

[50] Khusayfan, Najla M., A. F. Qasrawi, and Hazem Khanfar. "Design and electrical performance of CdS/Sb 2 Te 3 tunneling heterojunction devices." *Materials Research Express* (2018).

[51] Sharma, Sunita, M. M. Singh, and K. D. Mandal. "Dielectric and Electrical Properties of Undoped and Fe-Doped Yttrium Copper Titanate." *Processing and Properties of Advanced Ceramics and Composites VII* 252 (2015): 95.

[52] Darwish, A. A. A., M. M. El-Nahass, and A. E. Bekheet. "AC electrical conductivity and dielectric studies on evaporated nanostructured InSe thin films." *Journal of Alloys and Compounds* 586 (2014): 142-147.

[53] Murugavel, Sevi, and Manisha Upadhyay. "AC conduction in amorphous semiconductors." *Journal of the Indian Institute of Science* 91.2 (2012): 303-318.

[54] Ghosh, Aswini. "Frequency-dependent conductivity in bismuth-vanadate glassy semiconductors." *Physical review B* 41.3 (1990): 1479.

[55] Ershov, Maxim, et al. "Negative capacitance effect in semiconductor devices." *IEEE Transactions on Electron Devices*45.10 (1998): 2196-2206.

[56] Grilj, Marjan. "Thermionic emission." University of Ljubljana Faculty of mathematics and physics Department of physics, (April 2008)

[57] Lu, Chao, and Alvin Warren Czanderna, eds. *Applications of piezoelectric quartz crystal microbalances*. Elsevier, (2012).

[58] Practical Electrical Engineering – page 9-31 Sergey N. Makarov, Reinhold Ludwig, Stephen J. Bitar-(2016).

[59] Anl Garni, Sabah E., and Atef F. Qasrawi. "Impedance Spectroscopic Analysis of the InSe/ZnSe/InSe Interface."IEEE Transactions on Electron Devices 64.1 (2017): 244-249.

[60] Humphreys, Frederick John, and Max Hatherly. *Recrystallization and related annealing phenomena*. Elsevier, (2012).

[61]Al Garni, S. E., Olfat A. Omareye, and A. F. Qasrawi. "Growth and characterization of InSe/Ge/InSe interfaces." *Optik-International Journal for Light and Electron Optics* 144 (2017): 340-347.

[62] Araki, Takeshi, et al. "High critical current density scheme of YBa2Cu3O7− x films by the metalorganic deposition using trifluoroacetates." *Superconductor Science and Technology* 15.6 (2002): 913.

[63] Jeong, Jaewoo, et al. "Suppression of metal-insulator transition in VO2 by electric field–induced oxygen vacancy formation." *Science* 339.6126 (2013): 1402-1405.

[64] Trukhanov, S. V., et al. "Polarization origin and iron positions in indium doped barium hexaferrites." *Ceramics International* 44.1 (2018): 290-300.

[65] Wu, Sumei, et al. "Influence of S content on the structure and ignition time of CuIn (S, Se) 2 powders prepared by mechanochemical process." *Journal of Alloys*

*and Compounds*731 (2018): 318-322.

[66] Rau, Julietta V., et al. "The bone building blues: Self-hardening copper-doped calcium phosphate cement and it's in vitro assessment against mammalian cells and bacteria." *Materials Science and Engineering: C* 79 (2017): 270-279.

[67] Tatarchuk, Tetiana, et al. "Structural, optical, and magnetic properties of Zn-doped CoFe 2 O 4 nanoparticles." *Nanoscale research letters* 12.1 (2017): 141.

[68] Kuzian, R. O., et al. "Comment onOxygen vacancy-induced magnetic moment in edge-sharing CuO $ _ {2} $ chains of Li $ _ {2} $ CuO $ _ {2} $'." *arXiv preprint arXiv: 1708.06335* (2017).

[69] Hu, Riming, Xiaolong Zhou, and Jie Yu. "The effect of surface structure on Ag atom adsorption over CuO (111) surfaces: A first principles study." *Applied Surface Science* 425 (2017): 1111-1117.

[70] Zatsepin, D. A., et al. "Soft-x-ray-emission study of the influence of Li+-doping, irradiation, and plastic deformation on CuO." *Physical Review B* 59.1 (1999): 211.

[71] Rabier, J., and M. F. Denanot. "Plastic deformation of YBa2Cu3O7-δ and related structural defects." *Revue de Physique appliquée* 25.1 (1990): 55-59.

[72] Wang, Hui, et al. "Origin of n-type conductivity in two-dimensional InSe: In atoms from surface adsorption and van der Waals gap." *Physica E: Low-dimensional Systems and Nanostructures* 98 (2018): 66-73.

[73] Poller, Maximilian J., Neil Burford, and Konstantin Karaghiosoff. "Reversible Oxidative Se− Se Coupling of Phosphine Selenides by Ph3Sb (OTf) 2." *Chemistry-A European Journal* 24.1 (2018): 85-88.

[74] Jehdaramarn, Attawit, et al. "Effects of appended hydroxyl groups and ligand chain length on copper coordination and oxidation activity." *New Journal of Chemistry* 42.1 (2018): 654-661.

[75] Wei, Xin, et al. "Oxygen-induced degradation of the electronic properties of thin-layer InSe." *Physical Chemistry Chemical Physics* (2018).

[76] Siyar, Muhammad, et al. "Effect of annealing temperature on the phase transition, band gap and thermoelectric properties of Cu 2 SnSe 3." *Journal of Materials Chemistry C* (2018).

[77] Zhang, Xiaofeng, et al. "Electrochemical fabrication of shape-controlled Cu 2 O with spheres, octahedrons and truncated octahedrons and their electrocatalysis for ORR." *New Journal of Chemistry* 42.1 (2018): 458-464.

[78] Limpijumnong, Sukit, et al. "Hydrogen doping in indium oxide: An ab initio study." *Physical Review B* 80.19 (2009): 193202.

[79] Julien, C., N. Benramdane, and J. P. Guesdon. "Transformation steps of structure in flash-deposited films of a-InSe." *Semiconductor Science and Technology* 5.8 (1990): 905.

[80] Lashkarev, G. V., et al. "Anomalies of magnetic properties of layered crystals InSe containing Mn." *Materials Science and Engineering: C* 27.5-8 (2007): 1052-1055.

[81] Cao, Minhua, et al. "A controllable synthetic route to Cu, Cu 2 O, and CuO nanotubes and nanorods." *Chemical Communications*15 (2003): 1884-1885.

[82] Axelevitch, A., B. Gorenstein, and G. Golan. "Investigation of optical transmission in thin metal films." *Physics Procedia* 32 (2012): 1-13.

[83] Bornoz, Pauline, et al. "A bismuth vanadate–cuprous oxide tandem cell for overall solar water splitting." *The Journal of Physical Chemistry C* 118.30 (2014): 16959-16966.

[84] Alharbi, S. R., and A. F. Qasrawi. "Optical and electrical performance of Yb/InSe interface." *Materials Science in Semiconductor Processing* 43 (2016): 60-64.

[85] Jalali, Reza, et al. "The effect of Al content, substrate temperature and nitrogen flow rate on optical band gap and optical features of nanostructured TiAlN thin films prepared by reactive magnetron sputtering." *Applied Physics A* 122.11 (2016): 978.

[86] Julien, C., et al. "Electrical and optical properties of In2Se3 thin films." *Thin Solid Films* 137.1 (1986): 27-37.

[87] Muiva, Cosmas M., Stephen T. Sathiaraj, and Julius M. Mwabora. "Thermal and compositional defects in chemical spray pyrolysed indium selenide (In2Se3) thin films: effects on film properties." *Journal of Optoelectronics and Advanced Materials*13.9 (2011): 1240.

[88] Clavijo, J., E. Romero, and G. Gordillo. "Effect of substrate temperature on the optical, structural and morphological properties of In2Se3 thin films grown by a two-step process." *Journal of Physics: Conference Series*. Vol. 167. No. 1. IOP Publishing, (2009).

[89] Al Garni, S. E., and A. F. Qasrawi. "Optical analysis of Ge/MgO and Ge/BN thin layers designed for terahertz applications." *Materials Science in Semiconductor Processing* 31 (2015): 678-683.

[90] Ichimura, Masaya, and Shoichi Kawai. "Band alignment at the CdS/FeS2 interface based on the first-principles calculation." *Japanese Journal of Applied Physics* 54.3 (2015): 038002.

[91] Zhang, Ke, et al. "A flexible p-CuO/n-MoS 2 heterojunction photodetector with enhanced photoresponse by the piezo-phototronic effect." *Materials Horizons* 4.2 (2017): 274-280.

[92] Kudrynskyi, Zakhar R., et al. "Giant Quantum Hall Plateau in Graphene Coupled to an InSe van der Waals Crystal." *Physical review letters* 119.15 (2017): 157701.

[93] Xiao, KaiJian, Alexandra Sarabando de Carvalho, and Antonio Helio Castro Neto. "Defects and oxidation resilience in\ch {InSe}." *arXiv preprint arXiv: 1705.05519* (2017).

[94] Park, Nae-Man, et al. "Quantum confinement in amorphous silicon quantum dots embedded in silicon nitride." *Physical review letters* 86.7 (2001): 1355.

[95] Wilson, William L., P. F. Szajowski, and L. E. Brus. "Quantum confinement in size-selected, surface-oxidized silicon nanocrystals." *Science* 262.5137 (1993): 1242-1244.

[96] John, S., and A. Mohan. "Investigation on the Structural and Optical Properties of Thermally Evaporated Indium Selenide Compound Material for Solar Cell Application." *Proceedings of the International Conference Nanomaterials: Applications and Properties*. No. 2, no. 1. Sumy State University Publishing, (2013).

[97] Peled, A. "Photo-Excited Processes, Diagnostics and Applications." *Fundamentals and Advanced Topics* (2003).

[98] Qasrawi, A. F., Hazem K. Khanfar, and Renal RN Kmail. "Optical conduction in amorphous GaSe thin films." *Optik-International Journal for Light and Electron Optics* 127.13 (2016): 5193-5195.

[99] Eldlio, Mohamed, Franklin Che, and Michael Cada. "Drude-lorentz model of semiconductor optical plasmons." *IAENG Transactions on Engineering Technologies*. Springer, Dordrecht, (2014). 41-49.

[100] Yang, Hung-Wei, et al. "Ultraefficient Ultraviolet and Visible Light Sensing and Ohmic Contacts in High-Mobility InSe Nanoflake Photodetectors Fabricated by the Focused Ion Beam Technique." *ACS applied materials & interfaces* (2018).

[101] Dolai, S., et al. "Cupric oxide (CuO) thin films prepared by reactive dc magnetron sputtering technique for photovoltaic application." *Journal of Alloys and Compounds* 724 (2017): 456-464.

[102] Qasrawi, A. F. "Illumination effects on the capacitance spectra and signal quality factor of Al/InSe/C microwave sensors." *Journal of electronic materials* 42.6 (2013): 1033-1036.

[103] McKinley, A. F., et al. "The analytical basis for the resonances and anti-resonances of loop antennas and meta-material ring resonators." *Journal of Applied Physics* 112.9 (2012): 094911.

[104] Bart Van Zaghberoeck, Principle of Semiconductor Device, (2011).

[105]Qasrawi, A. F. "Electrical parameters of Al/InSe/C RF sensors." *Physica Scripta* 89.6 (2014): 065802.

[106] Vaipolin, A. A., et al. "Photosensitive structures based on CdGa 2 Se 4 single crystals." *Semiconductors* 37.5 (2003): 553-558.

[107] Alharbi, S. R., and A. F. Qasrawi. "Plasmon-electron dynamics at the Au/InSe and Y/InSe interfaces designed as dual gigahertz-terahertz filters." *Optik-International Journal for Light and Electron Optics* 136 (2017): 524-530.

[108] Qasrawi, Atef F., and Hazem K. Khanfar. "Design and Applications of Al/InSe/BN/Ag Hybrid Device." *IEEE Sensors Journal* 15.6 (2015): 3603-3607.

[109] Velichko, A. V., et al. "Highly-mismatched InAs/InSe heterojunction diodes." *Applied Physics Letters* 109.18 (2016): 182115.

[110] Drapak, S. I., et al. "On the mechanisms of current transfer in n-In 2 Se 3-p-GaSe heterostructures." *Technical Physics Letters*28.9 (2002): 707-710.

[111] Sakalauskas, S., and A. Sodeika. "Automated measuring instrument of the surface electric potential and potential distribution." *Review of scientific instruments* 69.2 (1998): 466-468.

[112] Masood, Hafiz Tariq, et al. "CdTe Thin Film Solar Cells Fabricated With CuO as a Buffer Layer in the Back Contact." *IEEE Journal of Photovoltaics* 7.4 (2017): 1124-1129.

[113] Khusayfan, Najla M., A. F. Qasrawi, and Hazem K. Khanfar. "Design and characterization of Au/In4Se3/Ga2S3/C field effect transistors." *Results in Physics* 8 (2018): 1239-1244.

[114] Phung, Thi Viet Bac, et al. "Theoretical studies on ionization potential of aluminum clusters." *International Journal of Quantum Chemistry* 109.15 (2009): 3602-3612.

الملخص

في هذه الرسالة تم دراسة أثار زراعة أكسيد النحاس على الانديوم سيلينايد بطريقة التبخير على الخصائص البنائية و الضوئية و الكهربائية على مادة الانديوم سيلينايد/أكسيد النحاس. حيث تم تبخير طبقة رقيقة من أكسيد النحاس (5 مايكرومتر) على طبقة من انديوم سيلينايد (5 مايكرو متر) للحصول على عينة من (انديوم سيليناد /أكسيد النحاس). و ذلك من اجل دراسة خصائص هذه العينة، إلا انه بعد إجراء التجارب عليها، توصلنا إلى أنها تمتلك خصائص رديئة و غير مجدية لإجراء الأبحاث و الدراسات عليها لكونها مادة عشوائية التركيب، لذلك تم تسخين هذه العينة على درجة حرارة عالية تصل إلى 250س. بعد التسخين تم الحصول على تركيبة جاما من هذه العينة، حيث انه تم إجراء العديد من الدراسات عليها وذلك لتحقيق أهداف هذا البحث.

تم دراسة الخصائص الضوئية، البنائية و الكهربائية و تم التوصل لما يلي: عند دراسة الخصائص الضوئية لهذه العينة و جدنا أنها تمتلك فجوة للطاقة، كما أنها تمتلك أذناب مستويات طاقة ممتدة، حيث أن هذه القيم لفجوة الطاقة كافية لتجعل من هذه العينة قطعة الكترونية مميزة. أما في ما يتعلق بالنتائج البنائية لهذه العينة لوحظ أن عملية التسخين قامت بتحويل هذه التركيبة من مادة عشوائية التركيب إلى مادة بلورية التركيب، حيث تقوم هذه العملية بتحسين الخصائص البنائية من خلال إحداث زيادة في طول المحاور الشبكية الأفقية و العمودية، بالإضافة إلى تقليل كمية الأخطاء في التراص بين الطبقات الذرية، أيضا تقلص في كمية الخلل و انخفاض في كمية الالتواء في ترتيب الذرات. على الصعيد الالكتروني تم دراسة الخصائص الالكترونية لهذه القطعة وذلك بعد تبخير مادة الذهب و إضافة مادة الكربون كنقاط توصيل باستخدام أكثر من تقنية و التي منها تقنية تسلل النفق الميكانيكي الكمي و تقنية قفز حواجز الطاقة المترابطة و ذلك لدراسة الموصلية، السعة و دراسة التغير في التيار و الجهد، حيث أن هذه القطعة تمتلك عرض منطقة نفاذ الكتروني صغيرة بالإضافة إلى ارتفاع حاجز الطاقة.

النتيجة النهائية و التي تم التوصل لها في هذه الرسالة انه يمكن استخدام هذه القطعة كجهاز تصوير ضوئي، أو في المايكروفونات و الإشارات الضوئية، كما يمكن استخدامها كترانزستورات.